

AWARD NUMBER: W81XWH-18-1-0506

TITLE: Engineering biomaterial based therapies for improved lymphatic function and the resolution of chronic inflammation in post-traumatic osteoarthritis

PRINCIPAL INVESTIGATOR: Brandon Dixon

**CONTRACTING ORGANIZATION: Georgia Tech Research Corporation
Atlanta, GA 30332**

REPORT DATE: Sept 2019

TYPE OF REPORT: Annual

**PREPARED FOR: U.S. Army Medical Research and Materiel Command
Fort Detrick, Maryland 21702-5012**

DISTRIBUTION STATEMENT: Approved for Public Release; Distribution Unlimited

The views, opinions and/or findings contained in this report are those of the author(s) and should not be construed as an official Department of the Army position, policy or decision unless so designated by other documentation.

REPORT DOCUMENTATION PAGE

Form Approved
OMB No. 0704-0188

Public reporting burden for this collection of information is estimated to average 1 hour per response, including the time for reviewing instructions, searching existing data sources, gathering and maintaining the data needed, and completing and reviewing this collection of information. Send comments regarding this burden estimate or any other aspect of this collection of information, including suggestions for reducing this burden to Department of Defense, Washington Headquarters Services, Directorate for Information Operations and Reports (0704-0188), 1215 Jefferson Davis Highway, Suite 1204, Arlington, VA 22202-4302. Respondents should be aware that notwithstanding any other provision of law, no person shall be subject to any penalty for failing to comply with a collection of information if it does not display a currently valid OMB control number. **PLEASE DO NOT RETURN YOUR FORM TO THE ABOVE ADDRESS.**

1. REPORT DATE Sept 2019			2. REPORT TYPE Annual		3. DATES COVERED 15 Aug 2018 – 14 Aug 2019	
4. TITLE AND SUBTITLE Engineering biomaterial based therapies for improved function and the resolution of chronic inflammation in post-traumatic osteoarthritis					5a. CONTRACT NUMBER	
					5b. GRANT NUMBER W81XWH-18-1-0506	
					5c. PROGRAM ELEMENT NUMBER	
6. AUTHOR(S) Brandon Dixon E-Mail: dixon@gatech.edu					5d. PROJECT NUMBER	
					5e. TASK NUMBER	
					5f. WORK UNIT NUMBER	
7. PERFORMING ORGANIZATION NAME(S) AND ADDRESS(ES) Georgia Tech Research Corporation 505 10 th St NW Atlanta GA 30318-5775					8. PERFORMING ORGANIZATION REPORT NUMBER	
9. SPONSORING / MONITORING AGENCY NAME(S) AND ADDRESS(ES) U.S. Army Medical Research and Materiel Command Fort Detrick, Maryland 21702-5012					10. SPONSOR/MONITOR'S ACRONYM(S)	
					11. SPONSOR/MONITOR'S REPORT NUMBER(S)	
12. DISTRIBUTION / AVAILABILITY STATEMENT Approved for Public Release; Distribution Unlimited						
13. SUPPLEMENTARY NOTES						
14. ABSTRACT For the first year of the project, we have demonstrated the utility of near-infrared imaging system to assess the clearance of various sized molecules (2kDa through 50kDa) from the knee joint of rats. The larger molecules are specifically taken up into lymphatics and thus, are useful tools to determine the function of lymphatics during osteoarthritis development and progression. Preliminary findings suggest that lymphatic function may be hindered at mid-stage osteoarthritis and current work are addressing the possible changes to the lymphatic vessel contractility. In addition to understanding lymphatic clearance, the near-infrared imaging technology can be applied to determine intra-articular delivery and retention of drugs within the joint. For this, liposome carriers are synthesized and are currently being evaluated for their prolonged retention within the knee joint. Continued investigation of this innovative technology will provide evidence of improved drug delivery and efficacy in treating osteoarthritis.						
15. SUBJECT TERMS						
16. SECURITY CLASSIFICATION OF:			17. LIMITATION OF ABSTRACT	18. NUMBER OF PAGES	19a. NAME OF RESPONSIBLE PERSON USAMRMC	
a. REPORT	b. ABSTRACT	c. THIS PAGE			19b. TELEPHONE NUMBER (include area code)	
Unclassified	Unclassified	Unclassified	Unclassified			

TABLE OF CONTENTS

	<u>Page</u>
1. Introduction	4
2. Keywords	4
3. Accomplishments	5
4. Impact	16
5. Changes/Problems	16
6. Products	18
7. Participants & Other Collaborating Organizations	20
8. Special Reporting Requirements	22
9. Appendices	22

1. INTRODUCTION:

Osteoarthritis (OA) is associated with chronic unresolved inflammation that is a key driver of disease development and progression. The central dogma in the OA field is that chronic inflammation is an inherent problem of production, i.e. the tissues of the joint continuously produce inflammatory cytokines, proteases, and other pathologic factors. The clearance of these factors has always been thought to be rapid and thus, is assumed not to be rate limiting in disease progression. Additionally, downstream communication from clearance (such as at the lymph node) has been largely neglected. These assumptions have received little attention and in part, because the tools to truly test these hypotheses have been limited. However, in all other peripheral tissue diseases, the functional process and communication between the tissue, the lymphatic vessel conduit, and the lymph nodes is critical in the resolution of inflammation. Thus, the **overall objective** of this PRMRP grant is to develop biomaterial-based therapies that can be integrated with imaging modalities to both: 1) elucidate the role of lymphatic function in normal and diseased joints; and 2) promote joint clearance and the resolution of chronic inflammation by delivering inflammation resolving lipid mediators using controlled-release nanoparticles. Our **central hypothesis** is that lymphatic function is a critical component in OA disease progression and regenerative therapies that improve lymphatic function and the resolution of chronic inflammation will attenuate OA disease development and progression. Thus, the following Specific Aims were designed:

Aims 1: *To develop a set of biomaterial-based tools to quantitatively interrogate lymphatic clearance function.*

Aims 2: *To evaluate lymphatic function during the pathogenesis of OA in the rat medial meniscus transection (MMT)-induced OA model.*

Aims 3: *To engineer novel intra-articular therapeutics to improve lymphatic function and resolution of inflammation during post traumatic OA.*

2. KEYWORDS:

osteoarthritis, intra-articular delivery, knee clearance, lymphatics, inflammation, resolvin

3. ACCOMPLISHMENTS:

Specific Aim 1: Develop NIR tools to assess lymphatic function and clearance of various sized particles from intra-articular injection.	Emory Site 1	GA Tech Site 2	Expected Timeline	Complete
Major Task 1 – <i>Determine the clearance kinetics of 2kDa and 40kDa PEG's from intra-articular injections into the knee joint and their uptake into lymphatics.</i>				
Subtask 1 – Determine the clearance kinetics and localization of 2kDa PEG-NIR particles	Willett	Dixon	8 - 10/18	100%
Subtask 2 – Determine the clearance kinetics and localization of 40kDa PEG-NIR particles	Willett	Dixon	9 - 12/18	100%
Milestone(s) Achieved	Willett	Dixon	12/18	100%
Local IACUC Approval	Willett	Dixon	Approved	100%
Milestone Achieved: ACURO Approval	Willett	Dixon	Approved	100%
Major Task 2 – <i>Determine the retention and clearance kinetics of PEG-liposome carriers from intra-articular injections into the knee joint and their uptake into lymphatics.</i>				
Subtask 1 - Determine the clearance kinetics and localization of 500nm NIR-labelled liposome carriers	Willett	Garcia & Dixon	1 - 3/19	50%
Subtask 2 – Determine the clearance kinetics and localization of 500nm liposome carriers containing 40kDa PEG-NIR	Willett	Garcia & Dixon	1 - 3/19	50%
Subtask 2 – Determine the clearance kinetics and localization of 900nm NIR-labelled liposome carriers	Willett	Garcia & Dixon	3 - 5/19	70%
Subtask 3 – Determine the clearance kinetics and localization of 900nm liposome carriers containing 40kDa PEG-NIR	Willett	Garcia & Dixon	3 - 5/19	60%
Milestone(s) Achieved:	Willett	Garcia & Dixon	5/19	
Specific Aim 2: Apply NIR technology to assess lymphatic function and clearance of materials within osteoarthritic joints.				
Major Task 3 - <i>Determine the effect of OA on lymphatic function and clearance of small particles.</i>				
Subtask 1 – Determine the clearance kinetics and localization of 2kDa PEG particles in MMT-induced OA animals at early, mid and late stage	Willett	Dixon	4/19-1/20	60%
Subtask 2 – Determine the clearance kinetics and localization of 40kDa PEG particles in MMT-induced OA animals at early, mid and late stage	Willett	Dixon	4/19-1/20	60%
Milestone(s) Achieved:	Willett	Dixon	1/20	
Major Task 4 – <i>Determine the effect of OA on lymphatic architect and clearance of PEG-liposome carriers.</i>				
Subtask 1 - Determine the clearance kinetics and localization of NIR-labelled liposome carriers in MMT-induced OA animals at early, mid and late stage	Willett	Dixon	6/19-8/20	15%
Subtask 2 - Determine the clearance kinetics and localization of liposome carriers containing 40kDa PEG-NIR in MMT-induced OA animals at early, mid and late stage	Willett	Dixon	6/19-8/20	15%
Milestone(s) Achieved:	Willett	Dixon	8/20	
Specific Aim 3: Administer resolvin therapies in liposome nanoparticles to treat OA and correct for lymphatic dysfunction.				
Major Task 5 – <i>Determine the Effects of Resolvins to treat OA.</i>				
Subtask 1 – Fabrication and assessment of liposome carriers containing Resolvins D1 and E1	Willett	Garcia & Dixon	5 - 7/20	0%
Subtask 2 – Determine the efficacy of Resolvins to treat early stage of OA	Willett	Garcia & Dixon	6 - 10/20	0%
Milestone(s) Achieved:	Willett	Garcia & Dixon	10/20	
Major Task 6 – <i>Determine the effect of PEG-liposome carriers containing resolvins on the progression of OA and their ability to improve lymphatic function during late stage OA.</i>				
Subtask 1 - Effect of Resolvin to treat mid to late stage of OA by using different therapeutic regimen	Willett	Garcia & Dixon	9/20-7/21	0%
Milestone(s) Achieved:	Willett	Garcia & Dixon	7/21	
Final analyses & manuscript preparation.	Willett	Garcia & Dixon	5 - 7/21	

What was accomplished under these goals?

Specific Aim 1: Develop NIR tools to assess lymphatic function and clearance of various sized particles from intra-articular injection.

Major Task 1 – Determine the clearance kinetics of 2kDa and 40kDa PEG's from intra-articular injections into the knee joint and their uptake into lymphatics.

Subtask 1 – Determine the clearance kinetics and localization of 2kDa PEG-NIR particles

Subtask 2 – Determine the clearance kinetics and localization of 40kDa PEG-NIR particles

We have completed Major Task 1 and this body of work can be found in our published manuscript, “Endothelin-1 inhibits size dependent lymphatic clearance of PEG-based conjugates after intra-articular injection into the rat knee” (doi: 10.1016/j.actbio.2019.04.025). Briefly, we have developed a method to monitor the *in vivo* clearance of particles from rat knee joints using near-infrared (NIR)

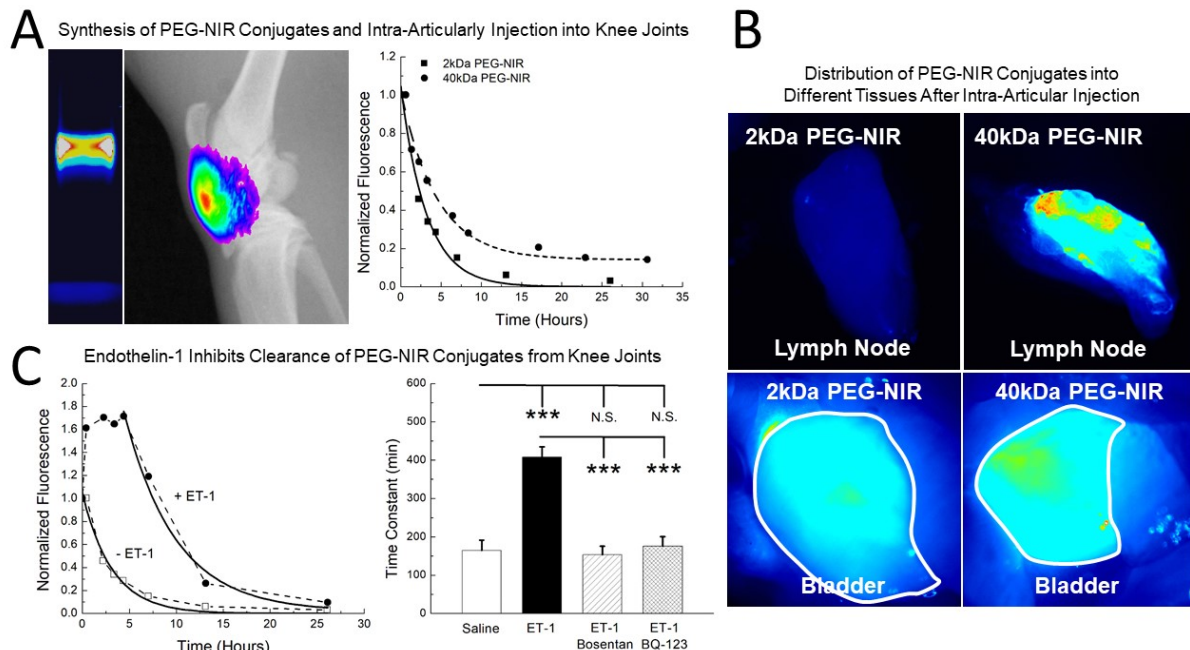


Figure 1: A, Separation of 40kDa polyethylene glycol (PEG) conjugated to NIR dye (PEG-NIR; upper band) from free dye (lower band) on SDS-PAGE. The PEG-NIR material was injected into the intra-articular space of rat knees and the change in NIR fluorescence was observed at differing time points. The clearance of 2kDa PEG-NIR was faster than the clearance of 40kDa PEG-NIR from the knee joint. B, 2kDa PEG-NIR was not found in the lymph node while the 40kDa PEG-NIR was found in the lymph node. Both 2kDa and 40kDa PEG-NIR were found collected in the bladder. C, the clearance of both 2kDa and 40kDa PEG-NIR were inhibited by endothelin-1 (ET-1). The effects of ET-1 were inhibited with endothelin receptor antagonists, bosentan and BQ-123.

imaging technology (Fig. 1A). We found that intra-articular injection of different sized particles (i.e. 2kDa and 40kDa PEG-NIR conjugates) can yield differing clearance kinetics and these differences are associated with venous clearance pathway or with lymphatic clearance pathway (Figure 1B). Notably, the clearance of these NIR conjugates can be perturbed by the biologic endothelin-1 (ET-1), a vasoactive peptide known to be elevated in the synovial fluid of osteoarthritis patients, and its effects can be blocked by antagonizing the endothelin-1 receptor with small molecule inhibitors (Figure 1C).

Major Task 2 – Determine the retention and clearance kinetics of PEG-liposome carriers from intra-articular injections into the knee joint and their uptake into lymphatics.

Subtask 1 - Determine the clearance kinetics and localization of 500nm NIR-labelled liposome carriers

Subtask 2 – Determine the clearance kinetics and localization of 500nm liposome carriers containing 40kDa PEG-NIR

Subtask 2 – Determine the clearance kinetics and localization of 900nm NIR-labelled liposome carriers

Subtask 3 – Determine the clearance kinetics and localization of 900nm liposome carriers containing 40kDa PEG-NIR

Since we were able to track particles in the range of 1-10's of nanometers, we set out to determine the clearance of particles in the hundred nanometers and micron range. To this end, we have fabricated

nanomaterial liposomes (as originally proposed) to use as a drug delivery carrier. Liposomes were comprised of 80% 1, 2, dipalmitoyl-*sn*-glycero-3-phosphocholine (DPPC), 15% cholesterol and 5% 1,2-distearoyl-*sn*-glycero - 3 - phosphoethanolamine - N - [amino (polyethylene glycol)-2000] (DSPE-PEG)

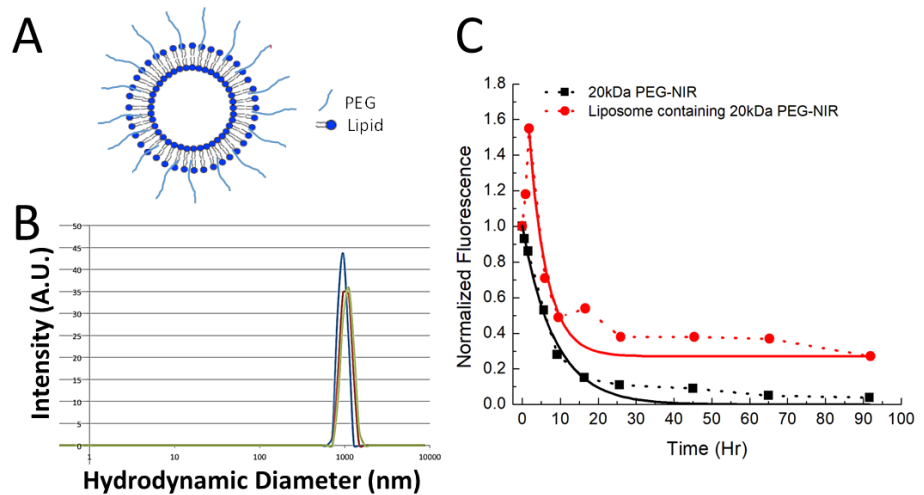


Figure 2: A, schematic of liposome composition. B, Assessment of fabricated liposomes after extrusion through a 1 micron-size polycarbonate filter. C, Representative clearance kinetics of liposomes containing PEG-NIR.

(Figure 2A). To synthesize specific sizes, liposomes were extruded through polycarbonate membranes with 1-micron size pores in phosphate-buffered saline (PBS). The quality of the liposomes was assessed using Malvern Zetasizer (Figure 2B). The ~1-micron-sized liposomes were stable at 4°C. These liposomes were synthesized with the 20kDa PEG-NIR tracer incorporated into the core of the liposome and injected intra-articularly into a rat knee. A representative clearance curve can be observed in Figure 2C.

In addition to designing a drug carrier, we have also investigated the clearance of additional biomaterials and particles including hyaluronan (HA), albumin, extracellular vesicles and alginate microspheres. HA is an extracellular matrix abundant in the synovial fluid of joints and is degraded during OA. Further,

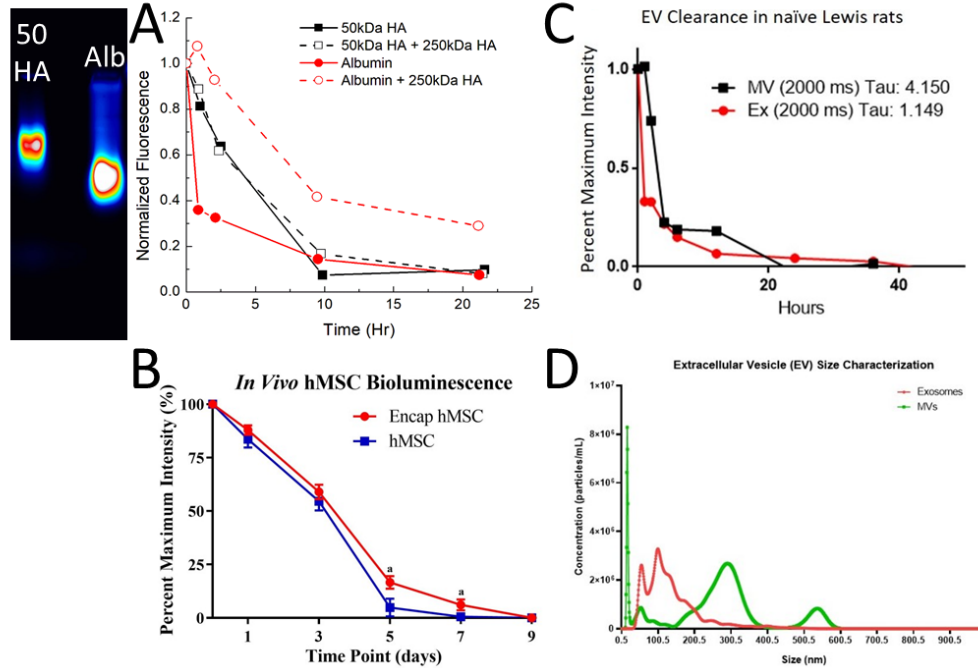


Figure 3: A, Assessment of purified 50kDa hyaluronan-NIR (50 HA) and purified albumin-NIR (Alb) on 1% agarose gel (left panel) and the clearance of HA-NIR and albumin-NIR in the presence and absence of 250kDa HA. B, clearance of 150-micron alginate beads with encapsulated human Mesenchymal Stromal Cells (MSCs) using bioluminescence. C, clearance of NIR-labeled extracellular vesicles and D, size characterization of the extracellular vesicles (comparable size range to the PEG-liposomes).

3A). These conjugated dyes were injected into rat knees and their clearance kinetics were assessed. The clearance of albumin appears to be faster than 50kDa HA. In the presence of 250kDa HA though, the clearance of albumin appeared delayed while no effect was found for 50kDa HA (n=1). This suggests that 250kDa HA may affect protein clearance within the synovium. Additional studies are ongoing to confirm this observation. We have also characterized clearance of alginate microspheres (~150 microns) encapsulated with human Mesenchymal Stromal Cells (hMSCs) after intra-articular injection. Alginate microspheres were retained in the joint out to 9 days; this work was published (doi: 10.22203/eCM.v037a04). We have also characterized clearance of naturally occurring extracellular vesicles, including microvesicles and exosomes --- which are of similar size range of our synthetic PEG-liposomes (Figure 3C and 3D). In a previous publication, we have shown that exosomes clear by the lymphatic system to the draining lymph nodes. Together, characterization of these materials and particles is setting up tools to comprehensively understand of joint clearance and lymphatic function.

To conclude Specific Aim 1, we have demonstrated that NIR technology can be applied to determine the clearance kinetics of various sized materials from the rat knee joint. Specifically, we

have engineered 40kDa PEG-NIR, 50kDa HA-NIR, albumin-NIR, PEG-liposomes, alginate microspheres, and extracellular vesicles. These reagents and materials will be tested in a rat medial meniscus transection (MMT)-induced osteoarthritis model (Specific Aim 2). In addition to synthesizing NIR tools, we have determined that some of these NIR reagents (i.e. 40kDa PEG-NIR and exosomes) are trafficked to lymph nodes. Thus, these lymphatic-specific tracers enable a mechanism to assess lymphatic function *in vivo*. Further work will be conducted in FY2 to determine the *in vivo* clearance kinetics and payload of liposomes.

Specific Aim 2: Apply NIR technology to assess lymphatic function and clearance of materials within osteoarthritic joints.
Major Task 3 - <i>Determine the effect of OA on lymphatic function and clearance of small particles.</i>
Subtask 1 – Determine the clearance kinetics and localization of 2kDa PEG particles in MMT-induced OA animals at early, mid and late stage
Subtask 2 – Determine the clearance kinetics and localization of 40kDa PEG particles in MMT-induced OA animals at early, mid and late stage

MMT-Induced Osteoarthritis Rat Model

Using the NIR tools we have developed in Specific Aim 1, we have begun applying these tools in the medial meniscus transection (MMT) rat model for osteoarthritis. This MMT rat model has been described and characterized by many investigators, but most limit the study to within the first 3 weeks after surgery. Given that our initial data, suggests that lymphatic dysfunction becomes more apparent at later stages of the disease, we sought to develop a thorough characterization of the joint phenotype during late-stage OA progression in the MMT rat model. Herein, we present a detailed characterization of this model and its effect on articular cartilage and bone remodeling from time of surgery to 12 weeks post-surgery. Using equilibrium partitioning of an ionic contrast agent *via* microCT (EPIC-microCT), we have found that articular cartilage can be quantitatively analyzed in 3-dimension and may distinguish different stages of osteoarthritis (Figure 4A). For instance, the articular cartilage volume is significantly increased for rat tibia that underwent MMT surgery when compared to Sham-operated or naïve tibia. The changes to articular cartilage volume though, is not significant at 12-weeks of MMT induction, which is explained by the loss of articular cartilage (i.e. increased in exposed bone). Thus, articular cartilage volume is a reliable parameter for early- (3-weeks) and mid-stage (6-weeks) characterization of OA progression and is not a reliable parameter for determining the late-stage OA phenotype. Similarly, articular cartilage thickness for MMT-induced OA followed the same trend as MMT-induced OA articular cartilage volume, there was a significant increase at early- and mid-stages of OA and an insignificant change at late-stage of OA. For articular cartilage surface roughness, MMT induction on rat tibia was increased at all time points compared to naïve or Sham induction. Exposed bone occurs when articular cartilage is degraded to the subchondral bone layer. We found that this parameter is evident at mid-stage of OA and increases thereafter through the late stage of OA.

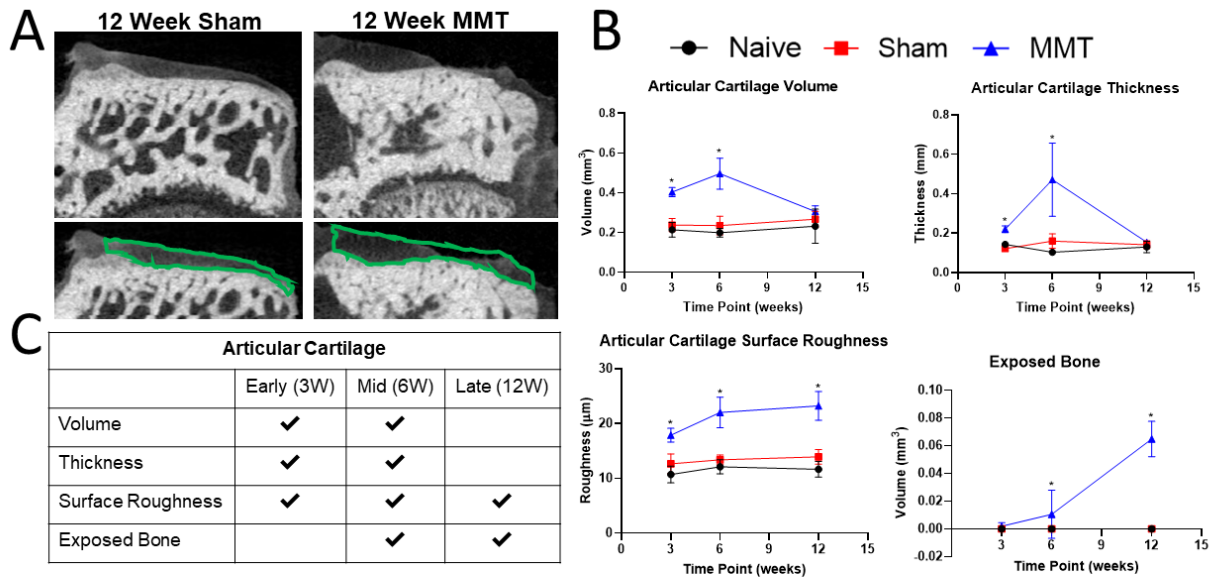


Figure 4: A, EPIC-microCT image of rat tibia that had undergone 3- (n=8), 6- (n=8) or 12-weeks (n=4) of Sham-surgery or of MMT-surgery. The green outline reflects the analyzed region of the articular cartilage surface. B, Plot of various parameters for Naïve unoperated hindlimb), Sham-operated hindlimb and MMT-operated hindlimb with respect to time of surgery. MMT-operated hindlimbs showed increased articular cartilage volume, articular cartilage thickness, articular cartilage surface roughness and exposed bone. C, A table summarizing the results and defining the criteria that can be used to distinguish each stage of OA progression (i.e. early, mid and late).

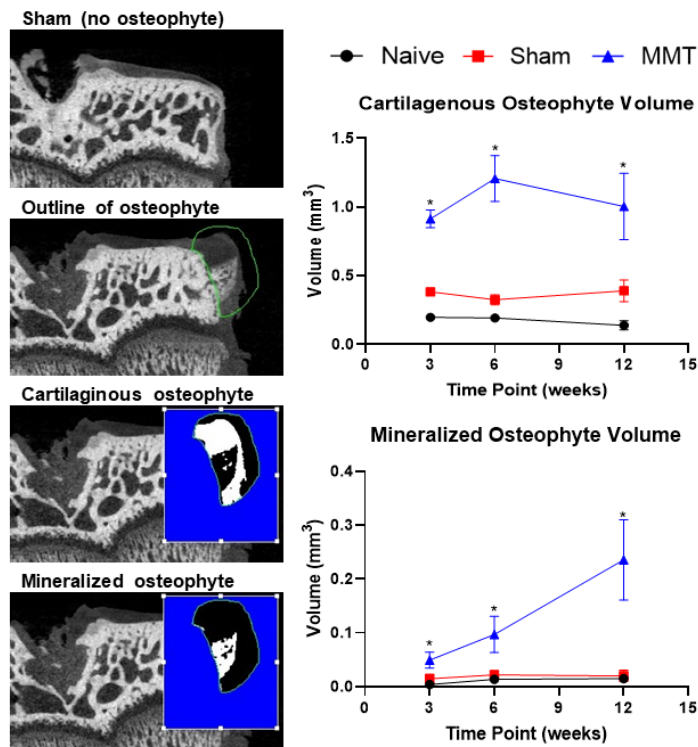


Figure 5: Formation of cartilaginous and mineralized osteophyte in MMT-induced OA. Left panels are EPIC-microCT images of rat tibia and shows the quantitative analysis of cartilaginous osteophyte (3rd panel) and of mineralized osteophyte (4th panel).

In addition to changes to articular cartilage, MMT-induced OA also caused changes to bone architecture. For instance, osteophyte formation is evident as early as 3 weeks of MMT induction and progressively increases over time. Osteophyte formation is further described as cartilaginous osteophyte, which is a protrusion or outgrowth by endochondral ossification, or mineralized osteophyte, which is the deposition of calcium in the extracellular matrix to produce hardened bone. Again, with EPIC-microCT, we found that both cartilaginous and mineralized osteophytes are increased over the progression of MMT-induced OA.

Clearance of Small NIR Conjugates in MMT-Induced Osteoarthritis

Using the MMT-induced OA rat model, we tested the effect of OA on clearance of 2kDa PEG-NIR, a tracer that is not cleared through the lymphatic pathway, and 40kDa PEG-NIR, a tracer cleared via lymphatics (n=3-6). The initial study did not find any significant differences in the clearance of either the 2kDa or the 40kDa PEG-NIR at these small sample sizes (initial experiment that will be repeated) though some trends were observed. Clearance of small particles (less than 5nm) via the venous system did not appear to be altered during osteoarthritis (Figure 6A). For the 40kDa PEG-NIR tracer which clears through the lymphatics system, there were trends for longer retention times after surgery along with higher standard deviations (variability) in both operated and contralateral

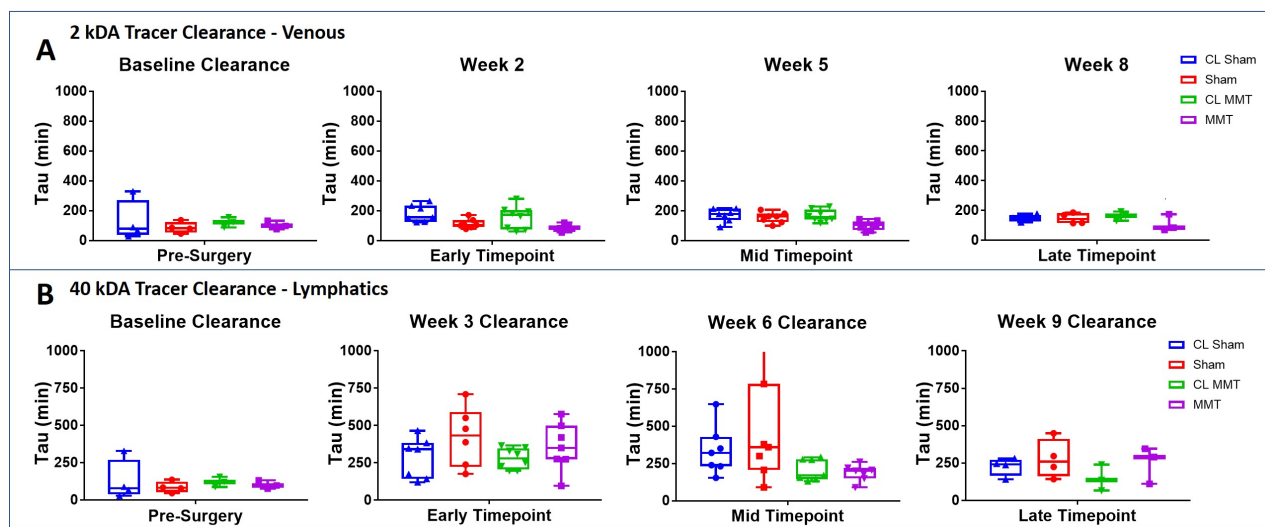


Figure 6: Venous and lymphatic clearance kinetics in a rat MMT-induced OA model. The left hindlimbs of rats underwent either Sham-surgery or MMT-surgery and their respective right hindlimbs were not operated (CL-contralateral). Rats received an intra-articular injection of either 2 kDa (A) or 40kDa (B) PEG-NIR at 2/3-, 5/6-, or 8/9-weeks post-surgery to left (Sham or MMT) and right (CL Sham or CL MMT) hindlimbs. The clearance of the PEG-NIR tracers were assessed using our developed NIR imaging technology.

limbs (Figure 6B). At the early and late timepoints there were trends for increased retention (higher time constant) in the operated limbs compared to the contralateral controls. The current sample size is small, particularly given the variability after surgery and thus is underpowered. In year two, we will be increasing the sample size in these studies and taking the animals out to a later OA timepoint.

Ex Vivo Lymphatic Vessel Functional Studies

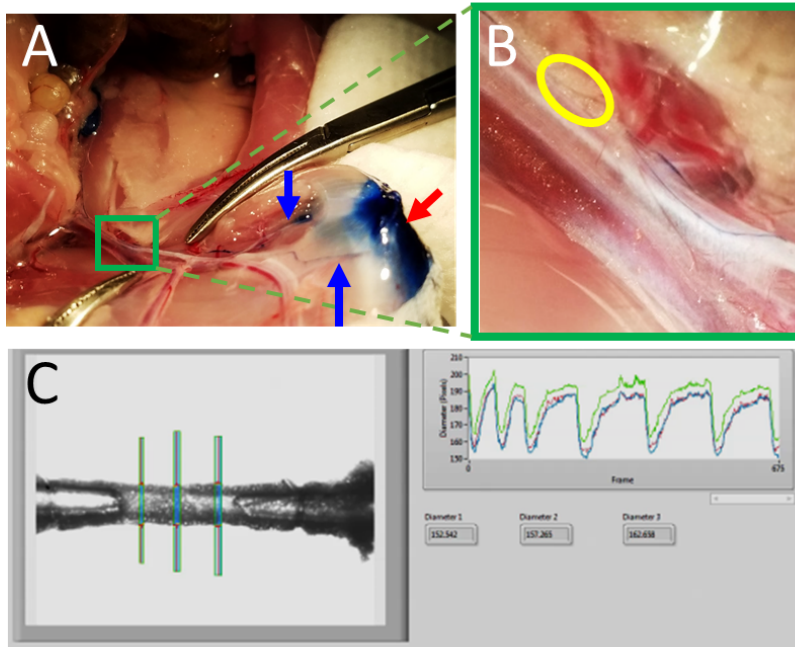


Figure 7: A, Dissection of lymphatic collecting vessel from rat hindlimb. Red arrow points at the knee joint of a rat that received an intra-articular injection of Evans Blue, a tracer that is picked up by lymphatic vessels. Blue arrows point at lymphatic vessels that drained from the knee joint. These vessels converge to collecting vessels found along the femoral artery (green box). B, Higher magnification of the green box (in A). Yellow ellipse reflects the lymphatic vessel that was isolated for *ex vivo* lymphatic vessel contractility assessment. C, Image of a mounted lymph vessel with pressure transducer and sensors attached. Colored lines are dynamic trackers to measure vessel diameter in real-time (right panel).

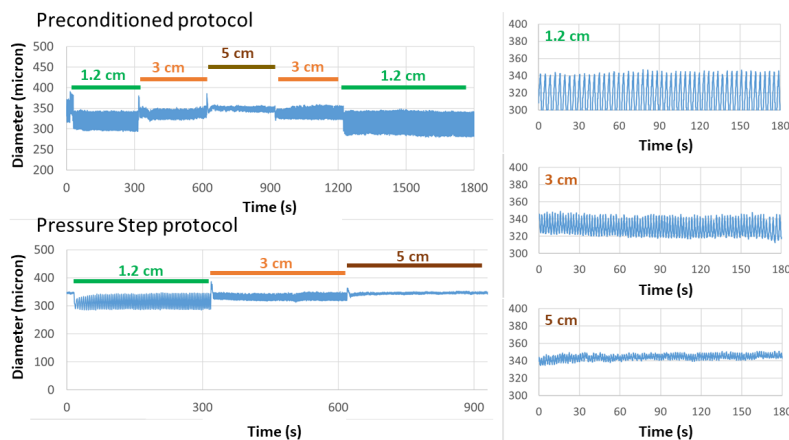


Figure 8: Representative lymph vessel diameter tracings in response to pressure changes during preconditioned protocol (to acclimate the vessel in the chamber) and during pressure step protocol. The right panels are magnified pressure step protocol.

In addition to knee clearance studies, we have also assessed lymphatic function by isolating lymphatic vessels that drain the knee joint. For this, we have assembled two *ex vivo* lymphatic vessel systems to assess the tonic and pressure-induced contractility of lymph vessels (Figure 7). In addition, the baseline contractile characteristics of these vessels have never been measured and given the regional heterogeneity of lymphatic contractility that has been reported in the literature, we also sought to establish baseline lymphatic contractility in healthy controls. Briefly, Evans Blue dye was injected into the knee capsule to determine which lymphatic vessels were responsible for draining the knee space. Once this determination was made, lymph vessels that drained the knee joint and ran along the femoral artery were isolated from the hindlimb of rats. The vessels were cleared of fat and interstitial tissues. About 1mm of vessels (absent of any valves) were mounted onto glass pipets that were attached to pressure transducers and sensors. Physiological saline solutions were perfused through the vessel and its diameter was tracked using an in-house Matlab algorithm (Figure 7). Isolated lymph vessels were preconditioned by loading the vessel to stepwise changes in

transmural pressure to acclimate the vessel in the chamber (Figure 8). After preconditioning, a pressure step protocol of 1.2, 3 and 5 cm of H₂O were applied for 5min each. This pressure step

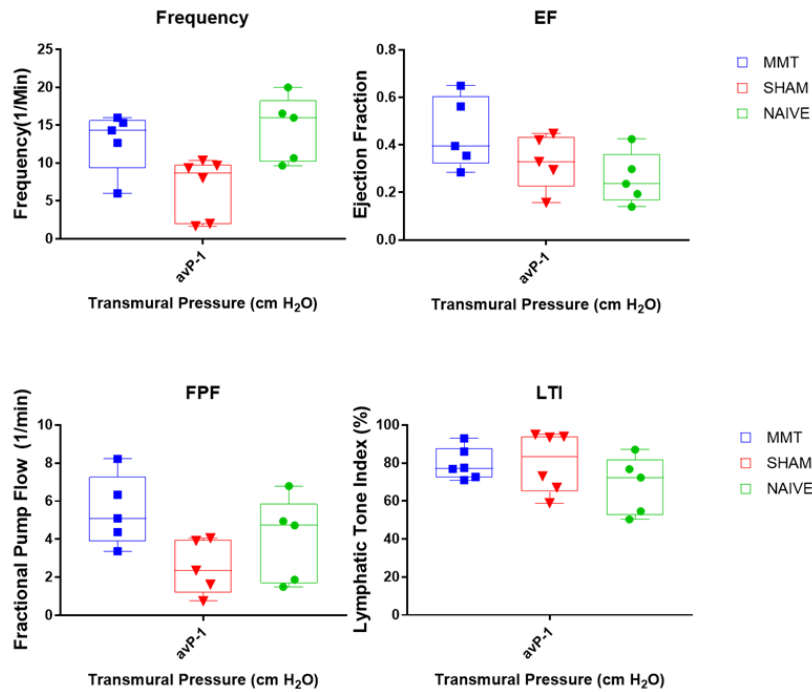


Figure 9: Contraction frequency, ejection fraction (EF), fractional pump flow (FPF) and lymphatic tone index (LTI) were measured for lymphatic vessels draining the MMT-operated knees, sham-operated knees, and naïve knees at 9-weeks after surgery. Data shown are for transmural pressure load of 1.2 cm H₂O.

protocol (Fig. 9). Vessels from OA knees showed elevated ejection fraction under low pressure, suggesting that these vessels are in a heightened contractile state. In the lymphedema literature, elevated contractility prior to disease onset has been shown to correlate with future lymphatic failure (Cintolesi, V *et al.*, *Lymph Res Biol*, 2016) and thus future work will focus on characterizing lymphatic function and remodeling responses at later time points of OA disease progression.

Summary of Accomplishments for Fiscal Year 1

We have made strong advances in our research for fiscal year 1. We have achieved the following set of milestones:

- 1) **Major Task 1:** Development of NIR technology and assessment of 2 and 40kDa PEG-NIR clearance for lymphatics. This was completed and resulted in a published manuscript.
- 2) **Approval of IACUC:** We have received approval for our animal studies at both Emory University and Georgia Institute of Technology in addition to the ACURO acceptance with the Department of Defense program.
- 3) **Major Task 2:** Assess the clearance of liposomes and large constructs from the knee joints using NIR technology. We have fabricated liposomes and their clearance kinetics will be further investigated in the coming months. We are also assessing the clearance of additional

biomaterials and particles found in the joint including hyaluronan. These will provide a comprehensive understanding of joint clearance and homeostasis in OA and will enable a new platform of particles, which are currently used to treat OA in the clinic and can potentially become carriers for various regenerative therapies.

- 4) **Major Task 3:** We have comprehensively characterized OA progression and development in the rat MMT model and see characteristic features of early-, middle- and late-stage OA which can be used to correlate to differences in lymphatic function and clearance kinetics. We have begun to assess the clearance of 2 and 40kDa PEG-NIR at these various stages of OA development and progression. We have preliminary data suggesting that 40kDa PEG-NIR clearance (specifically by lymphatics) is hindered in MMT-induced OA rats. We will confirm these findings with additional animals. In addition, we have assembled two new *ex vivo* lymphatic vessel systems to measure vessel contractility and function, have determined the routes of lymphatic clearance from the knee joint to lymphatics, and have measured lymphatic function of isolated vessels in our rat models at the 9-week time point.

Unmet goals:

Troubleshooting the fabrication and particularly the purification process with the surface bound PEG liposomes along with applying the dual label (PEG bound and encapsulated fluorophores) presented some unexpected challenges. There was an initial learning curve as we established new protocols and required new training to optimize this process. We can now fabricate liposomes with the surface bound PEG in both sizes and label the liposomes as proposed. We can encapsulate fluorophores and can label the PEG polymer with a second fluorophore. We have begun *in vivo* and *in vitro* experiments with the individual labeled particles for stability, release and clearance. We are finalizing the optimal ratios of dyes for the dual label protocol. We have made substantial progress on the labeling protocols and expect to get back on track for major Task 2 in the Fall of 2019. During the troubleshooting phase for liposome synthesis we made substantial progress on Aim 2. We are currently beginning work on Aim 3.

What opportunities for training and professional development has the project provided?

These accomplishments were performed by our rigorous team of investigators at both sites, Emory University and Georgia Institute of Technology (GA Tech). The team of 9 scientists met monthly to present and discuss the ongoing data and the progress of the Department of Defense research project. This provided opportunity for graduate students, post-doctorates, and investigators to exchange ideas and assisted with any problems across institutions. Within each institution, graduate students and post-doctorates met weekly with their respective principal investigators to review studies and to plan for the week.

Hands-on technical training was provided to all graduate students at each site. Dr. Doan trained personnel at Emory and Dr. Nepiyushchikh trained students at GA Tech. Dr. Nepiyushchikh has specialized expertise with lymphatic vessel isolation and *ex vivo* functional analysis; and, she trained Mr. Bernard on this unique technique during the first year of the project.

In addition to laboratory training, scientists received professional career development by attending and presenting at national science conferences and symposium.

How were the results disseminated to communities of interest?

In addition to presenting at regional and national conferences (see presentation list below), we have published our findings in peer-reviewed journals, including [ACTA Biomaterialia](#) and [European Cells and Materials](#).

What do you plan to do during the next reporting period to accomplish the goals?

As we move forward with our project, we will complete Aim 1 this fall and will primarily focus on Specific Aim 2 of the project, to determine the effect of osteoarthritis on lymphatic function and structure. We currently have animals that are in extreme late stage OA and will be taken down shortly for histologic analysis of lymphatic architecture. Our preliminary work suggests that lymphatic function may be altered at mid-stage of OA and these alterations are specific to lymphatic uptake and not venous uptake. We will provide additional evidence by assessing hyaluronan and liposome clearance from the knee joint in the face of OA. In addition, we have hired an additional post-doctorate with chemical engineering expertise (to begin in October) to fabricate the drug carriers and perform additional *in vivo* experiments. Near the end of year 2, we will determine the payload of resolvins in liposomal carriers and the release kinetics *in vitro*. The completion of these goals will poise us well into year 3 where we will determine the efficacy of resolvin drug delivery via intra-articular injection for osteoarthritis.

4. IMPACT:

What was the impact on the development of the principal discipline(s) of the project?

The use of NIR imaging to assess knee clearance in a small animal model (such as rat) is a unique technique and provides an unmet technology to address the impact size- and charge-based particle trafficking from diseased joints and overall joint homeostasis. Also, this technique allows for an ability to track drug delivery, drug retention and its release from the joint. This is critical to determine the efficacy of intra-articular injection of drugs and therapeutics to treat osteoarthritis. Because osteoarthritis is a chronic disease, the retention of drugs, and their potential to target downstream lymph nodes specific to the diseased joint within the affected joint is imperative for prolonged treatment.

What was the impact on other disciplines?

In addition to osteoarthritis, the use of NIR imaging to increase our understanding of factors involved in clearance can be applied to other joint diseases, including rheumatoid arthritis and synovitis. These joint diseases may result from an impairment of lymphatic function and thus clearance measurements may shed light to their deficits.

What was the impact on technology transfer?

Nothing to report here.

What was the impact on society beyond science and technology?

Nothing to report here.

5. CHANGES/PROBLEMS:

Nothing to report here.

Actual or anticipated problems or delays and actions or plans to resolve them

As mentioned previously, we had some troubleshooting and optimization on the liposomal fabrication which delayed our progress on major task 2. We have optimized these protocols and are conducting *in vivo* experiments now.

Changes that had a significant impact on expenditures

Nothing to report here.

Significant changes in use or care of human subjects, vertebrate animals, biohazards, and/or select agents

Significant changes in use or care of human subjects

This project does not use human subjects.

Significant changes in use or care of vertebrate animals

No significant changes to our use or care of vertebrate animals.

Significant changes in use of biohazards and/or select agents

No significant changes to use of biohazards and/or select agents.

6. PRODUCTS:

Publications, conference papers, and presentations

Journal publications.

- 1) Doan TN, Bernard FC, McKinney JM, Dixon JB, Willett NJ. Endothelin-1 inhibits size dependent lymphatic clearance of PEG-based conjugates after intra-articular injection into the rat knee. ACTA Biomaterialia Vol 93, 15 July 2019, 270-281. Published and federal support was acknowledged.
- 2) McKinney JM, Doan TN, Wang L, Deppen J, Reece DS, Pucha KA, Ginn S, Levit RD, Willett NJ. Therapeutic efficacy of intra-articular delivery of encapsulated human mesenchymal stem cells on early stage osteoarthritis. Eur Cell Mater. 2019 Jan 29, 37:42-59. Published and federal support was acknowledged.

Books or other non-periodical, one-time publications.

Nothing to report here.

Other publications, conference papers and presentations.

Presentations that acknowledged Department of Defense funding:

- 1) Bernard, F. C., Doan, T. N., McKinney, J. M., Dixon, J. B., Willett, N. J. Endothelin-1 Inhibits Clearance of Nanoparticles from Rat Knees. Biomedical Engineering Society Annual Meeting, Atlanta, Georgia, Oct 2018 (Podium).
- 2) McKinney, J. M., Doan T. N., Pucha A., Wang L., Weinstock L. D., Wood L., Levit R. D. & Willett N. J. Therapeutic efficacy of intra-articular delivered encapsulated human mesenchymal stem cells on osteoarthritis. Biomedical Engineering Society Meeting, Atlanta, GA, Oct 2018 (Podium).
- 3) McKinney, J. M., Doan T. N., Wang L., Deppen J., Weinstock L. D., Pucha A., Wood L., Levit R. D., & Willett N. J. Therapeutic efficacy of intra-articular delivered encapsulated human mesenchymal stem cells on osteoarthritis. Symposium on Regenerative Rehabilitation, Seattle, WA, Oct 2018 (Poster).
- 4) Doan TN, Bernard FC, McKinney JM, Dixon JB, Willett NJ. Endothelin-1 inhibits lymphatic clearance of different sized nanoparticles from intra-articular injection into rat knees. Orthopaedics Research Society, Austin, TX, Feb 2019 (Poster).
- 5) McKinney, J. M., Doan T. N., Pucha A., Wang L., Weinstock L. D., Wood L., Levit R. D., & Willett N. J. Therapeutic efficacy of intra-articular delivered encapsulated human mesenchymal stem cells on late stage osteoarthritis. Regenerative Medicine Workshop, Charleston, SC, Mar, 2019 (Podium).
- 6) McKinney, J. M., Doan T. N., Pucha A., Wang L., Weinstock L. D., Wood L., Levit R. D., & Willett N. J. Therapeutic efficacy of intra-articular delivered encapsulated human mesenchymal stem cells on osteoarthritis. Musculoskeletal (MSK) research symposium, Atlanta, GA, Apr, 2019 (Poster).

Presentations that acknowledged Department of Defense funding (continued):

7) Bernard, F. C., Doan, T. N., Nepiyushchikh, Z. V., McKinney, J. M., Dixon, J. B., Willett, N. J. Ex vivo and In Vivo Assessment of Femoral Lymphatic Vessel Function in Rats. Lymphatic Forum, Austin, Texas, May 2019 (Poster).

8) Bernard, F. C., Doan, T. N., Nepiyushchikh, Z. V., McKinney, J. M., Dixon, J. B., Willett, N. J. Multiscale assessment of rat femoral lymphatic function using *in vivo* NIR imaging and *ex vivo* lymphatic vessel perfusion device. Musculoskeletal Research Symposium, Atlanta, Georgia, May 2019 (Poster).

9) Liebman LN, Willett NJ, García AJ, Dixon JB. Dual-Function Liposomes for Lymphatics in Osteoarthritis. T32 Southeast Biotechnology Workshop, North Carolina State University, July 2019 (Poster).

- **Website(s) or other Internet site(s)**

Nothing to report here.

- **Technologies or techniques**

Nothing to report here.

- **Inventions, patent applications, and/or licenses**

Nothing to report here.

- **Other Products**

Nothing to report here.

7. PARTICIPANTS & OTHER COLLABORATING ORGANIZATIONS

Participants at Emory University

1) Nick Willett

Project Role: Principal Investigator at Emory University

Research ID: ORCID ID 0000-0003-3421-2549

Month worked: 2.4

Contribution to Project: Dr. Willett has led the overall project and managed the team on the Emory side. His team on the Emory side has begun in vivo clearance studies on OA animals. He has managed the overall experimental design and direction for the experiments on the Emory side and facilitates regular communication and collaboration with the Georgia Tech side. He was corresponding and senior author on the two publications that were supported by this work.

Funding Support: N/A

2) Thanh Doan

Project Role: Instructor

Research ID: 0000-0001-9079-9087

Month worked: 9 months

Contribution to Project: Dr. Doan organized the monthly Emory/GA Tech meetings and assisted with the preparation of this annual report. In addition to administrative responsibilities, Dr. Doan trained and assisted junior scientists at both the Emory and GA Tech sites. He was hands-on with knee clearance studies, *ex vivo* lymphatic vessels studies and assessment of bone/cartilage phenotypes in the rat medial meniscus transection model for osteoarthritis. He was lead author on the manuscript that was published.

Funding Support: N/A

3) Jarred Kaiser

Project Role: Instructor

Research ID: 0000-0001-9373-2961

Month worked: 6

Contribution to Project: Dr. Kaiser has focused on developing therapeutics to improve lymphatic function and resolution of inflammation during post-traumatic osteoarthritis. Dr. Kaiser purchased and set up the NIR imaging system on the Emory side. He has begun performing clearance studies.

Funding Support: N/A

4) Jay McKinney

Project Role: Graduate Student

Research ID: N/A

Month worked: 9

Contribution to Project: Mr. McKinney has performed work in quantitatively evaluating cartilage composition and morphology, subchondral bone morphology and osteophyte morphology using EPIC-uCT. Quantitative data has been collected for early- (3 week), mid- (6 week) and late- (12 week) stages of osteoarthritis.

Funding Support: N/A

Participants at Georgia Institute of Technology

1) Brandon Dixon

Project Role: Principal Investigator at GA Tech

Research ID: Y-1712-2019

Month worked: 1 month

Contribution to Project: Dr. Dixon oversaw the work being performed at Georgia Tech including the supervision of Dr. Nepiyushchikh, Fabrice Bernard, and Lauren Liebman. Dr. Dixon supervises the NIR imaging work and provides expertise in lymphatic biology and physiology. He also assisted with setting up the Emory side with NIR imaging capabilities comparable to those already in place at Georgia Tech.

Funding Support:

2) Andres Garcia

Project Role: Investigator at GA Tech

Research ID: 0000-0001-6602-2518

Month worked: 0.5

Contribution to Project: Dr. Garcia directs the design and characterization of liposome delivery vehicle. He co-advises the PhD student, Lauren Liebman, with Dr. Dixon.

Funding Support: N/A

3) Zhanna Nepiyushchikh

Project Role: Research Associate

Research ID: N/A

Month worked: 6

Contribution to Project: Dr. Nepiyushchikh directed and performed the *ex vivo* lymphatic vessels studies and trained graduate students at GA Tech. She also oversees the histological analysis of lymphatic structures, and performed the initial lymphatic flow mapping and characterization in the knee space.

Funding Support: N/A

4) Fabrice Bernard

Project Role: Graduate Student

Research ID: 0000-0002-6374-896X

Month worked: 6

Contribution to Project: Mr. Bernard synthesized the NIR-tracers for this project, assisted with knee clearance studies, and assisted with the *ex vivo* lymphatic vessels studies, including performing the majority of the post-processing analysis and synthesis of the data.

Funding Support: NIH RO1 Diversity Supplement

5) Lauren Liebman

Project Role: Graduate Student

Research ID: 0000-0002-3491-0788

Month worked: 5

Contribution to Project: Ms. Liebman worked in the area of biomaterials, specifically designing, synthesizing, and characterizing liposomes for joint clearance assessment.

Funding Support: NIH T32 Training Grant for Cell and Tissue Engineering (effective 8/15/19 and onward)

Funding Support: N/A

Has there been a change in the active other support of the PD/PI(s) or senior/key personnel since the last reporting period?

Nothing to report.

What other organizations were involved as partners?

No other organization was involved.

8. SPECIAL REPORTING REQUIREMENTS

COLLABORATIVE AWARDS: Dr. Nick Willett leads the group at the Emory site and Dr. Brandon Dixon leads the group at the GA Tech site. Dr. Andres Garcia is a collaborating investigator at the GA Tech site. Their groups' efforts are specified in the SOW. Dr. Willett and Dr. Doan both have office spaces at Emory and GA Tech and they visit both sites weekly.

9. APPENDICES:

- 1) Doan TN, Bernard FC, McKinney JM, Dixon JB, Willett NJ. Endothelin-1 inhibits size dependent lymphatic clearance of PEG-based conjugates after intra-articular injection into the rat knee. ACTA Biomaterialia Vol 93, 15 July 2019, 270-281. Published and federal support was acknowledged.
- 2) McKinney JM, Doan TN, Wang L, Deppen J, Reece DS, Pucha KA, Ginn S, Levit RD, Willett NJ. Therapeutic efficacy of intra-articular delivery of encapsulated human mesenchymal stem cells on early stage osteoarthritis. Eur Cell Mater. 2019 Jan 29, 37:42-59. Published and federal support was acknowledged.

PR171379: Engineering biomaterial-based therapies for improved lymphatic function and the resolution of chronic inflammation in post-traumatic osteoarthritis



PI: Dr. Brandon Dixon, Georgia Tech Research Corporation, Georgia

Budget: \$1,029,471.00

Topic Area: Peer-Reviewed Medical Research Program Mechanism: W81XWH-17-PRMRP-IIRA

Research Area(s): 0800

Award Status: 8/15/18 through 8/14/19

Study Goals:

This PRMRP grant is to develop biomaterial-based therapies that can be integrated with imaging modalities to both: 1) elucidate the role of lymphatic function in normal and diseased joints; and 2) promote joint clearance and the resolution of chronic inflammation by delivering inflammation resolving lipid mediators using controlled-release nanoparticles. Our **central hypothesis** is that lymphatic function is a critical component in OA disease progression and regenerative therapies that improve lymphatic function and the resolution of chronic inflammation will attenuate OA disease development and progression.

Specific Aims:

Aims 1: To develop a set of biomaterial-based tools to quantitatively interrogate lymphatic clearance function.

Aims 2: To evaluate lymphatic function during the pathogenesis of OA in the rat medial meniscus transection (MMT)-induced OA model.

Aims 3: To engineer novel intra-articular therapeutics to improve lymphatic function and resolution of inflammation during post traumatic OA.

Key Accomplishments and Outcomes:

Publications:

1) Doan TN, Bernard FC, McKinney JM, Dixon JB, Willett NJ. Endothelin-1 inhibits size dependent lymphatic clearance of PEG-based conjugates after intra-articular injection into the rat knee. ACTA Biomaterialia Vol 93, 15 July 2019, 270-281. Published and federal support was acknowledged.

2) McKinney JM, Doan TN, Wang L, Deppen J, Reece DS, Pucha KA, Ginn S, Levit RD, Willett NJ. Therapeutic efficacy of intra-articular delivery of encapsulated human mesenchymal stem cells on early stage osteoarthritis. Eur Cell Mater. 2019 Jan 29, 37:42-59. Published and federal support was acknowledged.

Patents: none to date

Funding Obtained: none to date



Full length article

Endothelin-1 inhibits size dependent lymphatic clearance of PEG-based conjugates after intra-articular injection into the rat knee [☆]

Thanh N. Doan ^{a,b}, Fabrice C. Bernard ^c, Jay M. McKinney ^{a,b,c}, J. Brandon Dixon ^{d,e}, Nick J. Willett ^{a,b,c,e,*}

^a Atlanta Veteran's Affairs Medical Center, 1670 Clairmont Road, Decatur, GA 30033, USA

^b Department of Orthopaedics, Emory University, 59 Executive Park South, Atlanta, GA 30329, USA

^c Wallace H. Coulter Department of Biomedical Engineering, Georgia Institute of Technology and Emory University, 313 Ferst Drive, Atlanta, GA 30332, USA

^d Department of Mechanical Engineering, Georgia Institute of Technology, 801 Ferst Drive, Atlanta, GA 30332, USA

^e Parker H. Petit Institute for Bioengineering and Bioscience, Georgia Institute of Technology, 315 Ferst Dr. NW, Atlanta, GA 30332, USA

ARTICLE INFO

Article history:

Received 5 October 2018

Received in revised form 4 April 2019

Accepted 10 April 2019

Available online 12 April 2019

Keywords:

Lymphatics

Intra-articular injection

Rat knees

NIR imaging

ABSTRACT

Clearance of particles from the knee is an essential mechanism to maintain healthy joint homeostasis and critical to the delivery of drugs and therapeutics. One of the limitations in developing disease modifying drugs for joint diseases, such as osteoarthritis (OA), has been poor local retention of the drugs. Enhancing drug retention within the joint has been a target of biomaterial development, however, a fundamental understanding of joint clearance pathways has not been characterized. We applied near-infrared (NIR) imaging techniques to assess size-dependent *in vivo* clearance mechanisms of intra-articular injected, fluorescently-labelled polyethylene glycol (PEG-NIR) conjugates. The clearance of 2 kDa PEG-NIR ($\tau = 171 \pm 11$ min) was faster than 40 kDa PEG-NIR ($\tau = 243 \pm 16$ min). 40 kDa PEG-NIR signal was found in lumbar lymph node while 2 kDa PEG-NIR signal was not. Thus, these two conjugates may be cleared through different pathways, i.e. lymphatics for 40 kDa PEG-NIR and venous for 2 kDa PEG-NIR. Endothelin-1 (ET-1), a potent vasoconstrictor of vessels, is elevated in synovial fluid of OA patients but, its effects on joint clearance are unknown. Intra-articular injection of ET-1 dose-dependently inhibited the clearance of both 2 kDa and 40 kDa PEG-NIR. ET-1 caused a 1.63 ± 0.17 -fold increase in peak fluorescence for 2 kDa PEG-NIR and a 1.85 ± 0.15 -fold increase for 40 kDa PEG-NIR; and ET-1 doubled their clearance time constants. The effects of ET-1 were blocked by co-injection of ET receptor antagonists, bosentan or BQ-123. These findings provide fundamental insight into retention and clearance mechanisms that should be considered in the development and delivery of drugs and biomaterial carriers for joint diseases.

Statement of Significance

This study demonstrates that *in vivo* knee clearance can be measured using NIR technology and that key factors, such as size of materials and biologics, can be investigated to define joint clearance mechanisms. Therapies targeting regulation of joint clearance may be an approach to treat joint diseases like osteoarthritis. Additionally, *in vivo* functional assessment of clearance may be used as diagnostics to monitor progression of joint diseases.

© 2019 Acta Materialia Inc. Published by Elsevier Ltd. All rights reserved.

[☆] Part of the Drug Delivery for Musculoskeletal Applications Special Issue, edited by Robert S. Hastings and Professor Johnna S. Temenoff.

* Corresponding author at: 1670 Clairmont Road, Room 5A-115, Decatur, GA 30033, USA.

E-mail addresses: thanh.doan@emory.edu (T.N. Doan), fabrice.bernard@emory.edu (F.C. Bernard), jay.m.mckinney@emory.edu (J.M. McKinney), dixon@gatech.edu (J.B. Dixon), nick.willett@emory.edu (N.J. Willett).

1. Introduction

The homeostatic maintenance of joint tissues and synovial fluid is regulated by multiple mechanisms including blood flow, plasma concentration, microvascular permeability, and lymphatic clearance [1,2]. Recent evidence has suggested that proper lymphatic function is critical to joint health and resolution of inflammation [3]. During joint disease, such as arthritis, the production and consumption of various metabolites, including proteins, cytokines and

proteoglycans within the joints, are altered; understanding the clearance kinetics and mechanism of these factors may provide insight into potential therapeutic delivery strategies as well as therapeutic targets. The secreted proteins and degraded extracellular matrix during joint disease diffuse passively through hyaluronan lattices, the synovial matrix, and then into capillaries of the synovium. Low-molecular weight molecules diffuse along their concentration gradients and are dominantly taken up into venous vessels. On the other hand, high-molecular weight molecules as well as cells are cleared primarily through the initial lymphatic vessels in the synovium.

Much of our understanding of joint physiology and clearance relies on observations from several decades ago—molecules above a certain molecular weight appear to clear at rates independent of their size, suggesting that the lymphatics are the primary route of clearance of large molecules from the joint [4–6]. Pioneering work by Simkin and colleagues simultaneously measured the clearance of two different sized-tracers from the joint to provide an indirect measurement of plasma flow and lymphatic drainage from knee effusions of patients with rheumatoid arthritis (RA) or osteoarthritis (OA); they found that clearance of proteins from the joint space is significantly slower in OA compared to RA [7]. However, all of these differential isotope studies were conducted in late-stage diseased patients and 30 years later we still do not know how these measurements compare to early stage disease or healthy patients [8]. Recent work in human patients has demonstrated a decrease in lymphatic capillary density in the synovia of OA patients, suggesting an impairment of lymphangiogenesis [9]. However, in pre-clinical studies using an injury-induced OA model in mice, lymphatic capillary density was found to be increased in OA animals, while the number of mature collecting vessels was markedly decreased in cases of severe OA. More importantly, functional drainage from the knee space was reduced which is consistent with reduced collecting vessel density and reduced drainage in OA [10]. In a follow up study, it was found that systemic delivery of therapeutic to promote lymphangiogenesis could attenuate OA disease progression in this model suggesting that lymphatics function and clearance mechanisms may be a promising therapeutic target [11].

Traditionally, tools used to assess *in vivo* clearance kinetics from joints have relied on radioactive-labelled materials [8,12–15] and in some instances, euthanizing animals for measurement at various time points [16]. More recently, near-infrared dyes, such as indocyanine green (ICG) [17] and Cyanine 5.5, have proven to be alternatives when paired with sophisticated imaging hardware [18]. When ICG is unbound, it binds to native proteins and thus preferentially drains into lymphatics when delivered intradermally [19,20]. However, Weiler et al. [21] recently showed that repeat injections of ICG caused a reduction in lymphatic pump function and an enlargement of the down-stream draining lymph nodes, while the dye itself is retained at detectable levels within the injection site for up to 2 weeks. We have recently developed methods to quantify lymphatic pump function and transport non-invasively in the context of various lymphatic and inflammatory insults using rodent models [19,21,22].

Lymphatic vessels are known to be regulated by vasoactive peptides such as angiotensin, serotonin and endothelin. Endothelin-1 (ET-1) is a soluble secreted protein that is a potent vasoconstrictor of blood and lymphatic vessels. For lymphatic regulation, ET-1 has been shown to be a potent constrictor of lymphatic vessels isolated from human thoracic duct [23] and rat mesentery [24]. In addition, ET_B receptors are expressed by lymphatic endothelial cells [25]. In the context of diseased joints, clinical evidence has shown that ET-1 is increased in the synovial fluid and is thought to be correlated to the severity of knee osteoarthritis [26–29]. Within the synovium, (ET-1) can be expressed by synoviocytes [30]. ET receptors can be

expressed by articular chondrocytes and levels are increased during ageing [31–33]. Further, upregulation of ET-1 [34] can lead to increased expression of metalloproteinases and thus degradation of cartilage matrix which is indicative of arthritis [35]. There is building evidence that pharmacological inhibition of ET receptors may ameliorate arthritis progression [36]. However, the implication for ET-1 has been largely through a direct effect on chondrocytes and a potential role in clearance mechanism remains unknown.

Herein, we apply NIR imaging technology to quantify the clearance kinetics of nanosized PEG-NIR conjugates from rat knees and demonstrate that the biologic ET-1 inhibits clearance of these conjugates. Moreover, there is a differential uptake of different nanosized PEG-NIR conjugates into the venous or lymphatic systems. The effects of ET-1 on knee clearance may elucidate its action during arthritis development.

2. Materials and methods

2.1. Ethical approval

This study was approved by IACUC committees at Georgia Institute of Technology (#A15019) and at Veteran's Administration (#V004-15) in Atlanta, GA. Sasco Sprague Dawley male rats (Charles River Laboratories) were used for all studies reported herein. Rats (between 3 and 9 months old) were age-matched (identical date of birth) with similar weights (<50 g difference) as their controls within an experiment (i.e. 2 kDa PEG-NIR or 40 kDa PEG-NIR alone). Time constants were not correlated to age of the animals, $R = -0.277$ and 0.274 for 2 kDa PEG-NIR and 40 kDa PEG-NIR, respectively. Data were pooled to calculate average values.

2.2. Reagents

Endothelin-1 (21 amino acids), bosentan and BQ-123 were purchased from Sigma-Aldrich. 2 kDa PEG amine and 40 kDa PEG amine were purchased from JenKem Technology.

2.2.1. Synthesis of PEG-NIR materials

2 kDa or 40 kDa amine polyethylene glycol (PEG) was conjugated to near infrared (NIR) dye, IRDye 800CW NHS ester (LI-COR Biosciences) according to manufacturer's instruction (LI-COR). Briefly, 1:8 molar ratio (mol/mol) of NIR dye to PEG were incubated in Dulbecco's Phosphate-Buffered Saline (PBS; Life Technologies) at pH 8.5 for 24 h at room temperature with gentle stirring. The mixture was lyophilized and stored at -20°C . PEG-NIR aliquots were thawed and resuspended with sterile 0.9% NaCl for *in vivo* studies.

To determine the optimal ratio of PEG to NIR-dye reaction, differing concentrations of 40 kDa amine PEG were reacted with a fixed concentration of IRDye 800CW NHS ester at room temperature overnight. The reaction mixtures were separated on 8% SDS-PAGE (Bio-Rad) and fluorescent images were captured using the LI-COR Odyssey Infrared Imaging System.

2.2.2. Measurement of hydrodynamic diameter

ET-1 (Sigma-Aldrich), 2 kDa PEG or 40 kDa PEG were suspended in PBS to a final concentration of 1 mg/ml. The hydrodynamic diameter was measured using Zetasizer Nano ZS (Malvern Instruments Ltd., United Kingdom). The zeta potential for the linear 40 kDa PEG-NIR was -7.06 .

2.3. NIR imaging in rats

Sasco Sprague Dawley rats were anaesthetized with isoflurane (SomnoSuite, Kent Scientific) and hind limbs were shaved.

Intra-articular injections (anterior approach, 4–5 mm depth) were performed into the knee joints using 1 mL insulin syringes (Becton Dickinson). All reagents were diluted in 0.9% sterile saline and co-injected with total volume of 50 μ L. NIR images of rat knee joints were captured using an in-house, custom-built NIR imaging system [19,37]. The computer-driven system included a cooled EMCCD camera (Evolve eXcelon, Photometrics) attached to a stereo-microscope (Olympus) equipped with NIR band pass excitation and long pass emission filters and an automated shutter-controlled xenon arc lamp light source (Sutter Instrument Company). Fluorescence images were captured at various time points with fixed camera exposure time of 100 ms using MicroManager software. Animals recovered from anesthesia before the next time point was collected (unless otherwise stated). Animals were left *ad libitum* from time of injection to time of euthanasia.

With this *in vivo* NIR imaging technique, the clearance of materials from the knee space can be quantified. Using a custom MATLAB (Mathworks) code, the region of interest (ROI) for each image was determined by isolating the 5% most intense pixels. This ROI visually corresponded with the size and position of the knee space. Those pixels within the ROI were then averaged to obtain the mean fluorescence intensity. Increasing the ROI to 10, 15, 20, 25 and 50% most intense pixels yielded similar changes in fluorescence however, this also increased the number of background (non-fluorescent) pixels and thus decreased the signal-to-noise ratio (data not shown). Data points were fitted to a mono-exponential function (Origin software): $f(t) = y_0 + A e^{-(t/\tau)}$, where y_0 is the offset, t is time, A is normalized fluorescence at $t = 0$, and τ is time constant. At a minimum, 5 data points were collected within the first 24 h. The R^2 ranged from 0.976 to 0.999 with a mean of 0.990 ± 0.002 for mono-exponential fits of 2 kDa PEG-NIR clearance and from 0.979 to 0.999 with a mean of 0.993 ± 0.002 for mono-exponential fits of 40 kDa PEG-NIR clearance.

To verify the intra-articular injection technique, 2 and 40 kDa PEG-NIR was injected into rat knees and fluorescence and X-ray images were captured using In-Vivo Extreme (Bruker). Fluorescence was captured using 730 nm excitation band pass filter and 790 nm emission long pass filter with a camera exposure of 5 min. The overlay of the fluorescence and x-ray images allowed assessment of the dye location relative to the skeletal structures of the rat hindlimb.

2.4. Biodistribution of PEG-NIR conjugates in rats

Following intra-articular injection of 2 kDa or 40 kDa PEG-NIR into the left knee, rats were asphyxiated with CO_2 at 4 h post-injection. The bladder was imaged *in situ*. Lymphatic tissues (i.e. lumbar, popliteal and inguinal lymph nodes) and other systemic organs (i.e. heart, liver, lungs, spleen and kidneys) were dissected and placed in 24-well plates. Fluorescence images of tissues and organs were captured using in-house built NIR imaging system with camera exposure setting of 2000 ms. Quantification of fluorescence was performed using ImageJ software.

To determine if 40 kDa PEG-NIR was metabolized in lymph node, the isolated tissue was solubilized in RIPA buffer (ThermoFisher Scientific), centrifuged at 14,000 rpm for 10 min and supernatant was separated on SDS-PAGE. Urine was collected from bladder, centrifuged at 14,000 rpm for 10 min, diluted in RIPA buffer and separated on SDS-PAGE.

2.5. Statistical analysis

Data were represented as means \pm SE. Unless otherwise stated, a one-way ANOVA was performed with post ad hoc Tukey method for statistical significance (GraphPad Prism version 6.02). A p -value

less than 0.05 was considered significant. For biodistribution studies, a one-way ANOVA was performed with post ad hoc Bonferroni method.

3. Results

3.1. Synthesis of PEG-NIR

To optimize the synthesis of different sized PEG-NIR conjugates from the knee joint, 2 kDa and 40 kDa PEG's were conjugated to near-infrared (NIR) dye via NHS ester reactivity with amine. A reaction ratio of 1:8 of IRDye:PEG was found to maximize PEG-NIR conjugation while minimizing free dye and unconjugated PEG (Fig. 1a). The hydrodynamic diameters for 2 kDa PEG and 40 kDa PEG were 2.6 ± 0.2 nm and 11.9 ± 0.3 nm, respectively (Fig. 1b). The fluorescence intensities of both 2 and 40 kDa PEG-NIR dyes were linear within the range of 10–200 μ M (Fig. 1c). The half maximal normalized fluorescence concentrations were 85 ± 24 μ M and 202 ± 42 μ M for 2 kDa PEG-NIR and 40 kDa PEG-NIR ($p = 0.1599$), respectively. At concentrations above 200 μ M, the fluorescence intensity of PEG-NIR dyes decreased, which is suggestive of self-quenching.

3.2. *In vivo* clearance of PEG-NIR from the knee joint

For *in vivo* knee clearance studies, we injected 50 μ L of 100 μ M PEG-NIR (5 nmol) into rat knees. To determine the relative location of the dye, we captured fluorescence and X-ray images of rat knees before (Fig. 2) and after intra-articular injection. The dye intensity was highest at the knee joint (immediately after intra-articular injection) and decreased at subsequent times. Using our custom-built NIR imaging system, similar changes in fluorescence intensity could be observed when PEG-NIR conjugates were injected into rat knee joints. With this system, a camera exposure time of 100 ms was sufficient to assess the fluorescence change of PEG-NIR dyes. When the normalized averaged fluorescence intensity of the top 5% fluorescent pixels were plotted with respect to time (Fig. 3), the calculated time constant (τ) was 171 ± 11 min for 2 kDa PEG-NIR ($n = 10$) and 243 ± 16 min for 40 kDa PEG-NIR ($n = 11$; $p < 0.005$). The concentration and volume of tracer injected was identical thus the difference in clearance rate is attributed to the difference in size. The clearance kinetics of PEG-NIR was not due to residual free or unbound NIR dye in the mixture. When 2 kDa PEG and NIR dye were not given time to conjugate and injected into rat knee immediately (after mixing), the fluorescence signal remained elevated for more than 2 days and exhibited slower clearance rate (Supplementary Fig. 1). In addition, 40 kDa PEG-NIR that was purified through FPLC column showed similar kinetics as non-purified 40 kDa PEG-NIR. 2 kDa PEG-NIR could not be purified with FPLC and hence for direct comparisons, non-purified PEG-NIR's were used for this study. The clearance of an intermediate size PEG-NIR (13 kDa) was also significantly different from 2 and 40 kDa PEG-NIR (Supplementary Fig. 2). Further, addition of unlabeled PEG (equimolar) did not alter the clearance of 2 kDa or 40 kDa PEG-NIR conjugates as illustrated in Supplementary Fig. 3.

3.3. Biodistribution of PEG-NIR

Within the synovium, materials may be cleared through capillaries of venous vessels (for particles < 5 nm) and/or through initial lymphatics. To determine clearance pathways of these different sized PEG-NIR conjugates, tissues and organs were isolated 4 h post-injection, a time point where nearly two-third of injected

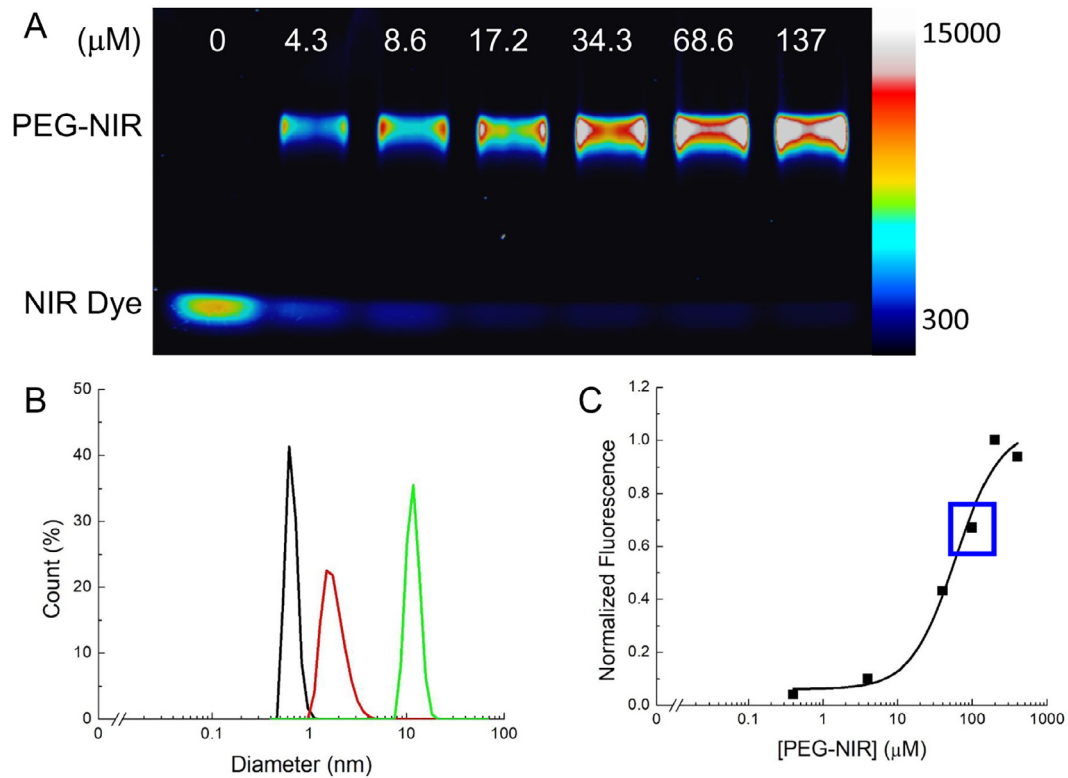


Fig. 1. Synthesis of PEG-NIR conjugates. A: Representative fluorescence image of SDS-PAGE separating IRDye 800CW NHS ester (lower band) and 40 kDa PEG-conjugated NIR dye (upper band). IRDye 800CW NHS ester (8.6 μM) was reacted with differing amounts of 40 kDa PEG and equivalent volume was loaded onto SDS-PAGE. B: Representative measurement of hydrodynamic diameter for ET-1 (black), 2 kDa PEG (red) and 40 kDa PEG (green) using Zetasizer Nano ZS ($n = 3$). C: Representative data of normalized fluorescence for 2 kDa PEG-NIR resuspended in sterile 0.9% NaCl. Data points were fitted to sigmoidal function (solid line). The 100 μM concentration (blue square) was used for *in vivo* studies. Similar profile was found for 40 kDa PEG-NIR.

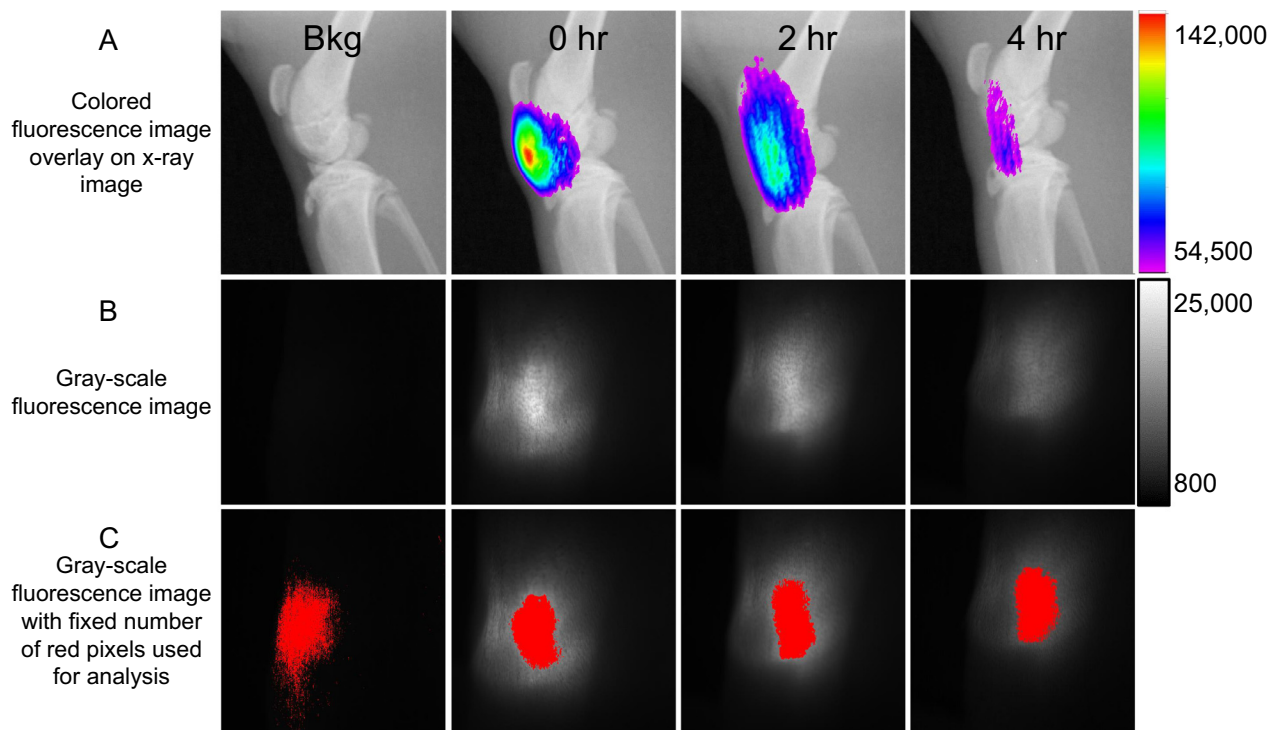


Fig. 2. Representative images of near infrared and x-ray images of rat knees with 40 kDa PEG-NIR. Intra-articular injection of 40 kDa PEG-NIR was administered to rat knee. Representative images of rat knee at various time points: before (background, bkg), immediately after 0, 2 and 4 h post dye injection were shown. A: X-ray images (black and white) and fluorescence images (pseudo-color) were captured using the In-Vivo Extreme imaging system. B: Fluorescence images (gray scale) were captured using a custom-built NIR imaging system. C: Same fluorescence images as in B with threshold red region. Threshold region represented the top 5% of pixels with the highest fluorescence intensities.

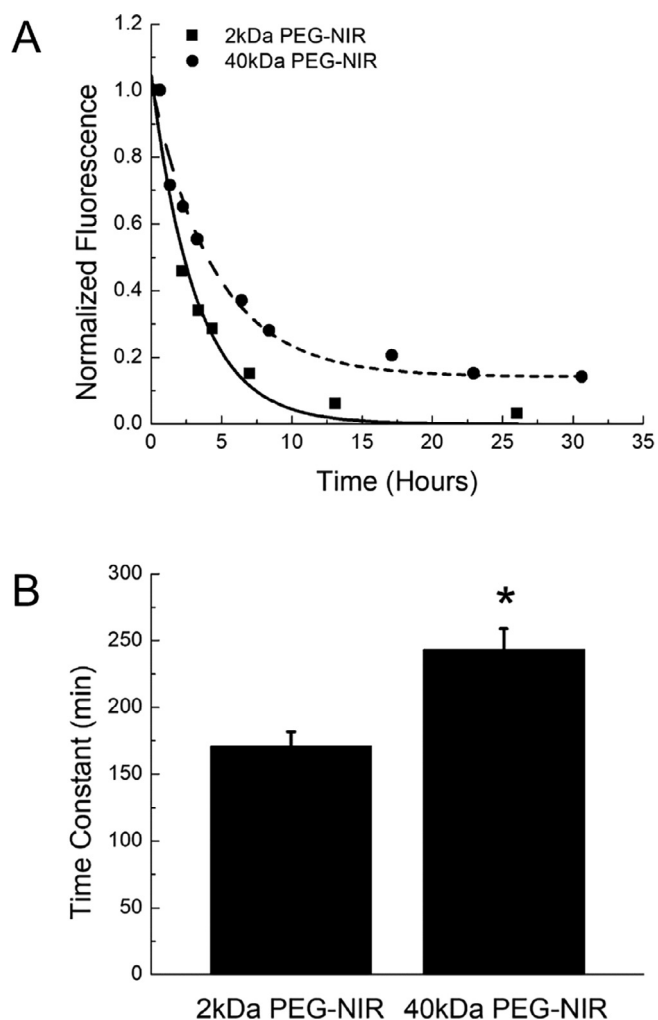


Fig. 3. Clearance of conjugates from rat knees. A: A representative clearance curve of 2 kDa (square; 1 representative curve from the 10 animals) and 40 kDa (circle; 1 representative curve from the 11 animals) PEG-NIR from rat knees. Solid and dashed lines were mono-exponential fits to 2 kDa and 40 kDa PEG-NIR data points, respectively. Bottom panel, average time constant for 2 kDa ($n = 10$) and 40 kDa PEG-NIR ($n = 11$; *denoted $p < 0.005$).

40 kDa PEG-NIR was cleared from the knee joint. In rats, fluorescence was significantly increased in the left lumbar lymph node of animals injected with 40 kDa PEG-NIR compared to left lumbar lymph node of naïve animals (Fig. 4). The lumbar node is known to collect materials drained from the knee joint [38]. 2 kDa PEG-NIR was not found in the lumbar lymph node, suggesting that this conjugate was not taken up by the lymphatic vessels or if so, not retained in the lumbar lymph node. The increased fluorescence of injected 40 kDa PEG-NIR was found for up to 24 h post-injection (data not shown). In addition to the lumbar lymph node, increased NIR signals were evident in the bladder for both 2 kDa and 40 kDa PEG-NIR administrations. No change in fluorescence was observed for any other tissues and organs examined, including popliteal lymph nodes, inguinal lymph nodes, heart, lung, liver, kidney and spleen.

To determine if 40 kDa PEG-NIR were broken down in the lymph node and/or urine, solubilized samples were separated on SDS-PAGE (Fig. 4d). The 40 kDa PEG-NIR conjugate was found in the lymph tissue and no free dye were detected. For urine, both the 40 kDa PEG-NIR and free dye were found. Additionally, PEG-

NIR conjugates did not degrade or react with other proteins or materials in synovial fluid (Supplementary Fig. 4).

3.4. Effect of a biologic on clearance of PEG-NIR conjugates

3.4.1. Endothelin-1 inhibited the clearance of 2 kDa PEG-NIR from the knee joint

To determine if biologics may influence the clearance of PEG-NIR conjugates within the knee joint, ET-1, a potent vasoconstrictor, was co-administered with 2 kDa PEG-NIR (Fig. 5). ET-1 (2.5 μg) significantly prevented the clearance of 2 kDa PEG-NIR for up to 100 ± 40 min ($p < 0.05$). During this initial inhibitory phase, ET-1 caused an increase in fluorescence within the knee space with a magnitude of 1.63 ± 0.17 ($p < 0.01$). After the ET-1 induced inhibitory phase, 2 kDa PEG-NIR was cleared with a calculated time constant of 374 ± 33 min ($p < 0.001$). The effects of ET-1 was dose-dependent *in vivo*. ET-1 effects on peak fluorescence (Fig. 5D) was significant at doses as low as 250 ng, suggesting that this parameter may be more sensitive to capturing the biological effects of ET-1 than time delay or time constant.

In a separate group of animals that were continuously kept under anesthesia after intra-articular injection, the ET-1 effect on peak fluorescence was less pronounced (Fig. 5A) than those that recovered from anesthesia before collecting the next data point (Fig. 5B, E). This suggests that joint distention and the subsequent convective transport and diffusion of ET-1 to surrounding tissues may facilitate ET-1 action on surrounding tissues.

3.4.2. ET-1 inhibited the clearance of 40 kDa PEG-NIR from knee joint

When ET-1 was co-administered with 40 kDa PEG-NIR, there was an inhibitory phase (Fig. 6), like that observed for ET-1 effect on 2 kDa PEG-NIR clearance. The time delay for 40 kDa PEG-NIR with 2.5 μg ET-1 was 164 ± 45 min and without ET-1 was 35 ± 10 min ($p < 0.001$). ET-1 (2.5 μg) significantly increased the peak fluorescence of 40 kDa PEG-NIR from 1.16 ± 0.08 (without ET-1) to 1.85 ± 0.15 ($p < 0.001$). ET-1 co-delivery also led to a significantly higher time constant of 507 ± 41 min for 40 kDa PEG-NIR compared to 40 kDa PEG-NIR alone ($p < 0.001$).

3.4.3. Specificity of ET-1 on knee clearance

To determine the specificity of ET-1, bosentan, a competitive antagonist for both ET_A and ET_B receptors, was co-injected with ET-1 and 2 kDa PEG-NIR (Fig. 7). Bosentan blocked the ET-1-induced changes to 2 kDa PEG-NIR clearance. The time constant for 2 kDa PEG-NIR with ET-1 was 408 ± 27 min and in the presence of bosentan, it was 154 ± 22 min ($p < 0.001$), a value that was not significant from the time constant of 2 kDa PEG-NIR alone (165 ± 27 min). Bosentan did not significantly alter ET-1 effects on time delay and peak fluorescence for 2 kDa PEG-NIR. Co-injection of an antagonist with specificity for the ET_A receptor, BQ-123, also prevented ET-1 induced changes to 2 kDa PEG-NIR clearance. Neither antagonists alone had any effect on 2 kDa PEG-NIR clearance (data not shown).

We also assessed the ability of bosentan and BQ-123 to compete against ET-1 effects on the clearance of 40 kDa PEG-NIR. Similar to that found for 2 kDa PEG-NIR, bosentan and BQ-123 significantly prevented ET-1-induced change on time constant (Fig. 8D). ET-1 shifted the time constant for 40 kDa PEG-NIR from 220 ± 13 min to 364 ± 17 min ($p < 0.001$) and with the addition of bosentan or BQ-123, the time constants were 209 ± 18 min or 219 ± 24 min, respectively ($p < 0.001$). Bosentan and BQ-123 did not have a significant effect on ET-1 induced changes to peak fluorescence.

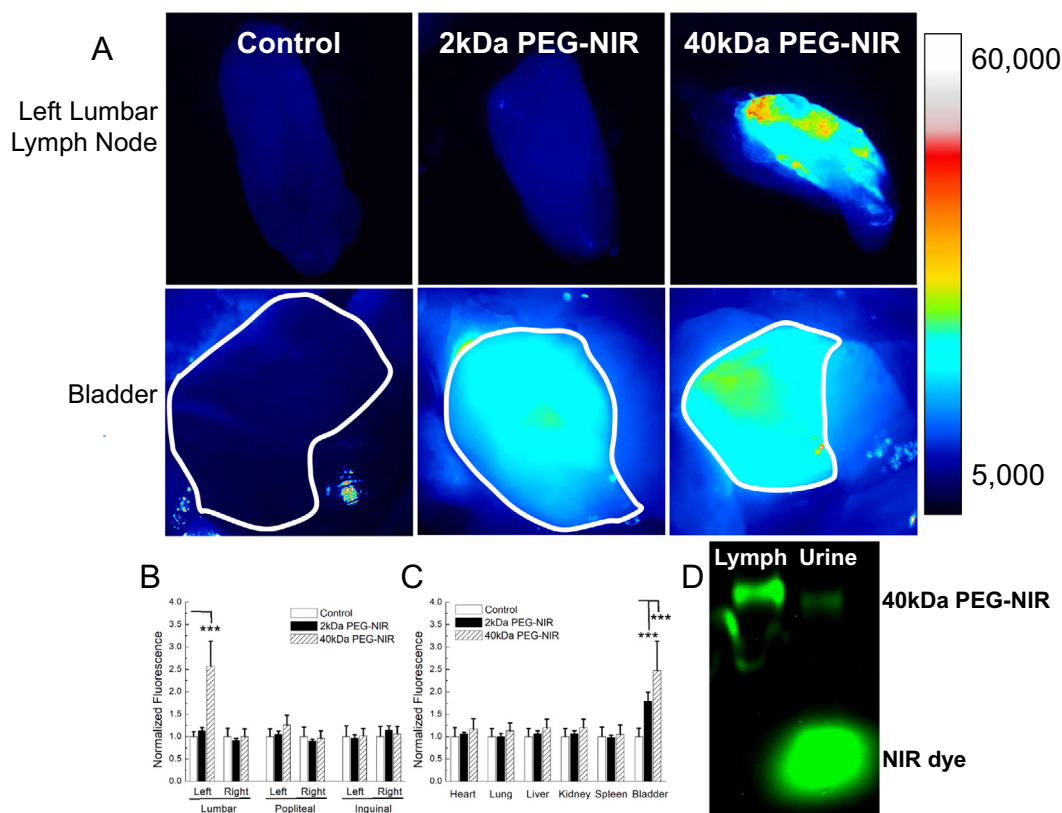


Fig. 4. Biodistribution of PEG-NIR from intra-articular injection into rat knees. A: Representative fluorescence images of left lumbar lymph nodes and bladders isolated from rats that were naïve (control) or injected with 2 kDa PEG-NIR or 40 kDa PEG-NIR into left knees. For the bladders, a white border was manually drawn, and this ROI was used to calculate the mean fluorescence intensity for the tissue. Mean fluorescence intensities were calculated for each lymphatic tissues (B) and organs (C). Significance was determined using one-way ANOVA and post hoc Bonferroni test with calculated p values to be < 0.001 (***) when compared to respective tissues from naïve animals. D: Representative image of SDS-PAGE ($n = 4$) loaded with solubilized left lumbar node (left lane) and urine (right lane) from a rat intra-articularly injected with 40 kDa PEG-NIR into the knee after 4 h.

4. Discussion

The clearance of materials and proteins from the knee joint is critical to normal joint homeostasis; measurement of these processes has historically been performed using radioactive tracers. This technique requires collecting synovial fluid samples over time which presents technical challenges in small animal models like the rat. More recently, near-infrared dyes and imaging techniques have enabled noninvasive longitudinal assessment of *in vivo* clearance kinetics [10,11,39,40]. We have employed a near-infrared imaging technique to assess the clearance of nanometer-sized molecules from rat knees. A variety of larger contrast agents have been utilized within the joint to characterize different features of joint homeostasis. Large, charged ionic contrast agents, like anionic Gd-DTPA²⁻ [41], Hexabrix 320 [42,43], CA⁴⁺ [44] and avidin [16], have been used to assess proteoglycan content of articular cartilage; however, these agents cannot be used to assess knee clearance kinetics since their *in vivo* binding and release kinetics to and from cartilage are not known. Here, we utilized PEGs as NIR tracking molecules because they are hydrophilic and electrostatically neutral and thus, not likely to bind to extracellular matrices of the joint or proteoglycans in the synovial fluid like hyaluronan, which is an anionic, non-sulfated glycosaminoglycan.

Assessment of fluorescence signal from probes injected into the knee joint is an indirect measurement of knee clearance. The measured fluorescence signal over time is a net result of diffusion and equilibration of materials within the synovial fluid, volumetric change of the joint space, passive diffusion of materials into the

synovium and their subsequent removal by the blood or lymphatic microcirculation. The initial rise in peak fluorescence of either 2 kDa PEG-NIR (occurs usually within 5–10 min) or 40 kDa PEG-NIR (occurs within 30–60 min) is most likely due to diffusion of the conjugates within the synovial fluid or to transient changes in synovial fluid volume after injection. It is unlikely that the rise in fluorescence is due to unquenching of the dye since we are using a PEG-NIR concentration that is within the linear range of fluorescence detection. Similar to our findings, Shi et al. [10] also reported a time delay of nearly an hour for clearance of indocyanine green (ICG) from mice knee. ICG binds to proteins *in vivo* and most typically, to albumin since it is an abundant soluble protein and can then be cleared by the lymphatic system.

Materials that are injected intra-articularly will clear by a process where they diffuse through the synovial fluid, pass through the synovial lining, diffuse into the synovium, and are cleared from the joint through capillaries. These processes can be calculated together as a bulk parameter or calculated in separate pieces to understand varying phases of this process. The calculated time constant reported herein did not include data points found in the delay (or lag) phase to minimize the initial diffusion differences of 2 kDa and 40 kDa PEG-NIR. We determined that the τ for 2 kDa PEG-NIR is about 1.4 times faster than 40 kDa PEG-NIR from rat knees. Previous studies have quantified clearance kinetics of materials with a variety of sizes. From Shi et al. [10] published work, we approximate the τ for ICG in mice knees at about ~ 140 min. Singh et al. [39] calculated the half-life of 500 nm particles designed for drug delivery to be 1.9 days after intra-articular

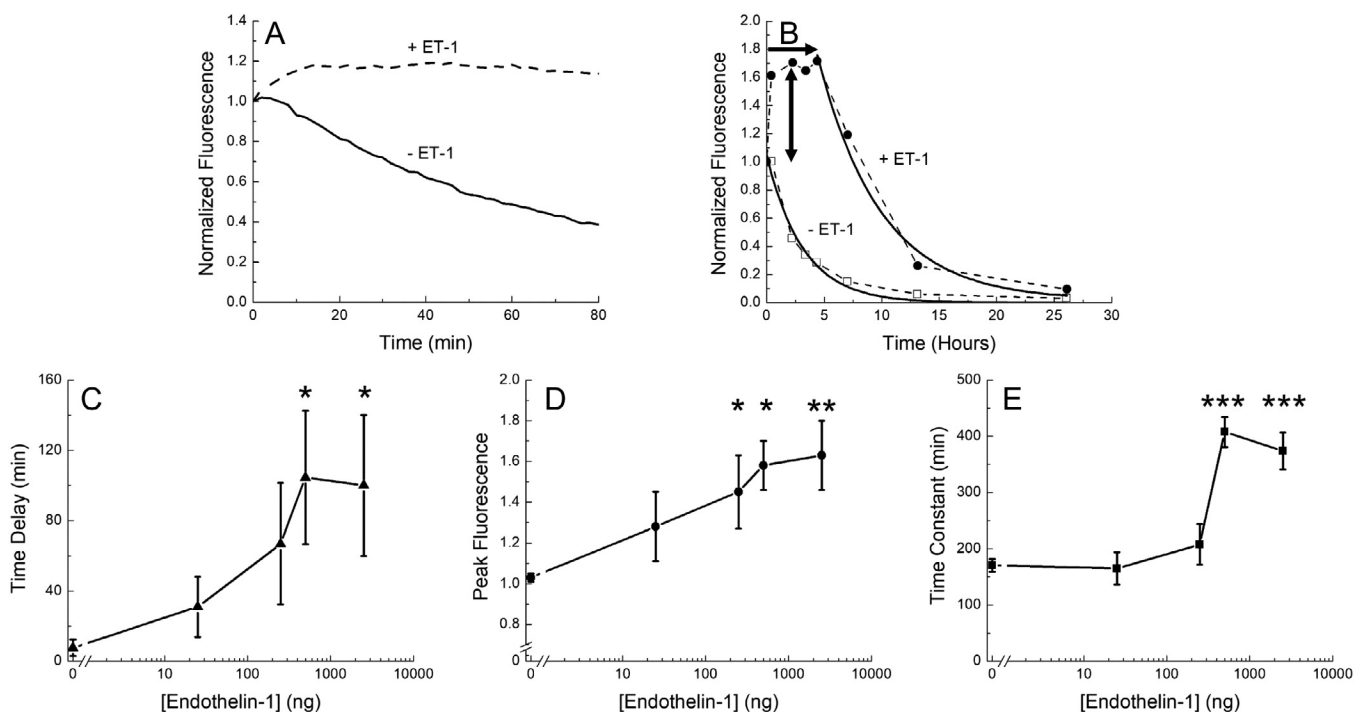


Fig. 5. Endothelin-1 dose-dependently inhibited the clearance of 2 kDa PEG-NIR from rat knees. A: Anesthetized rats were injected with 50 μ L of 100 μ M 2 kDa PEG-NIR in the presence (dashed line) or absence (solid line) of 2.5 μ g ET-1. Fluorescence images were taken every 2 min and the rats were kept under anesthesia throughout the 80 min of data collection. B: Anesthetized rats were injected with 50 μ L of 100 μ M 2 kDa PEG-NIR in the presence (solid circles; 1 representative study from the 6 animals) or absence (open squares; 1 representative study from the 10 animals) of 2.5 μ g ET-1. Fluorescence images were taken at each time point and rats recovered from anesthesia in between the time points. Solid lines were mono-exponential fits for the clearance of PEG-NIR. Horizontal arrow (single arrow head) reflected the measured time delay and the vertical arrow (double arrow head) reflected the fold difference in fluorescence. The effect of ET-1 on the time delay (C), peak normalized fluorescence (D) and calculated time constant (E) were shown. The number of samples for 0, 25, 250, 500 and 2500 ng ET-1 with 2 kDa PEG-NIR were 10, 6, 6, 4 and 6, respectively. Significance was determined after performing one-way ANOVA and post ad hoc Tukey analysis with calculated *p* values to be ≤ 0.05 (*), ≤ 0.01 (**) or ≤ 0.001 (***).

injections into rat knees. Recently, a study reported joint clearance and synovial transport of different sized dextran (10 and 500 kDa) in naïve and OA rats; clearance and synovial transport was slower for larger size dextran and overall, its transport was impaired in OA [40]. These findings are consistent with the size-based clearance that we and others have found. A separate study by Loffredo et al. [45] used heparin, a charged molecule, to retain insulin growth factors within the knee joint for longer period. Similarly, Bajpayee et al. [16] have shown that charged avidin conjugated to Texas Red is sequestered in articular cartilage and meniscus for days while neutral avidin is cleared within 24 h. Further, the charge moieties were correlated to glycosaminoglycan content of various cartilage tissues within the knee joints. The latter two studies injected similar sized conjugates as 40 kDa PEG-NIR but the materials had charged moieties which prevented free diffusion and clearance within the knee joint. These studies together suggest that both size and charge play a critical role in the retention of materials within the joint and can be utilized to improve biomaterial carrier design and retention of drugs within the knee joint.

For treatment of joint diseases, intra-articular injections are becoming a common minimally invasive approach to deliver various therapeutic ranging from small molecules, to cells, to tissue derivatives. Various formulations of PEG based biomaterials [46–48] have been used as drug carriers to improve drug retention and to increase drug concentration within a localized area. For example, Nemirovskiy et al. [49] demonstrated that recombinant human growth hormone (rhGH) conjugated to PEG is retained in rat OA knee joints longer than free rhGH after intra-articular injection. Presumably, the increased retention of rhGH-PEG caused a prolonged production of insulin-like growth factor-1 within the

synovium. Further, rhGH-PEG had a longer serum half-life than rhGH suggesting that PEG may hamper its clearance from circulation. Sterner et al. [50] have shown that PEG size can influence permeability and clearance through synovial membranes. Even PEG hydrogel microspheres have been used to deliver compounds associated with inflammation and were found to be retained for at least a month [47]. These data suggest that increasing the size of the PEG into the micron range would further influence the clearance kinetics; typically, in peripheral tissues, this size range changes clearance mechanisms from passive, diffusion dominated clearance process to an active, cell mediated clearance process. PEG based delivery provides a platform that can be tailored to many different therapeutics and as we show here, the retention within the joint space and the subsequent clearance route can be controlled through simple size dependent mechanisms.

The optimal hydrodynamic diameter range for uptake into lymphatics is 10–100 nm and anything <10 nm is readily reabsorbed by blood capillaries [51–54]. Our finding herein is consistent with this dogma for clearance of nanosized materials into lymph nodes. The 40 kDa PEG-NIR with hydrodynamic diameter greater than 10 nm was found collected in the lymph node while 2 kDa PEG-NIR (<10 nm) was not present in the node. These data suggest that 40 kDa PEG-NIR is cleared by the expected pathways through the lymphatic system, as has been demonstrated to occur for skin [55]. Increased fluorescence was also found in the bladder when rats were injected with 2 kDa or 40 kDa PEG-NIR suggesting that these conjugates may readily pass through glomeruli and collect in urine [2]. Interestingly, a significantly higher amount of fluorescence was found from bladders of 40 kDa PEG-NIR injected animals than of 2 kDa PEG-NIR injected animals. This may be due to a

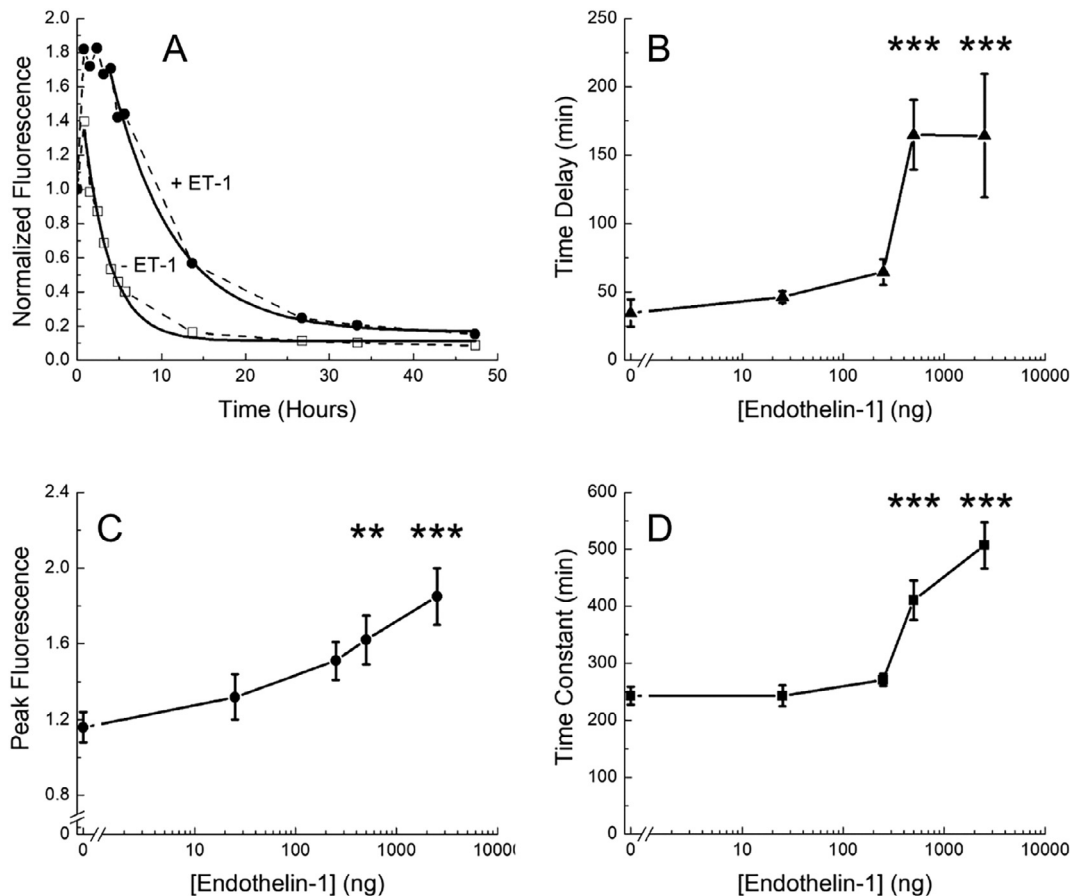


Fig. 6. Endothelin-1 dose-dependently inhibited the clearance of 40 kDa PEG-NIR from rat knees. A: Anaesthetized rats were injected intra-articularly with 50 μ L of 100 μ M 40 kDa PEG-NIR in the presence (solid circles; 1 representative trace from the 6 animals) or absence (open squares; 1 representative trace from the 11 animals) of 2.5 μ g ET-1. Fluorescence images of the knee were taken at each time point and rats recovered from anesthesia in between the time points. Solid lines represented mono-exponential fits for the clearance of PEG-NIR. The effect of ET-1 on the time delay (B), peak normalized fluorescence (C) and calculated time constant (D) were shown. The sample size for 0, 25, 250, 500 and 2500 ng ET-1 with 40 kDa PEG-NIR were 11, 6, 6, 7 and 6, respectively. Significance was determined after performing one-way ANOVA and post ad hoc Tukey analysis with calculated p values <0.01 (**) or 0.001 (***).

higher amount of 2 kDa PEG-NIR being excreted from the animal, which we did not account for in this study. We also found free dye in urine of animals injected with 40 kDa NIR-PEG; however, we cannot be sure if the free dye was from the unpurified reagent used or PEG-NIR that were metabolized by the animal. Regardless, we did not find any free dye or fragmented 40 kDa PEG-NIR in lymph node tissues, suggesting that only intact 40 kDa PEG-NIR was collected by lymphatics.

The role of ET-1 in joint homeostasis is largely unclear. ET-1 levels have been reported to be elevated in the synovial fluid of OA patients [27] and further, the concentration of ET-1 in the synovial fluid is directly correlated to severity and stage of OA disease progression [29]. ET-1 has also been implicated in other bone related diseases, including rheumatoid arthritis and scleroderma, and abnormalities, such as development of craniofacial mandible [36]. These reports have led to investigations targeting ET-1 signaling as a potential therapeutic in arthritis development and progression. In an OA rat model, ET-1 antagonist BQ-123 (30 nmol via weekly intra-articular injection) was shown to attenuate the progression of OA [56,57]. Donate et al. [58] reported that oral administration of bosentan protected collagen-induced OA in rats. These antagonists are thought to prevent the breakdown of articular cartilage in OA since ET-1 is upregulated in chondrocytes during OA and can increase the activity of MMP's.

Our investigation herein provides an alternative role for ET-1 in joint homeostasis by regulating microcirculation and clearance pathways of the joint. We demonstrated that intra-articular injection of ET-1 into rat knees dose-dependently and time-dependently inhibited the clearance of both 2 kDa and 40 kDa PEG-NIR, suggesting a modulation of both venous and lymphatic systems. Thus, it is probable that ET-1 has a general effect on the microenvironment of the knee and not specific to blood or lymphatic pathways. Lymph formation itself is a function of the Starlings forces that drive capillary filtration. Thus, any factor that alters local arterial and/or venous pressure will likely alter lymph formation and thus lymphatic clearance. The data is unclear to what extent the observed changes in clearance of the two different sized molecules is a result of arterial effects, venous effects, lymphatic effects, or some combination. Thus, the alterations in the local microcirculation by ET-1 has the consequence of reducing the clearance of both large and small molecules from the joint. Consistent with others [24,59], ET-1 can modulate isolated venous and lymphatic vessels. In addition, the effect of ET-1 is observed within minutes of intra-articular injection, suggesting that ET-1 action is within the localized knee joint. From this finding, we speculate that ET-1 may prevent clearance of inflammatory cytokines during OA and hence, antagonists of ET-1 would improve knee clearance and thus decrease OA progression. Similarly, Karlsen

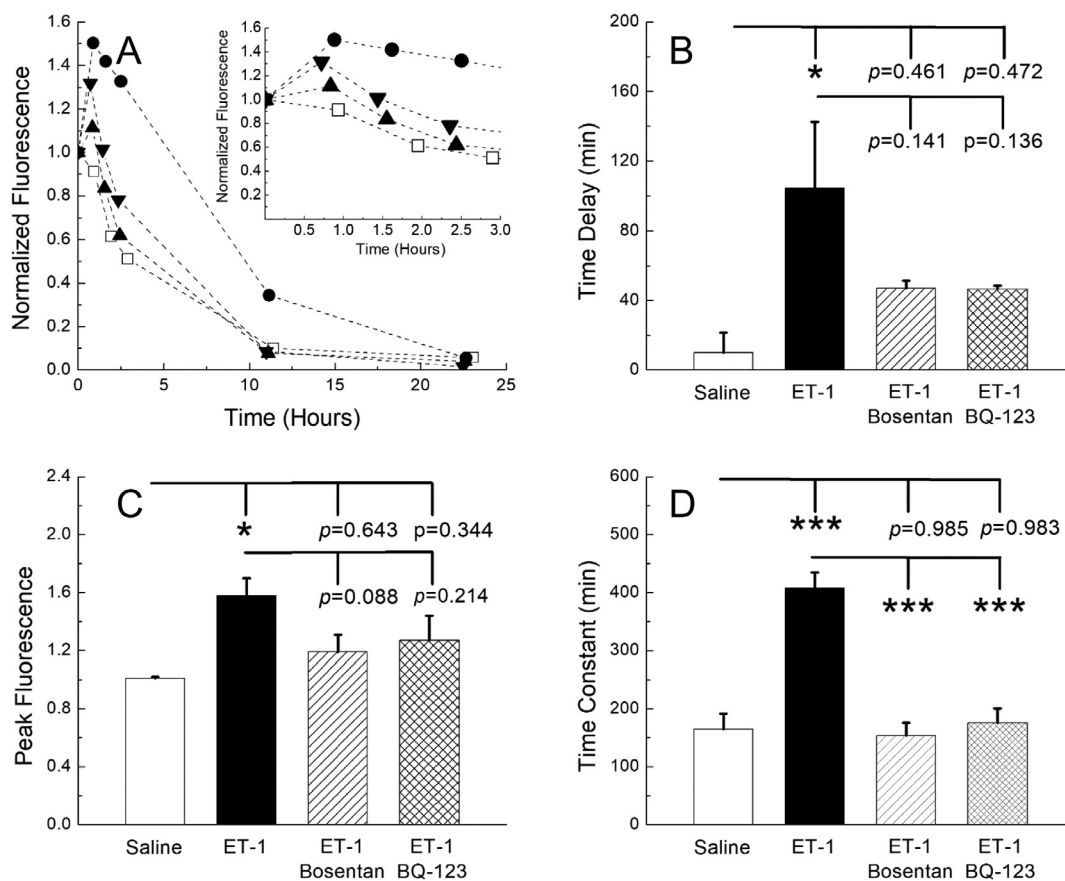


Fig. 7. Bosentan and BQ-123 attenuated the effects of ET-1 inhibition of 2 kDa PEG-NIR clearance. **A:** Data points illustrated the time-dependent clearance of 2 kDa PEG-NIR without (open squares; 1 representative trace from the 4 animals) or with ET-1 (filled circles; 1 representative trace from the 4 animals), with ET-1 and bosentan (solid, upright triangle; 1 representative trace from the 4 animals) and with ET-1 and BQ-123 (solid, inverted triangle; 1 representative trace from the 4 animals). 500 ng ET-1 (0.2 nmol) were challenged with 25 μ g bosentan (43.9 nmol) or 5 μ g BQ-123 (8.2 nmol). *Inset*, the effect of ET-1 antagonists on the clearance of 2 kDa PEG-NIR with a reduced time scale (up to 3 h). The effect of bosentan and BQ-123 on the ET-1 induced changes to time delay (**B**), peak normalized fluorescence (**C**) and calculated time constant (**D**) were shown. For saline, ET-1, ET-1 with bosentan, and ET-1 with BQ-123, n's equaled 4 for each condition. Significance was determined after performing one-way ANOVA and post ad hoc Tukey analysis. Calculated values were considered significant when $p < 0.05$ (*) or 0.001 (***) or were not significant when $p \geq 0.05$.

et al. [60] have also shown that ET-1 can delay clearance of lymphatic drainage from intradermal injection in mice and rat. The transient effect of ET-1 may be explained by its rapid clearance from the knee space since it is relatively smaller than 2 kDa PEG. Other factors that may contribute to the transient nature of ET-1 activity is ET receptor internalization and desensitization [61,62]. In addition, isoflurane may influence ET-1 effectiveness in rat knee joints. We found a decreased response to ET-1 when animals were continuously kept under isoflurane anesthesia. Others have also reported similar findings where isoflurane can attenuate ET-1 effects on aortic contractions [63], airways of rat smooth muscle contraction [64] and calcium mobilization of cultured smooth muscle cells [65].

There are numerous small molecule inhibitors of ET-1 that are FDA approved agents used for the treatment of hypertension. Bosentan, a synthetic small molecule, and BQ-123, a cyclic peptide, are competitive blockers of ET-1 for its receptors. Similar to established pharmacodynamic profile for these antagonists, we found that bosentan [66,67] was less efficacious than BQ-123 [68,69] and hence, a 5.4-fold more molar amount of bosentan was needed to achieve a similar block of ET-1 induced effects as BQ-123. It is noteworthy that inhibition of ET-1 with bosentan (oral administration) was shown to ameliorate pain, inflammation and severity of arthritis-induced cartilage deterioration in a rodent arthritis model

[58]. Taken together with our current finding, these data suggest that bosentan may improve clearance mechanisms in arthritic knees; improved clearance could regulate joint homeostasis and prevent the accumulation of inflammatory cytokines, proteases, and other mediators of disease progression. Consistent with our speculation, Guo et al. [70] have shown that inhibition of lymphatic drainage can exacerbate chronic arthritis.

5. Conclusion

Herein, we demonstrated that NIR imaging technology can be used to assess clearance of PEG-NIR conjugates from the knee joint space. We showed that size-based clearance pathways in the joint abide by similar principles to other peripheral tissues where materials larger than 10 nm diameter clear through the lymphatic system. Additionally, we showed that ET-1 can regulate joint clearance suggesting a potential role in joint disease. NIR imaging technologies may have potential utilization in diagnostic applications to determine disease state and progression, especially for arthritis. Already ICG is an NIR dye that is FDA-approved and is used in the clinic to visualize vessels in certain tissue beds. Furthermore, therapies that target lymphatic function and the micro-circulation of joints may be a promising avenue for therapeutic development.

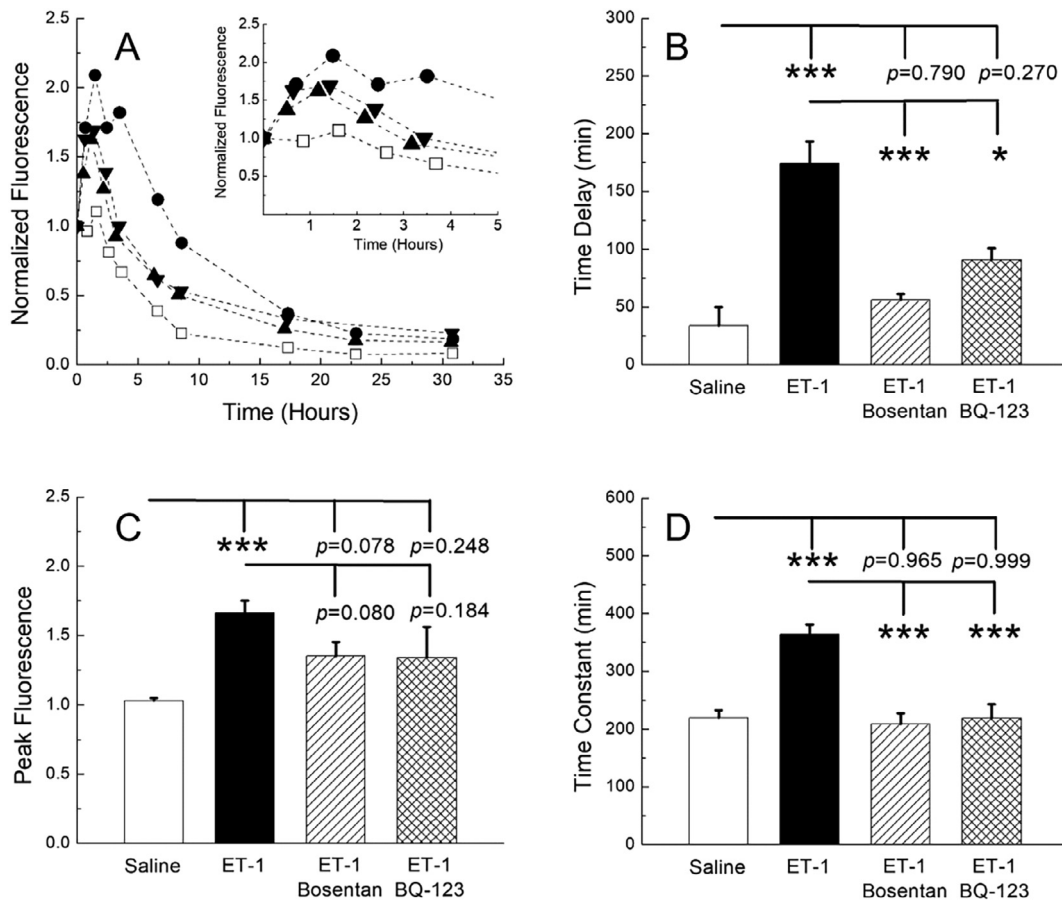


Fig. 8. Bosentan and BQ-123 attenuated the effects of ET-1 inhibition of 40 kDa PEG-NIR clearance. A: Data points illustrated the time-dependent clearance of 40 kDa PEG-NIR without (open squares; 1 representative trace from the 8 animals) or with ET-1 (filled circles; 1 representative trace from the 11 animals), with ET-1 and bosentan (solid, upright triangle; 1 representative trace from the 6 animals) and with ET-1 and BQ-123 (solid, inverted triangle; 1 representative trace from the 3 animals). 500 ng ET-1 (0.2 nmol) were challenged with 25 μ g bosentan (43.9 nmol) or 5 μ g BQ-123 (8.2 nmol). *Inset*, the effect of ET-1 antagonists on the clearance of 2 kDa PEG-NIR with a reduced time scale (up to 5 h). The effect of bosentan and BQ-123 on the ET-1 induced changes to time delay (B), peak normalized fluorescence (C) and calculated time constant (D) were shown. For saline, ET-1, ET-1 with bosentan, and ET-1 with BQ-123, n's equaled 8, 11, 6 and 3, respectively. Significance was determined after performing one-way ANOVA and post ad hoc Tukey analysis. Calculated values were considered significant when $p < 0.05$ (*) or 0.001 (***) or were not significant when $p \geq 0.05$.

Acknowledgments

The authors would like to thank Joseph C. Shaver for his technical assistance towards synthesis of the PEG-NIR reagents.

Funding

This work was supported by the National Center for Advancing Translation Science of the National Institutes of Health [grant number UL1TR000454]; the National Institute of Biomedical Imaging and Bioengineering of the National Institutes of Health [grant number 5T32EB006343]; the Department of Defense PRMRP Grant [grant number PR171379].

Disclosures

No conflict of interest and thus, nothing to disclose.

Appendix A. Supplementary data

Supplementary data to this article can be found online at <https://doi.org/10.1016/j.actbio.2019.04.025>.

References

- [1] J.R. Levick, Contributions of the lymphatic and microvascular systems to fluid absorption from the synovial cavity of the rabbit knee, *J. Physiol.* 306 (1980) 445–461.
- [2] H. Sarin, Physiologic upper limits of pore size of different blood capillary types and another perspective on the dual pore theory of microvascular permeability, *J. Angiogenesis Res.* 2 (2010) 14.
- [3] P.A. Simkin, J.E. Bassett, Pathways of microvascular permeability in the synovium of normal and diseased human knees, *J. Rheumatol.* 38 (12) (2011) 2635–2642.
- [4] D.L. Brown, A.G. Cooper, R. Bluestone, Exchange of IgM and albumin between plasma and synovial fluid in rheumatoid arthritis, *Ann. Rheum. Dis.* 28 (6) (1969) 644–651.
- [5] G.P. Rodnan, M.J. MacLachlan, The absorption of serum albumin and gamma globulin from the knee joint of man and rabbit, *Arthritis Rheum.* 3 (1960) 152–157.
- [6] A.J. Sliwinski, N.J. Zvaifler, The removal of aggregated and nonaggregated autologous gamma globulin from rheumatoid joints, *Arthritis Rheum.* 12 (5) (1969) 504–514.
- [7] W.J. Wallis, P.A. Simkin, W.B. Nelp, Protein traffic in human synovial effusions, *Arthritis Rheum.* 30 (1) (1987) 57–63.
- [8] P.A. Simkin, The human knee: A window on the microvasculature, *Tissue Barriers* 3 (1–2) (2015) e970465.
- [9] D.A. Walsh, P. Verghese, G.J. Cook, D.F. McWilliams, P.I. Mapp, S. Ashraf, D. Wilson, Lymphatic vessels in osteoarthritic human knees, *Osteoarthritis Cartilage* 20 (5) (2012) 405–412.
- [10] J. Shi, Q. Liang, M. Zuscik, J. Shen, D. Chen, H. Xu, Y.J. Wang, Y. Chen, R.W. Wood, J. Li, B.F. Boyce, L. Xing, Distribution and alteration of lymphatic vessels in knee joints of normal and osteoarthritic mice, *Arthritis Rheumatol.* 66 (3) (2014) 657–666.

- [11] W. Wang, X. Lin, H. Xu, W. Sun, E.M. Bouta, M.J. Zuscik, D. Chen, E.M. Schwarz, L. Xing, Bortezomib attenuates joint tissue damage in a mouse model of experimental post-traumatic osteoarthritis, which is associated with improved synovial lymphatic function, *Arthritis Rheumatol* (2018).
- [12] M. Albuquerque, J.P. de Lima, Articular lymphoscintigraphy in human knees using radiolabeled dextran, *Lymphology* 23 (4) (1990) 215–218.
- [13] P.A. Simkin, Assessing biomarkers in synovial fluid: consider the kinetics of clearance, *Osteoarthritis Cartilage* 21 (1) (2013) 7–9.
- [14] N.E. Larsen, H.D. Dursema, C.T. Pollak, E.M. Skrabut, Clearance kinetics of a hyalan-based viscosupplement after intra-articular and intravenous administration in animal models, *J. Biomed. Mater. Res. B Appl. Biomater.* 100 (2) (2012) 457–462.
- [15] W.J. Wallis, P.A. Simkin, W.B. Nelp, D.M. Foster, Intraarticular volume and clearance in human synovial effusions, *Arthritis Rheum.* 28 (4) (1985) 441–449.
- [16] A.G. Bajpayee, M. Scheu, A.J. Grodzinsky, R.M. Porter, Electrostatic interactions enable rapid penetration, enhanced uptake and retention of intra-articular injected avidin in rat knee joints, *J. Orthop. Res.* 32 (8) (2014) 1044–1051.
- [17] R. Sharma, W. Wang, J.C. Rasmussen, A. Joshi, J.P. Houston, K.E. Adams, A. Cameron, S. Ke, S. Kwon, M.E. Mawad, E.M. Sevick-Muraca, Quantitative imaging of lymph function, *Am. J. Physiol. Heart Circ. Physiol.* 292 (6) (2007) H3109–H3118.
- [18] L.L. Gompels, N.H. Lim, T. Vincent, E.M. Paleolog, In vivo optical imaging in arthritis—an enlightening future?, *Rheumatology (Oxford)* 49 (8) (2010) 1436–1446.
- [19] M. Weiler, T. Kassis, B. Dixon, Sensitivity analysis of near infrared functional lymphatic imaging, *J. Biomed. Optics* 17 (6) (2012) 1–11. 066019.
- [20] E.M. Sevick-Muraca, S. Kwon, J.C. Rasmussen, Emerging lymphatic imaging technologies for mouse and man, *J. Clin. Invest.* 124 (3) (2014) 905–914.
- [21] M. Weiler, B. Dixon, Differential transport function of lymphatic vessels in the rat tail model and the long-term effects of Indocyanine Green as assessed with near-infrared imaging, *Front. Physiol.* 4 (2013) 1–10.
- [22] T.S. Nelson, R.E. Akin, M.J. Weiler, T. Kassis, J.A. Kornuta, J. Brandon Dixon, Minimally invasive method for determining the effective lymphatic pumping pressure in rats using near-infrared imaging, *Am. J. Physiol. Regul. Integr. Comp. Physiol.* 306 (5) (2014) R281–R290.
- [23] N. Telinius, N. Drewsen, H. Pilegaard, H. Kold-Petersen, M. de Leval, C. Aalkjaer, V. Hjortdal, D.B. Boedtker, Human thoracic duct in vitro: diameter-tension properties, spontaneous and evoked contractile activity, *Am. J. Physiol. Heart Circ. Physiol.* 299 (3) (2010) H811–H818.
- [24] Z.B. Fortes, R. Scivoletto, J. Garcia-Leme, Endothelin-1 induces potent constriction of lymphatic vessels in situ, *Eur. J. Pharmacol.* 170 (1–2) (1989) 69–73.
- [25] F. Spinella, V. Caprara, E. Garrafa, V. Di Castro, L. Rosano, P.G. Natali, A. Bagnato, Endothelin axis induces metalloproteinase activation and invasiveness in human lymphatic endothelial cells, *Can. J. Physiol. Pharmacol.* 88 (8) (2010) 782–787.
- [26] A.M. Nahir, A. Hoffman, M. Lorber, H.R. Keiser, Presence of immunoreactive endothelin in synovial fluid: analysis of 22 cases, *J. Rheumatol.* 18 (5) (1991) 678–680.
- [27] N. Miyasaka, Y. Hirata, K. Ando, K. Sato, H. Morita, M. Shichiri, K. Kanno, K. Tomita, F. Marumo, Increased production of endothelin-1 in patients with inflammatory arthritides, *Arthritis Rheum.* 35 (4) (1992) 397–400.
- [28] J. Wharton, R.A. Rutherford, D.A. Walsh, P.I. Mapp, G.A. Knock, D.R. Blake, J.M. Polak, Autoradiographic localization and analysis of endothelin-1 binding sites in human synovial tissue, *Arthritis Rheum.* 35 (8) (1992) 894–899.
- [29] Z. Zhao, E. Li, Q. Cao, J. Sun, B. Ma, Endothelin-1 concentrations are correlated with the severity of knee osteoarthritis, *J. Invest. Med.* 64 (4) (2016) 872–874.
- [30] H. Yoshida, M. Ohhara, K. Ohsumi, Production of endothelin-1 by cultured human synoviocytes, *Clin. Chim. Acta* 259 (1–2) (1997) 187–189.
- [31] H. Messai, A.M. Khatib, G. Lebrun, P. Aubin, M. Florina, F. Jean, D.R. Mitrovic, Endothelin-1 in monolayer cultures of articular chondrocytes from young and old rats: regulation by growth factors and cytokines, *Mech. Ageing Dev.* 114 (1) (2000) 37–48.
- [32] H. Messai, A. Panasyuk, A. Khatib, A. Barbara, D.R. Mitrovic, Endothelin-1 receptors on cultured rat articular chondrocytes: regulation by age, growth factors, and cytokines, and effect on cAMP production, *Mech. Ageing Dev.* 122 (6) (2001) 519–531.
- [33] Z. Barrett-O'Keefe, S.J. Ives, J.D. Trinity, G. Morgan, M.J. Rossman, A.J. Donato, S. Runnels, D.E. Morgan, B.S. Gmelch, A.D. Bledsoe, R.S. Richardson, D.W. Wray, Endothelin-A-mediated vasoconstriction during exercise with advancing age, *J. Gerontol. A Biol. Sci. Med. Sci.* 70 (5) (2015) 554–565.
- [34] S.E. Andersson, K. Lexmuller, K. Alving, G.M. Ekstrom, Periarticular tissue levels of cytokine- and endothelin-1-like immunoreactivity during the course of antigen-induced arthritis in the rat, *Inflamm. Res.* 48 (9) (1999) 491–496.
- [35] M. Roy-Beaudry, J. Martel-Pelletier, J.P. Pelletier, K.N. M'Barek, S. Christgau, F. Shipkolye, F. Moldovan, Endothelin-1 promotes osteoarthritic cartilage degradation via matrix metalloproteinase 1 and matrix metalloproteinase 13 induction, *Arthritis Rheum.* 48 (10) (2003) 2855–2864.
- [36] A. Sin, W. Tang, C.Y. Wen, S.K. Chung, K.Y. Chiu, The emerging role of endothelin-1 in the pathogenesis of subchondral bone disturbance and osteoarthritis, *Osteoarthritis Cartilage* 23 (4) (2015) 516–524.
- [37] M.S. Razavi, T.S. Nelson, Z. Nepiyushchikh, R.L. Gleason, J.B. Dixon, The relationship between lymphangion chain length and maximum pressure generation established through in vivo imaging and computational modeling, *Am. J. Physiol. Heart Circ. Physiol.* 313 (6) (2017) H1249–H1260.
- [38] H. Suami, D.W. Chang, K. Matsumoto, Y. Kimata, Demonstrating the lymphatic system in rats with microinjection, *Anat. Rec. (Hoboken)* 294 (9) (2011) 1566–1573.
- [39] A. Singh, R. Agarwal, C.A. Diaz-Ruiz, N.J. Willett, P. Wang, L.A. Lee, Q. Wang, R.E. Guldberg, A.J. Garcia, Nanoengineered particles for enhanced intra-articular retention and delivery of proteins, *Adv. Healthc. Mater.* 3 (10) (2014). 1562–7, 1525.
- [40] T.K. Mwangi, I.M. Berke, E.H. Nieves, R.D. Bell, S.B. Adams, L.A. Setton, Intra-articular clearance of labeled dextrans from naive and arthritic rat knee joints, *J. Control. Release* 283 (2018) 76–83.
- [41] J. Li, T.D. Stewart, Z. Jin, R.K. Wilcox, J. Fisher, The influence of size, clearance, cartilage properties, thickness and hemiarthroplasty on the contact mechanics of the hip joint with biphasic layers, *J. Biomech.* 46 (10) (2013) 1641–1647.
- [42] T. Thote, A.S. Lin, Y. Raji, S. Moran, H.Y. Stevens, M. Hart, R. Kamath, R.E. Guldberg, N.J. Willett, Localized 3D analysis of cartilage composition and morphology in small animal models of joint degeneration, *Osteoarthritis Cartilage* (2013).
- [43] N. Willett, T. Thote, A. Lin, S. Moran, Y. Raji, S. Sridaran, H. Stevens, R. Guldberg, Intra-articular injection of micronized dehydrated human amnion/chorion membrane attenuates osteoarthritis development, *Arthritis Res. Therapy* 16 (1) (2014) R47.
- [44] R.C. Stewart, P.N. Bansal, V. Entezari, H. Lusic, R.M. Nazarian, B.D. Snyder, M.W. Grinstaff, Contrast-enhanced CT with a high-affinity cationic contrast agent for imaging ex vivo bovine, intact ex vivo rabbit, and in vivo rabbit cartilage, *Radiology* 266 (1) (2013) 141–150.
- [45] F.S. Loffredo, J.R. Pancoast, L. Cai, T. Vannelli, J.Z. Dong, R.T. Lee, P. Patwari, Targeted delivery to cartilage is critical for in vivo efficacy of insulin-like growth factor 1 in a rat model of osteoarthritis, *Arthritis Rheumatol.* 66 (5) (2014) 1247–1255.
- [46] P. Puebla, P. Pastoriza, E. Barcia, A. Fernandez-Carballido, PEG-derivative effectively modifies the characteristics of indomethacin-PLGA microspheres destined to intra-articular administration, *J. Microencapsul.* 22 (7) (2005) 793–808.
- [47] L. Bedouet, F. Pascale, L. Moine, M. Wassef, S.H. Ghegediban, V.N. Nguyen, M. Bonneau, D. Labarre, A. Laurent, Intra-articular fate of degradable poly (ethylene glycol)-hydrogel microspheres as carriers for sustained drug delivery, *Int. J. Pharm.* 456 (2) (2013) 536–544.
- [48] R. Somack, M.G. Saifer, L.D. Williams, Preparation of long-acting superoxide dismutase using high molecular weight polyethylene glycol (41,000–72,000 daltons), *Free Radic. Res. Commun.* 12–13 (Pt 2) (1991) 553–562.
- [49] O. Nemirovskiy, Y.J. Zheng, D. Tung, B. Korniski, S. Settle, A. Skepner, M. Yates, P. Aggarwal, T. Sunyer, D.J. Aguiar, Pharmacokinetic/pharmacodynamic (PK/PD) differentiation of native and PEGylated recombinant human growth hormone (rhGH and PEG-rhGH) in the rat model of osteoarthritis, *Xenobiotica* 40 (8) (2010) 586–592.
- [50] B. Sterner, M. Harms, S. Woll, M. Weigandt, M. Windbergs, C.M. Lehr, The effect of polymer size and charge of molecules on permeation through synovial membrane and accumulation in hyaline articular cartilage, *Eur. J. Pharm. Biopharm.* 101 (2016) 126–136.
- [51] T.R. Bagby, S. Cai, S. Duan, S. Thati, D.J. Aires, L. Forrest, Impact of molecular weight on lymphatic drainage of a biopolymer-based imaging agent, *Pharmaceutics* 4 (2) (2012) 276–295.
- [52] S.K. Nune, P. Gunda, B.K. Majeti, P.K. Thallapally, M.L. Forrest, Advances in lymphatic imaging and drug delivery, *Adv. Drug Deliv. Rev.* 63 (10–11) (2011) 876–885.
- [53] S.T. Reddy, A.J. van der Vlies, E. Simeoni, V. Angeli, G.J. Randolph, C.P. O'Neil, L. K. Lee, M.A. Swartz, J.A. Hubbell, Exploiting lymphatic transport and complement activation in nanoparticle vaccines, *Nat. Biotechnol.* 25 (10) (2007) 1159–1164.
- [54] S.N. Thomas, A. Schudel, Overcoming transport barriers for interstitial-, lymphatic-, and lymph node-targeted drug delivery, *Curr. Opin. Chem. Eng.* 7 (2015) 65–74.
- [55] S.T. Proulx, P. Luciani, S. Derzsi, M. Rinderknecht, V. Mumprecht, J.C. Leroux, M. Detmar, Quantitative imaging of lymphatic function with liposomal indocyanine green, *Cancer Res.* 70 (18) (2010) 7053–7062.
- [56] G.N. Kaufman, C. Zauter, B. Valteau, P. Sirois, F. Moldovan, Nociceptive tolerance is improved by bradykinin receptor B1 antagonism and joint morphology is protected by both endothelin type A and bradykinin receptor B1 antagonism in a surgical model of osteoarthritis, *Arthritis Res. Ther.* 13 (3) (2011) R76.
- [57] T.D. Warner, P. Klemm, What turns on the endothelins?, *Inflamm. Res.* 45 (2) (1996) 51–53.
- [58] P.B. Donate, T.M. Cunha, W.A. Verri Jr., C.M. Junta, F.O. Lima, S.M. Vieira, R.S. Peres, K.F. Bombonato-Prado, P. Louzada Jr., S.H. Ferreira, E.A. Donadi, G.A. Passos, F.Q. Cunha, Bosentan, an endothelin receptor antagonist, ameliorates collagen-induced arthritis: the role of TNF- α in the induction of endothelin system genes, *Inflamm. Res.* 61 (4) (2012) 337–348.
- [59] D.E. Dobbins, J.M. Dabney, Endothelin-mediated constriction of prenatal lymphatic vessels in the canine forelimb, *Regul. Pept.* 35 (1) (1991) 81–91.
- [60] T.V. Karlsen, E. McCormack, M. Mujic, O. Tenstad, H. Wiig, Minimally invasive quantification of lymph flow in mice and rats by imaging depot clearance of near-infrared albumin, *Am. J. Physiol. Heart Circ. Physiol.* 302 (2) (2012) H391–H401.
- [61] T. Bremnes, J.D. Paasche, A. Mehlum, C. Sandberg, B. Bremnes, H. Attramadal, Regulation and intracellular trafficking pathways of the endothelin receptors, *J. Biol. Chem.* 275 (23) (2000) 17596–17604.

- [62] F. Gartner, T. Seidel, U. Schulz, J. Gummert, H. Milting, Desensitization and internalization of endothelin receptor A: impact of G protein-coupled receptor kinase 2 (GRK2)-mediated phosphorylation, *J. Biol. Chem.* 288 (45) (2013) 32138–32148.
- [63] A. Boillot, B. Vallet, J. Marty, A. Auclerc, F. Barale, Effects of halothane, enflurane and isoflurane on contraction of rat aorta induced by endothelin-1, *Br. J. Anaesth.* 75 (6) (1995) 761–767.
- [64] S. Akhtar, S.J. Brull, Effect of isoflurane on endothelin-1 mediated airway smooth muscle contraction, *Pulm. Pharmacol. Ther.* 11 (2–3) (1998) 227–230.
- [65] P.A. Iaizzo, The effects of halothane and isoflurane on intracellular Ca²⁺ regulation in cultured cells with characteristics of vascular smooth muscle, *Cell Calcium* 13 (8) (1992) 513–520.
- [66] M. Clozel, V. Breu, G.A. Gray, B. Kalina, B.M. Loffler, K. Burri, J.M. Cassal, G. Hirth, M. Muller, W. Neidhart, et al., Pharmacological characterization of bosentan, a new potent orally active nonpeptide endothelin receptor antagonist, *J. Pharmacol. Exp. Ther.* 270 (1) (1994) 228–235.
- [67] J.J. Maguire, R.E. Kuc, A.P. Davenport, Defining the affinity and receptor subtype selectivity of four classes of endothelin antagonists in clinically relevant human cardiovascular tissues, *Life Sci.* 91 (13–14) (2012) 681–686.
- [68] M.G. Peter, A.P. Davenport, Characterization of the endothelin receptor selective agonist, BQ3020 and antagonists BQ123, FR139317, BQ788, 50235, Ro462005 and bosentan in the heart, *Br. J. Pharmacol.* 117 (3) (1996) 455–462.
- [69] J.J. Maguire, R.E. Kuc, B.A. Rous, A.P. Davenport, Failure of BQ123, a more potent antagonist of sarafotoxin 6b than of endothelin-1, to distinguish between these agonists in binding experiments, *Br. J. Pharmacol.* 118 (2) (1996) 335–342.
- [70] R. Guo, Q. Zhou, S.T. Proulx, R. Wood, R.C. Ji, C.T. Ritchlin, B. Pytowski, Z. Zhu, Y. J. Wang, E.M. Schwarz, L. Xing, Inhibition of lymphangiogenesis and lymphatic drainage via vascular endothelial growth factor receptor 3 blockade increases the severity of inflammation in a mouse model of chronic inflammatory arthritis, *Arthritis Rheum.* 60 (9) (2009) 2666–2676.

THERAPEUTIC EFFICACY OF INTRA-ARTICULAR DELIVERY OF ENCAPSULATED HUMAN MESENCHYMAL STEM CELLS ON EARLY STAGE OSTEOARTHRITIS

J.M. McKinney^{1,2,4}, T.N. Doan^{1,2}, L. Wang³, J.N. Deppen^{3,4}, D.S. Reece^{4,5}, K.A. Pucha², S.C. Ginn³, R.D. Levitt³ and N.J. Willett^{1,2,4,5,*}

¹Research Service, VA Medical Center, Decatur, GA, USA

²Department of Orthopedics, Emory University, Atlanta, GA, USA

³Department of Medicine, Division of Cardiology, Emory University, Atlanta, GA, USA

⁴Wallace H. Coulter Department of Biomedical Engineering, Georgia Institute of Technology and Emory University, Atlanta, GA, USA

⁵Parker H. Petit Institute for Bioengineering and Bioscience, Georgia Institute of Technology, Atlanta, GA, USA

Abstract

Mesenchymal stem cells (MSCs) represent a great therapeutic promise in pre-clinical models of osteoarthritis (OA), but many questions remain as to their therapeutic mechanism of action: engraftment *versus* paracrine action. Encapsulation of human MSCs (hMSCs) in sodium alginate microspheres allowed for the paracrine signaling properties of these cells to be isolated and studied independently of direct cellular engraftment. The objective of the present study was to quantitatively assess the efficacy of encapsulated hMSCs as a disease-modifying therapeutic for OA, using a medial meniscal tear (MMT) rat model. It was hypothesized that encapsulated hMSCs would have a therapeutic effect, through paracrine-mediated action, on early OA development.

Lewis rats underwent MMT surgery to induce OA. 1 d post-surgery, rats received intra-articular injections of encapsulated hMSCs or controls (*i.e.*, saline, empty capsules, non-encapsulated hMSCs). Microstructural changes in the knee joint were quantified using equilibrium partitioning of an ionic contrast agent based micro-computed tomography (EPIC- μ CT) at 3 weeks post-surgery, an established time point for early OA.

Encapsulated hMSCs significantly attenuated MMT-induced increases in articular cartilage swelling and surface roughness and augmented cartilaginous and mineralized osteophyte volumes.

Cellular encapsulation allowed to isolate the hMSC paracrine signaling effects and demonstrated that hMSCs could exert a chondroprotective therapeutic role on early stage OA through paracrine signaling alone. In addition to this chondroprotective role, encapsulated hMSCs augmented the compensatory increases in osteophyte formation. The latter should be taken into strong consideration as many clinical trials using MSCs for OA are currently ongoing.

Keywords: Osteoarthritis, medial meniscal transection, human mesenchymal stem cells, cellular encapsulation, osteophytes, paracrine signaling, contrast enhanced micro-computed tomography.

***Address for correspondence:** Nick J. Willett, Atlanta Veteran Affairs Medical Center, 1670 Clairmont Rd, Room 5A-115, Decatur, GA 30033, USA.

Telephone number: +1 4043216111 Email: nick.willett@emory.edu

Copyright policy: This article is distributed in accordance with Creative Commons Attribution Licence (<http://creativecommons.org/licenses/by-sa/4.0/>).

Introduction

Osteoarthritis (OA) is the most common joints' chronic disease and remains one of the leading global causes of disability (Cisternas *et al.*, 2016; Vos *et al.*, 2012). Disease incidence is expected to continue rising with

the increasingly obese and aging global population (Vos *et al.*, 2012). OA is characterized by chronic degeneration of articular cartilage, with proteoglycan loss, chondrocyte hypertrophy, matrix fibrillation, erosion and lesion formation and eventually full-thickness loss of articular cartilage resulting in

bone-on-bone contact (Bertrand *et al.*, 2010; Martel-Pelletier, 2004). OA-associated phenotypic changes are not strictly limited to articular cartilage, as surrounding tissue is additionally altered, with osteophyte formation, synovial inflammation and subchondral bone remodeling (Loeser *et al.*, 2012). While physical therapy and weight loss improve functionality in patients with OA, current drugs (analgesics, viscosupplements, corticosteroid injections) only provide symptomatic relief (Messier *et al.*, 2004; Yu and Hunter, 2016). There is a notable need for development of a disease-modifying therapeutic for OA. Mesenchymal stem cells (MSCs) represent a promising treatment to target the disease, relying on their regenerative capacity along with their immunomodulatory and anti-inflammatory properties.

MSC therapeutics for cartilage regeneration are widely studied, in both the pre-clinical and clinical environment. Pre-clinical studies demonstrate the efficacy of autologous, allogeneic and xenogeneic MSC intra-articular injections for cartilage regeneration (Hatsushika *et al.*, 2013; Kim *et al.*, 2014; Pigott *et al.*, 2013; Saulnier *et al.*, 2016). While varied results are reported in OA as to the efficacy of xenogeneic cell sources, this remains an understudied area (Farrell *et al.*, 2016; Saulnier *et al.*, 2016). However, recent *in vivo* data, following intra-articular injections, demonstrate that xenogeneic MSCs do not elicit an increased immune response, suggesting these cells may be immunoprivileged in the short-term (Pigott *et al.*, 2013; Saulnier *et al.*, 2016). While these pre-clinical studies show improved cartilage repair with MSC treatment, much remains unknown and MSCs have yet to be translated into an effective clinical therapy (Mamidi *et al.*, 2016; Pers *et al.*, 2015; Yu and Hunter, 2016; Web ref. 1). MSCs may be acting through direct engraftment, in addition to paracrine signaling, in concert with the local environment (Grigolo *et al.*, 2009; Horie *et al.*, 2012; Sato *et al.*, 2012). However, MSC viability studies, following intra-articular injection, show short-term survival (~ 7 d) and small numbers of engrafted cells, indicating that the newly regenerated tissue derives mostly from the host cells (Horie *et al.*, 2012; Sato *et al.*, 2012; ter Huurne *et al.*, 2012). These findings suggest that the recruitment of endogenous cells may be a critical component to MSC therapies, through paracrine communication. Human MSCs (hMSCs) can secrete a wide range of paracrine factors to facilitate tissue remodeling, recruit stem and progenitor cells and modulate the immune response. In response to cartilage degeneration, hMSCs can induce tissue remodeling through secretion of factors such as interleukin (IL)-6 and stromal-cell-derived factor (SDF)-1 (Liu *et al.*, 2011; Namba *et al.*, 2007). hMSCs can also modulate the host immune response factors tumor necrosis factor alpha (TNF- α)-stimulated gene (TSG)-6, transforming growth factor (TGF)- β 1 and adenosine (Choi *et al.*, 2011; Kintscher *et al.*, 2002; Kunzmann *et al.*, 2006;

Shin *et al.*, 2018). Additionally, in graft-versus-host disease, MSC apoptosis, following delivery *in vivo* by systemic administration, further modulates the immune response; however, it is unknown if this is important in the context of local treatment of osteoarthritic joints (Galleu *et al.*, 2017). The relative contribution of hMSC paracrine factors, independent of direct cellular engraftment, is difficult to define.

Cellular encapsulation represents a promising means to isolate and study hMSC paracrine factors, independent of cellular engraftment, as the capsule provides a mechanical barrier between the encapsulated cells and the native host tissue. Sodium alginate, an inert heteropolysaccharide, is used as a vehicle to encapsulate various cell types for delivery (Orive *et al.*, 2003). Sodium alginate capsules can be formed with controlled porosity, allowing encapsulated MSCs to communicate with the surrounding native tissue through paracrine mechanisms, while retaining the cells inside the microcapsules (Landázuri *et al.*, 2012). Encapsulation of MSCs in semi-permeable alginate allows for diffusion of molecules into and out of the cell-containing microspheres, enabling them to sense signals from the diseased tissue and to secrete various factors into the surrounding environment. The molecular cut-off of proteins readily diffusible through the alginate capsule is ~ 80 kDa – through 24 h incubation of encapsulated fluorescent microspheres – thus allowing free transit of small cytokines, chemokines and growth factors while excluding larger proteins, such as IgG (Landázuri *et al.*, 2012). In a murine hind limb ischemia model, encapsulation of xenogeneic hMSCs increases cell survival, retention and pro-angiogenic activity at the ischemic injury site and intact capsules are recoverable up to 5 months post-implantation (Landázuri *et al.*, 2012). Furthermore, delivery of encapsulated xenogeneic hMSCs in a hydrogel patch post rat myocardial infarction demonstrates increased viable cell retention at the delivery site, improved cardiac function, decreased scar size and increased microvascular density (Levit *et al.*, 2013). The improved retention of hMSCs using this delivery method could be explained by alginate's partial protection from the host's immune-mediated clearance. Encapsulation of hMSCs was used in the present study to isolate the hMSC paracrine signaling properties from direct engraftment and to study the associated effects on the onset of OA.

There are currently many ongoing clinical trials using MSCs, but these have yet to translate into an effective clinical therapy (Mamidi *et al.*, 2016; Pers *et al.*, 2015; Yu and Hunter, 2016; Web ref. 1). In contrast, MSCs repeatedly show great promise in pre-clinical studies (Mamidi *et al.*, 2016; Pers *et al.*, 2015; Yu and Hunter, 2016). This motivates more detailed investigations into the MSC mechanism of action. Particularly, the role of paracrine action *versus* direct cellular engraftment of these cells need to be explored

further to better design cell-based therapies that will effectively translate to the human scale. The objective of the study was to examine the therapeutic efficacy of hMSCs with and without encapsulation in early stage post-traumatic OA. Equilibrium partitioning of a ionic contrast agent based micro-computed tomography (EPIC- μ CT) was used to quantitatively analyze changes in articular cartilage, osteophyte and subchondral bone morphologies. EPIC- μ CT is established and validated in reference to the gold standard in the musculoskeletal field, histopathology (Palmer *et al.*, 2006; Reece *et al.*, 2017; Thote *et al.*, 2013; Willett *et al.*, 2014; Willett *et al.*, 2016; Xie *et al.*, 2010). The hypothesis was that encapsulated hMSCs would have a therapeutic effect, through paracrine-mediated action, on the onset and development of early stage OA.

Materials and Methods

Surgical methods

Animal care and experiments were conducted in accordance with the institutional guidelines of the Atlanta Veteran Affairs Medical Center (VAMC) and experimental procedures were approved by the Atlanta VAMC Institutional Animal Care and Use Committee (IACUC) (Protocol: V004-15).

Weight-matched wild type male Lewis rats (strain code: 004; Charles River), weighing 300-350 g, were acclimatized for 1 week after they were received. A surgical instability animal model, medial meniscal tear (MMT), was used to induce OA (Bendele, 2001). Animals were anesthetized using isoflurane and injected subcutaneously with 1 mg/kg sustained-release buprenorphine (ZooPharm, Windsor, CO, USA). Skin over the medial aspect of the left femoro-tibial joint was shaved and sterilized. Blunt dissection was used to expose the medial collateral ligament (MCL), which was next transected to expose the meniscus. Then, a full-thickness cut was made through the meniscus at its narrowest point. Following transection of the meniscus, soft tissues were re-approximated and closed using 4.0 Vicryl sutures and the skin was closed using wound clips. Sham surgery was also performed in rats. For shams, the MCL was transected followed by closure of the skin without transection of the meniscus.

1 d post-surgery, MMT animals received 50 μ L intra-articular injections using a 25-gauge needle. Animals were injected with i) Hanks balanced salt solution (HBSS) ($n = 8$), ii) empty sodium alginate capsules ($n = 7$), iii) 5×10^5 hMSC/knee in HBSS ($n = 8$) or iv) 5×10^5 encapsulated hMSC (encap hMSC)/knee ($n = 8$). The cell dose (5×10^5 cells/knee) used for injection was the maximum concentration that could be encapsulated and delivered in a 50 μ L volume. Sham ($n = 8$) animals were not injected post-surgery.

3 weeks post-surgery, animals were euthanized by CO₂ inhalation. The MMT surgical model shows initial phenotypical changes associated with OA

at the standard 3 weeks post-surgery time point, including cartilage damage, osteophyte formation and subchondral bone changes (Bendele, 2001). This time point was matched with animal euthanasia to assess the therapeutic effects of encapsulated hMSCs on the onset and early development of OA. Left hind limbs were collected and fixed in 10 % neutral buffered formalin.

Cell culture and characterization

hMSCs derived from bone marrow were obtained from Emory Personalized Cell Therapy core facility at Emory University. hMSCs were cultured in complete minimum essential medium Eagle- α modification (α -MEM; 12561; Gibco) supplemented with 10 % heat-inactivated fetal bovine serum (FBS) (S11110H; Atlanta Biologicals, Lawrenceville, GA, USA), 2 mM L-glutamine (SH3003401; HyClone, Logan, UT, USA) and 100 μ g/mL penicillin/streptomycin (P/S) (B21110; Atlanta Biologicals) and sub-cultured at 70 % confluency. For lentiviral preparation, HEK 293T cells (CRL-3216TM; ATCC) were cultured in complete Dulbecco's modified Eagle's medium (DMEM; D5546; Sigma-Aldrich). hMSC phenotype was confirmed by adipogenic, chondrogenic and osteogenic differentiation (kit protocols A1007001, A1007101, A1007201; StemPro™ Differentiation Kits, ThermoFisher Scientific). Flow cytometry was also used to characterize the hMSCs. A hMSC Verification Flow Kit (FMC020; R&D Systems) was used to confirm that MSCs expressed characteristic MSC surface markers (CD73, CD90, CD105) and lacked hematopoietic markers (CD45, CD34, CD11b, CD79A, HLA-DR).

Encapsulation of hMSCs

1×10^6 cells/mL passage 4 hMSCs were suspended in 1 % ultrapure low viscosity sodium alginate LVG (UP-LVG) (4200006; PRONOVA™ UP LVG; NovaMatrix, Sandvika, Norway). An electrostatic encapsulator (VARV1; Nisco Engineering AG, Zurich, Switzerland) with a 0.2 μ m nozzle, 2.5 mL/h flow rate and 7 kV voltage was used. Capsules were gelled in 50 mM BaCl₂. hMSC capsules were washed six times with 0.9 % saline (NaCl), re-suspended to the appropriate dose and stored at 4 °C in saline until injection. hMSC viability was confirmed with Live/Dead™ Viability/Cytotoxicity kit (L3224; Invitrogen) following encapsulation. Cell viability was quantified using ImageJ software. All rats were injected within 2 h of hMSC encapsulation.

In vitro capsule viability study

Immediately following encapsulation and washing, encapsulated hMSCs were placed in complete α -MEM medium in 12-well plates and cultured at 37 °C, 5 % CO₂ until different time points were reached (1, 3, 5, 7, 9, 14, 21, 28 and 35 d post plating), with medium changed every 3 d. At the specified time point, hMSC viability in capsules was determined with Live/Dead™ Viability/Cytotoxicity kit (Invitrogen).

Percentage viability was quantified by comparing the relative number of live cells stained with calcein-AM to ethidium-homodimer-stained dead cells counted through ImageJ software on serial z-stacked images, each containing 3-17 capsules, obtained by a confocal microscope, at 3.99 μm z-thickness. Image collection and quantification was completed for every 14 sections, ensuring encapsulated cells were counted only once.

Lentiviral vector packaging

The lentiviral vector, pLenti CMV Puro LUC (w168-1) (#17477; Addgene, Cambridge, MA, USA), contains a CMV promoter upstream of the firefly luciferase gene and a murine phosphoglycerate kinase (pGK) promoter upstream of a puromycin resistance gene (Campeau *et al.*, 2009). Second generation packaging plasmids were used for lentiviral packaging. pLenti CMV Puro LUC was co-transfected with a packaging plasmid, psPAX2 (#12260; Addgene) and a VSV-G-envelope-expressing plasmid, pMD2.G (#12259; Addgene), in a 4 : 2 : 1 ratio into HEK 293T cells using Lipofectamine™ 3000 Transfection Reagent (L3000008; Invitrogen) and Opti-MEM™ I Reduced Serum Medium (31985062; ThermoFisher Scientific), as recommended by the manufacturer. 70 % confluent HEK 293T cells were transfected with the plasmid mixture in transfection medium (DMEM + 10 % FBS + 2 mM glutamine). Transfection medium was replaced with collection medium (DMEM + 10 % FBS + 2mM glutamine + 100 $\mu\text{g}/\text{mL}$ P/S at 18 h post-transfection. Collection medium was harvested at 41, 48 and 65 h post-transfection, pooled, centrifuged at 400 $\times g$ for 5 min at 4 °C and filtered through a 0.45 μm polyethersulfone membrane syringe filter (6780-2504; Whatman). The viral supernatant was concentrated using the PEG-it Virus Precipitation Solution (LV810A; System Biosciences, Palo Alto, CA, USA) and stored at -80°C.

hMSC lentiviral transduction

50-60 % confluency passage 3 hMSCs were transduced with 7 mL of concentrated viral supernatant in T175 flasks (353112; Corning) with 8 $\mu\text{g}/\text{mL}$ polybrene (AL-118; Sigma-Aldrich) in complete DMEM containing 10 % FBS. Antibiotic selection commenced 48 h post-transduction and continued throughout culture by replacing medium with DMEM supplemented with 10 % FBS, 2 mM glutamine, 100 $\mu\text{g}/\text{mL}$ P/S and 0.6 $\mu\text{g}/\text{mL}$ puromycin (H9268; Sigma-Aldrich). Transduced hMSCs were passaged when reaching 60-90 % confluency. Luciferase expression was confirmed through addition of D-luciferin (L-123-250; Gold Biotechnology, St. Louis, MO, USA) to transduced hMSCs, with luminescence measurements made with a microplate luminometer (BioTek Synergy™ H1, Winooski, VT, USA). The hMSCs transduced with the lentivirus were used for bioluminescent-cell-tracking studies only. The hMSCs injected for therapeutic efficacy studies evaluated by EPIC- μCT analysis did not contain the firefly luciferase gene.

Bioluminescence imaging (BLI)

Naïve Lewis rats were injected intra-articularly with 5×10^5 cells/knee of either encapsulated or non-encapsulated luciferase-expressing hMSCs ($n = 5$ for each condition). Following cellular injections at day 0, animals received an intra-articular injection of 40 mg/mL luciferin (Promega™ Beetle Luciferin, Potassium Salts, ThermoFisher Scientific) diluted in α -MEM (12561; Gibco). Incubation times for initial and subsequent luciferin injections were optimized in a prior pilot study, in which incubation time points that yielded maximum signal were selected, using the Bruker In-Vivo Xtreme. At day 0, a 30 min incubation time was allotted before BLI was conducted using the Bruker In-Vivo Xtreme imaging system. Additional BLI readings were performed at 1, 3, 5, 7 and 9 d post hMSC injections, with subsequent luciferin injections administered 20 min (incubation time) before readings. The minimum detection limit for luciferase-expressing hMSCs, *in vitro*, using the In-Vivo Xtreme imaging system was determined to be 10,000 cells (data not shown). Bioluminescence intensity values were quantified using ImageJ software and plotted as percentage of maximum intensity. Background (naïve animals with luciferin alone) images ($n = 4$) were also collected and the averaged intensity value was subtracted from intensity values collected for all study samples.

EPIC- μCT analysis of articular cartilage, osteophytes and subchondral cone

EPIC- μCT was used to quantitatively evaluate articular cartilage structure and composition, osteophyte volumes and subchondral bone morphology (Fig. 1), as previously described (Palmer *et al.*, 2006; Reece *et al.*, 2017; Thote *et al.*, 2013; Willett *et al.*, 2014; Willett *et al.*, 2016; Xie *et al.*, 2010). Fixed tibiae were dissected, carefully exposing the articular cartilage of the medial tibial plateau and stored in phosphate-buffered saline (PBS). Before scanning, the proximal tibia was immersed for 30 min at 37 °C in 2 mL of 30 % Hexabrix® 320 contrast reagent (NDC 67684-5505-5; Guerbet, Villepinte, France) and 70 % PBS (Palmer *et al.*, 2006). Tibiae were gently patted dry, placed in covered sample chambers and scanned using Scanco μCT 40 (Scanco Medical, Brüttisellen, Switzerland). Scan parameters were: 45 kVp, 177 μA , 200 ms integration time, 16 μm voxel size, ~ 27 min scan time (Palmer *et al.*, 2006). Raw scan data were automatically reconstructed to two-dimensional (2D) grayscale tomograms and orthogonally transposed to yield coronal sections.

Coronal sections were evaluated in the medial $\frac{1}{3}$ of the medial tibial plateau for articular cartilage parameters, as this region demonstrates high damage incidence in the MMT-induced OA model (Thote *et al.*, 2013). Contours were constructed around medial tibial cartilaginous surfaces. Thresholding was used to separate cartilage from air and bone, on the medial $\frac{1}{3}$, with thresholds of 110 and 435 mg hydroxyapatite per cubic centimeter (mg HA/cm³), respectively (Fig.

1b,c). Results yielded average articular cartilage volume, thickness and attenuation. Cartilage attenuation is a parameter inversely proportional to sulfated glycosaminoglycan (sGAG) content (Palmer *et al.*, 2006). More specifically, degraded cartilage has a lower sGAG content so that a larger amount of contrast agent integrates into the cartilage matrix and, therefore, reflects a higher attenuation value (Palmer *et al.*, 2006).

Osteophytes are defined as a thickening of tissue on the most medial aspect of the tibial condyle (van der Kraan and van der Berg, 2007). Osteophyte volume is evaluated using the coronal section (Reece *et al.*, 2017; Willett *et al.*, 2016). The osteophyte cartilage volume was measured in volumes of interest that excluded the peripheral soft tissue. For cartilaginous osteophyte volumes, threshold values of 110–435 mg HA/cm³ were used to segment the cartilage from air and bone. For mineralized osteophyte volume measurements, thresholds of 435–1000 mg HA/cm³

were used to exclude mineralized tissue volumes from surrounding cartilage, soft tissue and air (Fig. 1f–i). Total osteophyte volumes were calculated by adding the respective volumes of cartilaginous and mineralized osteophytes.

Subchondral bone was analyzed over the entire medial tibial plateau using coronal sections. Thresholds of 435–1000 mg HA/cm³ were used to separate the bone from the surrounding cartilage and soft tissue (Fig. 1d,e). Average subchondral bone volume, thickness, attenuation (density) and porosity were measured.

Surface roughness analysis of articular cartilage

Serial coronal sections of the medial tibial plateau, obtained from EPIC- μ CT scans, were exported as 2D grayscale TIFF images and imported into MATLAB R2017a (MathWorks, Natick, MA, USA). A custom algorithm scanned section images sequentially to create three-dimensional (3D) digital representations

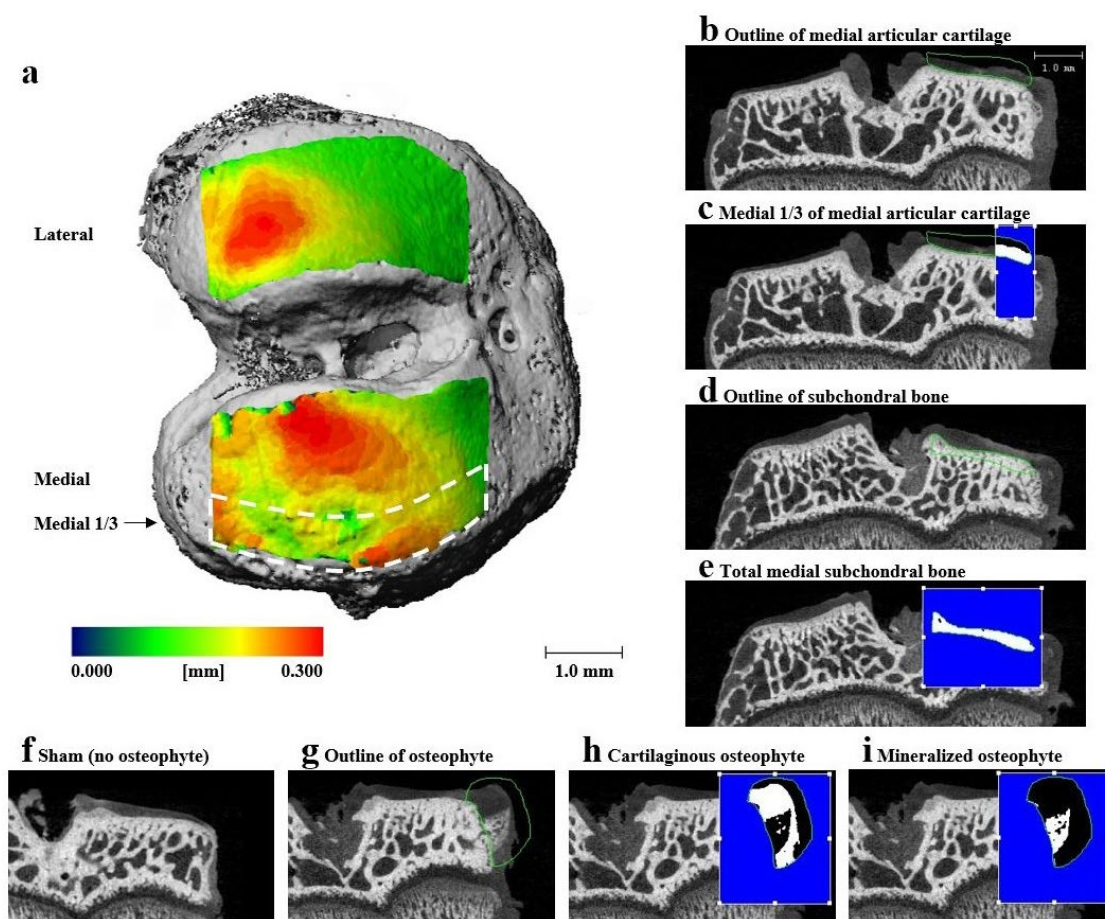


Fig. 1. Representative EPIC- μ CT images demonstrating articular cartilage, osteophyte and subchondral bone volume of interest (VOI). (a) Rat tibial articular cartilage thickness map overlays on bone indicating articular cartilage VOI. Color heat map indicates cartilage thickness according to the scale bar (blue \sim 0.0 mm; red \sim 0.3 mm) (b) Representative images of coronal sections of rat tibial joint showing outline of total medial articular cartilage, (c) medial $\frac{1}{3}$ (indicated in white) of medial articular cartilage, outline of (d) medial tibial subchondral bone and (e) cortical subchondral bone (indicated in white) of medial tibia. Representative coronal sections of medial tibial joint illustrating (f) no osteophyte in sham joint, (g) contour of osteophyte in MMT joint, (h) cartilaginous osteophyte volume (indicated in white) in MMT joint and (i) mineralized osteophyte volume (indicated in white) in MMT joint. Scale bar in (a) is universal for all representative images of coronal sections.

of respective cartilaginous surfaces (Reece *et al.*, 2017). Briefly, cartilage surfaces were fitted with a 3D polynomial surface: fourth order along the ventral-dorsal axis and second order along the medial-lateral axis. Surface roughness was calculated as the root mean square of differences between the articular cartilage surface and the polynomial fitted surface. Surface roughness was analyzed over the medial 1/3 of the medial tibial plateau.

Histology

Tibiae were decalcified with Immunocal (SKU-1414-32; StatLab, McKinney, TX, USA) for 7-10 d. Dehydrated samples were processed into paraffin-embedded blocks, 5 µm-thick sectioned and stained with hematoxylin and eosin (H&E; Fisherbrand™ 517-28-2, Waltham, MA, USA) or safranin O and fast green (Saf-O; Electron Microscopy Sciences® 20800, Hatfield, PA, USA), following manufacturer protocols.

Statistical analysis

All quantitative data are presented as mean ± standard deviation (SD). The BLI study was evaluated by repeated measures using two-way analysis of variance (ANOVA) (factors: time point and delivery method) with *post-hoc* Tukey Honest analysis. Articular cartilage and subchondral bone parameters were evaluated using one-way ANOVA with *post-hoc* Tukey Honest analysis. Osteophyte parameters were evaluated using one-way ANOVA with a nonparametric *post-hoc* Bonferroni analysis. Statistical significance was set at $p < 0.05$. All data were analyzed using GraphPad Prism software version 6.0 (GraphPad Software Inc., La Jolla, CA, USA).

Results

Encapsulated hMSC characterization

To characterize the hMSCs used for therapeutic delivery, differentiation and phenotypic characterization assays were performed prior to encapsulation. hMSC differentiation was confirmed with immunofluorescence staining for type II collagen of paraffin-sectioned pellets, oil red O staining and alizarin red S staining for chondrogenesis, adipogenesis and osteogenesis, respectively (Fig. 2a-c). Additionally, hMSCs were confirmed to be positive for typical MSC markers, including CD73, CD90 and CD105, and negative for hematopoietic markers, including CD45, CD34, CD11b, CD79A and HLA-DR, by fluorescence-activated cell sorting analysis (FACS) (Fig. 2d).

hMSC were encapsulated in sodium alginate microspheres. The average diameter of encapsulated hMSC microspheres was 144 ± 16 µm (Fig. 2e). Encapsulated hMSC viability immediately following encapsulation was 96 ± 2.4 % (Fig. 2f).

Encapsulated hMSC tracking following intra-articular injection

Cellular encapsulation improves MSC survival in both hindlimb ischemia and myocardial infarct models (Landázuri *et al.*, 2012; Levit *et al.*, 2013). However, no studies show the same augmented cell survival in knee joints following intra-articular delivery of encapsulated hMSCs. Luciferase-expressing hMSCs were used to analyze the effect of encapsulation on cellular viability, retention, proliferation and metabolic state both in culture and following intra-articular injections in rat knees (Allen *et al.*, 2014; Levit *et al.*, 2013). *In vitro* viability studies demonstrated that encapsulated hMSCs were approximately 75 % viable for the first 7 d following encapsulation and remained approximately 30 % viable for at least 35 d under standard culture conditions (Fig. 3a). Representative maximum projection images are included displaying encapsulated cells at four key study time points (Fig. 3b).

In vivo bioluminescence was plotted as percentage of maximum intensity, with maximum intensity (100 %) being expressed at day 0 for all animals. Encapsulated and non-encapsulated hMSCs showed similar initial decreases in bioluminescence, as no differences in signal were detectable for the first three study time points (day 0, 1 and 3). However, at later time points (day 5 and 7), non-encapsulated hMSCs had a small but statistically significant decrease in bioluminescence when compared to encapsulated hMSCs. While complete loss of hMSC bioluminescent signal (<1 % of original intensity) was observed at day 7, encapsulated hMSCs yielded only ~6 % cellular bioluminescence at this time point, with complete clearance at day 9 (Fig. 3c). Qualitative data, in the form of representative images selected from key time points for both groups, are included (Fig. 3d).

Full joint histology was performed on the hind limbs of animals ($n = 2$ /time point) injected with encapsulated hMSCs, at 3 and 9 d post-injection, to qualitatively assess cell and capsule retention following intra-articular injection. Capsules can be readily visualized with Saf-O, a cationic stain that binds to negatively charged alginate (Schmitz *et al.* 2010). Intact alginate capsules containing hMSCs were visible within the infrapatellar fat pad of the knee at day 3 (Fig. 4a-c). Alginate capsules were also visible in the joint space at day 9, surrounded by capsule remnants (Fig. 4d,e). While no hMSCs could be identified within the capsules at day 9, lacunae empty or potentially containing cell debris were present in the capsules. Identification of encapsulated hMSCs at day 3 and the absence of hMSCs in alginate capsules at day 9 was consistent with the *in vivo* bioluminescent analysis (Fig. 3c).

Qualitative analysis of the therapeutic efficacy of encapsulated hMSCs in OA

Encapsulated hMSCs were injected 1 d post-surgery to assess the effects of the paracrine signaling

properties of hMSCs, independent of direct cell engraftment, in delaying the onset of MMT-induced OA. Tibiae were collected 3 weeks post-surgery, the time point in the MMT model corresponding to the presentation of OA-associated phenotypical cartilage degeneration (Janusz *et al.*, 2002). Histology was performed on collected tibiae to qualitatively analyze effects of encapsulated hMSC therapeutics on OA. Representative histological images of coronal tibial sections showed proteoglycan loss, degeneration of the cartilage surfaces and development of cartilaginous osteophytes in all MMT conditions (Fig. 5b-e,g-j). The sham group showed good proteoglycan staining and smooth cartilage surfaces with no osteophyte development (Fig. 5a,f). However, no further analysis was performed on H&E and Saf-O images as EPIC- μ CT was used to quantitatively analyze the therapeutic efficacy of encapsulated hMSCs on OA. Representative coronal slices from both histology and EPIC- μ CT showed qualitatively similar disease progression over the 3-week study time course (Fig. 5).

EPIC- μ CT quantitative analysis of articular cartilage in the MMT study

EPIC- μ CT was implemented to quantitatively analyze the effects of encapsulated hMSCs on MMT-induced OA development. Changes in articular cartilage structure and composition of the medial $\frac{1}{3}$ of the medial tibial condyle were quantified in 3D. Representative coronal cuts of contrast-enhanced cartilage EPIC- μ CT attenuation maps of the whole medial tibial plateau showed qualitatively higher attenuation of cartilage for the MMT + saline (MMT/saline), MMT + empty capsules (MMT/empty caps), MMT + hMSCs (MMT/hMSC) and MMT + encapsulated hMSCs (MMT/encap hMSCs) when compared to sham control (red = high attenuation, low sGAG content; green = low attenuation, high sGAG content) (Fig. 5k-o). Quantitative analysis of EPIC- μ CT images within the medial $\frac{1}{3}$ of the medial tibial plateau showed a significant increase in attenuation, representative of a decrease in sGAG content, for all MMT conditions as compared to the sham control (Fig. 6a). However, no significant

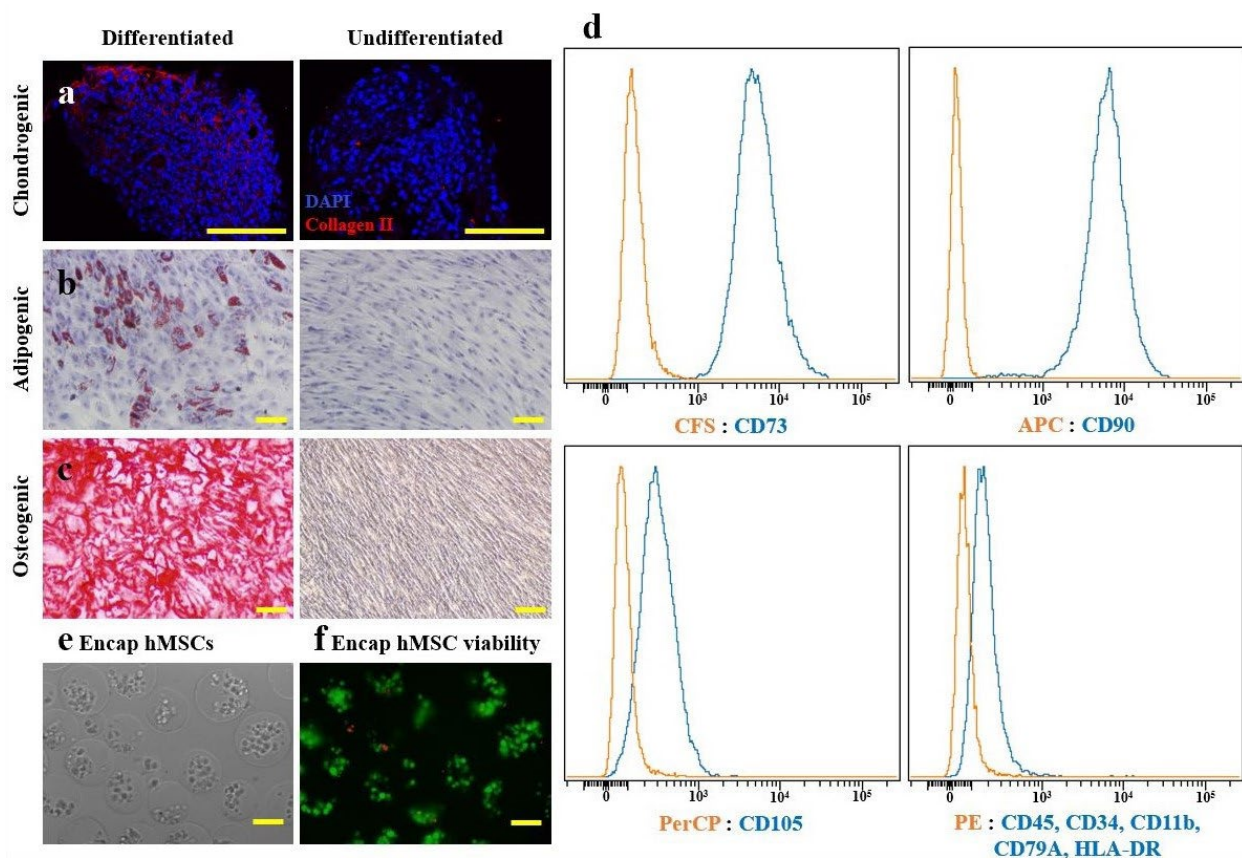


Fig. 2. Encapsulated hMSC characterization. Multipotency of hMSCs confirmed prior to encapsulation, as cultured hMSCs were differentiated into (a) chondrogenic, (b) adipogenic and (c) osteogenic phenotypes as demonstrated by collagen type II, oil red O and alizarin red staining. (d) FACS analysis demonstrated that hMSCs expressed typical MSC surface markers: CD73, CD90 and CD105; but not hematopoietic markers: CD45, CD34, CD11b, CD79A and HLA-DR. (e) Light microscopic appearance of encapsulated hMSCs immediately following sodium alginate encapsulation showed capsule diameters of $170 \pm 27 \mu\text{m}$. (f) Fluorescent viability assay, staining live cells green and dead cells red, showed $96 \pm 2.4 \%$ of cells were viable immediately following encapsulation in sodium alginate. Scale bars = $100 \mu\text{m}$.

differences in attenuation were noted between any of the MMT conditions. Cartilage thickness of the medial 1/3 of the medial tibial condyle showed significant increases in thickness values for all MMT conditions in comparison to the sham control (Fig. 6b). Additionally, the encapsulated hMSCs condition yielded attenuated cartilage thickness increases in comparison to all other MMT conditions. MATLAB surface roughness analysis of the medial 1/3 of the medial tibial plateau showed an increased articular cartilage surface roughness for all MMT conditions as compared to sham animals (Fig. 6c). Furthermore, the encapsulated hMSC condition yielded attenuated surface roughness values in comparison to all other MMT conditions. Additionally, the saline group yielded augmented surface roughness in comparison to all MMT conditions. Qualitative analysis of the surface roughness was performed by subtracting individual 3D polynomial surfaces from the

corresponding cartilage surface renderings, relative to the sham control (Fig. 6d-h).

EPIC- μ CT quantitative analysis of osteophytes and subchondral bone in MMT study

Osteophytes are a thickening and partial mineralization of cartilage tissue at the marginal edge of the medial tibial plateau and are a staple of OA development (van der Kraan and van der Berg, 2007). Cartilaginous and mineralized tissue volumes on the most medial aspect of the medial tibial condyle were quantified in 3D by EPIC- μ CT. Total osteophyte volume (cartilaginous + mineralized tissue volume) was significantly larger for all MMT conditions in comparison to the sham control (Fig. 7a). Furthermore, encapsulated hMSCs yielded significantly larger volumes than both the saline and empty capsule groups but not than the hMSC group. Cartilaginous osteophyte volumes were also significantly larger

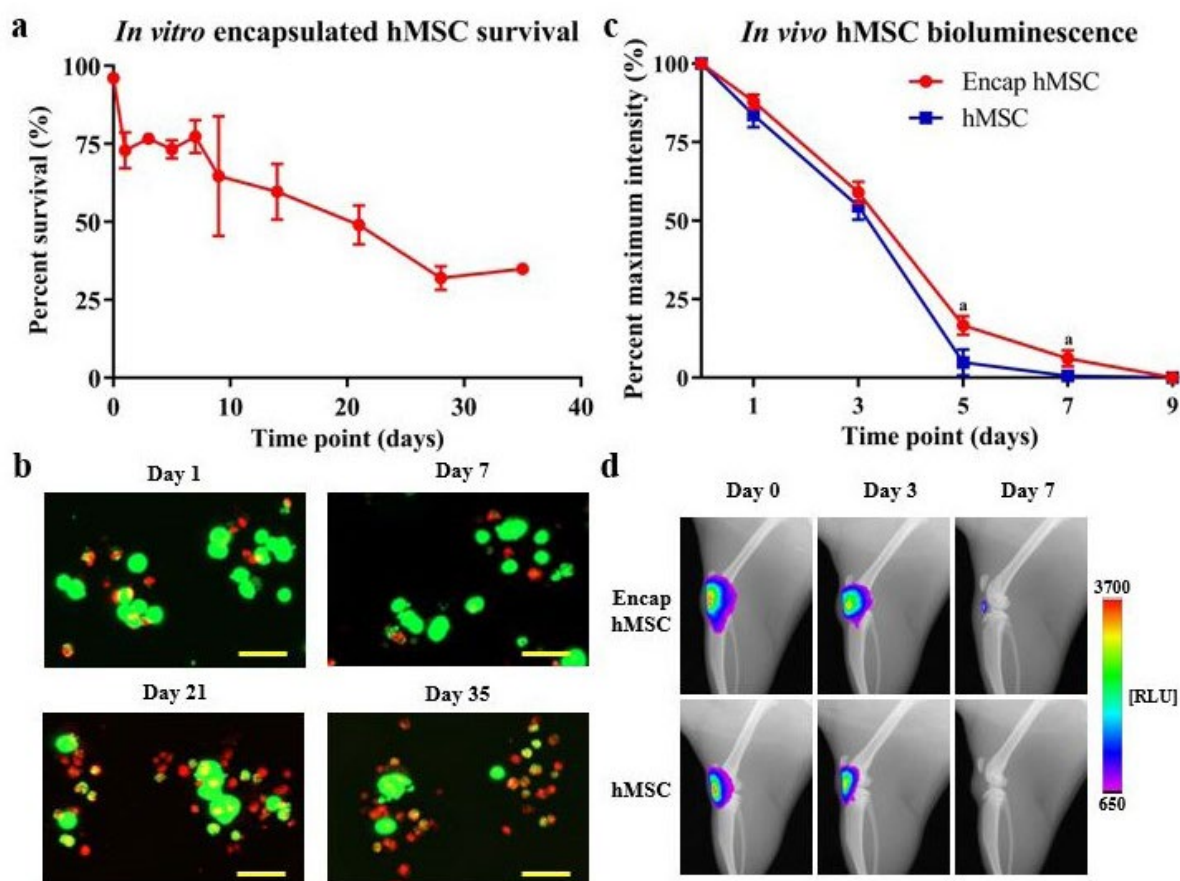


Fig. 3. Encapsulated hMSC *in vitro* viability and *in vivo* tracking following intra-articular injection into naïve joints. (a) hMSCs in alginate capsules remained 70-80 % viable at early time points (days 1-7), with viability slowly declining to approximately 30 % at day 28 and 35. (b) Representative maximum projection images of capsules from key time points qualitatively demonstrated encapsulated hMSC viability over time *in vitro*. (c) *In vivo* bioluminescent imaging demonstrated an overall increase in quantified bioluminescence of encapsulated hMSCs *versus* hMSCs. Initial time points showed similar bioluminescent signals, while later time points (day 5 and 7) demonstrated differences in bioluminescent signal. Complete clearance of hMSCs (< 1 %) was observed at day 7 and complete clearance of encapsulated hMSCs was observed at day 9. (d) Representative images, from key study time points, of the rat knee joint qualitatively illustrate bioluminescent signal for each of the study groups. RLU: relative luminescence units with a color heat map according to the scale bar. Data presented as mean \pm SD. $n = 5/\text{group}$ for *in vivo* study. $^*p < 0.05$. Scale bars = 50 μm .

for all MMT conditions in comparison to the sham control (Fig. 7b). Furthermore, encapsulated hMSCs also showed increased cartilaginous osteophyte volumes in comparison to all other conditions, except hMSCs. Histological and EPIC- μ CT representative images qualitatively confirmed the results of the cartilaginous osteophyte volume analysis (Fig. 5f-j,k-o). Mineralized osteophyte volumes showed an increase for all MMT conditions as compared to the sham control (Fig. 7c). Additionally, encapsulated hMSCs yielded increased mineralized osteophyte volumes in comparison to all other experimental groups. EPIC- μ CT representative images qualitatively confirmed the results of the mineralized osteophyte volume analysis (Fig. 5k-o). Subchondral bone, the layer of bone just below the articular cartilage in load-bearing joints, showed an increased thickness in all MMT conditions as compared to the sham control (Fig. 7d). No significant differences were found between any of the MMT conditions for this parameter.

Discussion

The clinical need for disease-modifying drugs for the treatment of OA remains unmet. MSCs represent a promising treatment to target OA, relying on their regenerative capacity in combination with their immunomodulatory and anti-inflammatory properties (Choi *et al.*, 2011; Kintscher *et al.*, 2002; Kunzmann *et al.*, 2006; Liu *et al.*, 2011; Namba *et al.*, 2007; Shin *et al.*, 2018). Numerous clinical trials using MSCs are ongoing, but these have yet to translate into an effective clinical therapy, despite MSCs showing great promise on the pre-clinical side (Mamidi *et al.*, 2016; Pers *et al.*, 2015; Yu and Hunter, 2016; Web ref. 1). This motivates more detailed investigations into the MSC mechanism of action. More specifically, the main mechanism of action of these cells following intra-articular injection into the knee space: paracrine action *versus* cellular engraftment. The objective of the study was to quantitatively assess the efficacy of encapsulated hMSCs as a disease-modifying

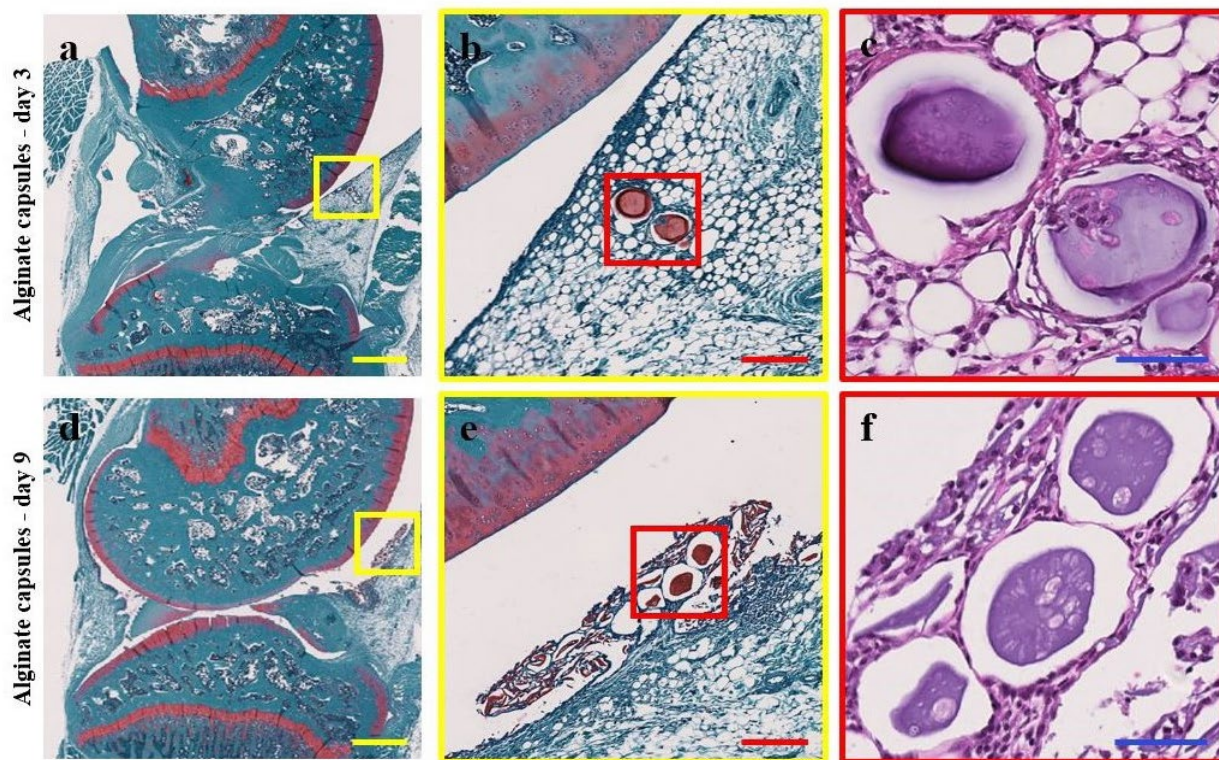


Fig. 4. Representative histological images, single images at three separate magnifications, of full joint histology of rat hind limb knee joints at (a-c) 3 d and (d-e) 9 d post injection of encapsulated hMSCs. (a,b) At day 3, Saf-O-stained joints showed the presence of sodium alginate capsules (stained red) in the infrapatellar fat pad. (c) H&E staining demonstrated the presence of encapsulated cells in the sodium alginate capsules at this time point. (d,e) Saf-O staining at day 9 displayed intact sodium alginate capsules in the synovial lining of the knee joint space surrounded by remnants of broken down capsules. (f) No encapsulated cells were identifiable at day 9, as demonstrated by H&E staining, but lacunae were identifiable appearing either empty or containing cell debris. In each image, the anterior hindlimb is located on the right and the posterior hindlimb on the left. Scale bars: yellow = 1 mm, red = 200 μ m, blue = 60 μ m.

therapeutic for early stage OA in a pre-clinical rat model.

hMSC encapsulation allows the study of the paracrine signaling properties of these cells independently of direct engraftment, as the capsule provides a mechanical barrier preventing the direct incorporation of the hMSCs into the native tissue (Landázuri *et al.*, 2012). Additionally, encapsulation improves MSC survival, which is critical for the therapeutic efficacy (Landázuri *et al.*, 2012; Leijts *et al.*, 2017; Levit *et al.*, 2013). To study the effects encapsulation would have on viability, retention, proliferation and metabolic state of hMSCs, a bioluminescence-tracking study was performed using luciferase-expressing hMSCs. While encapsulation yielded a statistically significant increase in hMSC bioluminescence, the enhancement of cell bioluminescent signal was not as pronounced as was initially hypothesized. The initial hypothesis was based on a previous work in a rat myocardial infarction model showing a sizable increase in the bioluminescent signal of the encapsulated hMSCs (Levit *et al.*, 2013). Even though Levit *et al.* (2013) show similar encapsulated hMSC bioluminescent signal detection for approximately 7 d, hMSCs alone yield an attenuated bioluminescence 1 d post-injection. However, in the present study, the bioluminescence of the non-encapsulated hMSCs (~7 d) was consistent with a previous report using intra-articular injections

(Horie *et al.*, 2012). Van Buul *et al.* (2014) show that non-encapsulated hMSCs can survive for up to 14 d following intra-articular injections in a rat model; however, one key difference is that those results are obtained using allogeneic MSC sources. While many questions remain as to the effects of cell sourcing, particularly the utilization of an allogeneic *versus* xenogeneic source, numerous reports demonstrate decreased cell variability when using xenogeneic *vs.* allogeneic cells (Lin *et al.*, 2012; Niemeyer *et al.*, 2008). Furthermore, while previous studies demonstrate beneficial effects of encapsulation on hMSC viability, direct comparison of these reports to the present study was confounded by the various capsule sizes employed and the different sites of delivery employed, as each location could contain different clearance kinetics, mechanical loading and immune response components (Landázuri *et al.*, 2016; Leijts *et al.*, 2017; Levit *et al.*, 2013). In the present study, histological analysis of alginate capsule retention showed the presence of encapsulated cells at day 3 post-injection, consistent with the bioluminescent data, but cells were not identifiable in the capsules at day 9. However, at day 9, the capsules did show open spaces resembling lacunae that were either empty or contained cell debris, suggesting potential cell apoptosis. To confirm that this cell death was not due to technical issues with encapsulation, an *in vitro* study was performed demonstrating

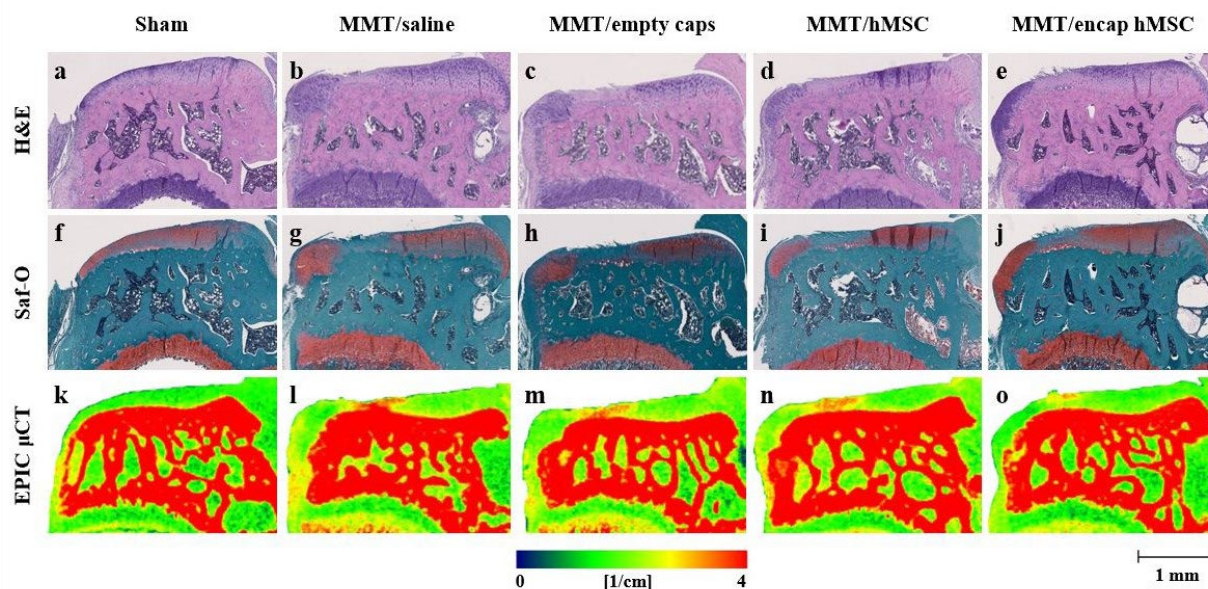


Fig. 5. Representative histology and EPIC- μ CT coronal images of medial tibial condyle following encapsulated hMSC treatment. (a-e) H&E- and (f-j) Saf-O-stained MMT joints showed no cartilage damage or osteophyte development in (a,f) sham control; (b-e,g-j) proteoglycan loss, degeneration of cartilaginous surfaces and osteophyte development in all MMT conditions. (k-o) Corresponding EPIC- μ CT images showed similar disease progression as shown by histology. (k) No cartilage damage was observed in sham control; (l-o) increased areas of cartilage attenuation, specifically in the medial $\frac{1}{3}$, was observed in all MMT conditions in addition to osteophyte volumes. Red indicates higher cartilage attenuation, corresponding to lower proteoglycan content. In all images, the medial tibial condyle is located on the left and the lateral tibial condyle on the right. Scale bar (bottom right corner) is universal for all histology and EPIC- μ CT representative images.

encapsulated hMSC survival for up to 35 d. While cell viability is a key component of the therapeutic efficacy of MSC treatments, recent reports suggest that hMSC apoptosis may play a key role in the immunomodulatory properties of these cells (Mamidi *et al.*, 2016; Pigott *et al.*, 2013; Galleu *et al.*, 2017). Overall, while the study demonstrated that hMSC encapsulation slightly enhanced bioluminescent signal in comparison to hMSCs alone, both groups showed no signal by day 9 post-injection. One limitation of this bioluminescent technique was that hMSC viability, retention, proliferation and metabolic state could not be studied independently. Further study will be needed to discriminate the potential individual contributions of each of these cellular properties.

To study the therapeutic effects of encapsulated hMSCs, EPIC- μ CT analysis was used to quantitatively evaluate changes in articular cartilage structure and composition, osteophyte volumes and subchondral

bone morphology. EPIC- μ CT data showed articular cartilage lower thickness and increased surface roughness in the encapsulated hMSC group in comparison to all other MMT conditions in the early stages of OA, as the therapeutic was delivered at the time of a traumatic injury to the joint but before OA had developed. Swelling of the articular cartilage precedes fibrillation development and augmented surface roughness in the early stages of OA (Bertrand *et al.*, 2010). Therefore, encapsulated hMSCs showed a chondroprotective role in early OA as they were associated with both attenuated swelling of articular cartilage and surface roughness as compared to the control groups. These findings were consistent with pre-clinical OA models showing decreased cartilage degeneration and a cartilage protective effect in MSC-treated animals (Diekman *et al.*, 2013; Murphy *et al.*, 2003; Toghraie *et al.*, 2012). Furthermore, the chondroprotective role of MSCs in OA is reported in *ex vivo* human tissue samples with MSC treatments

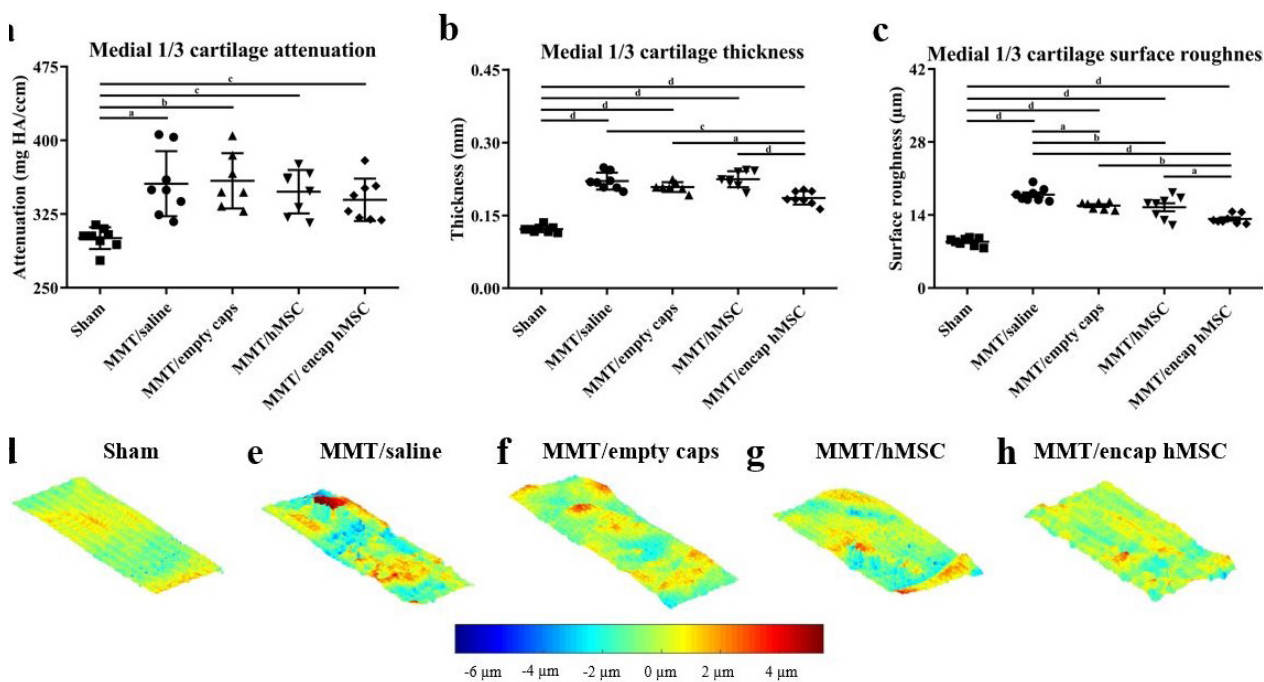


Fig. 6. EPIC- μ CT quantification of articular cartilage structure and composition in the medial $\frac{1}{3}$ of the medial articular cartilage in MMT joints treated with encapsulated hMSCs. (a) Cartilage attenuation was significantly increased in all MMT conditions as compared to sham control. (b) Cartilage thickness was significantly increased in all MMT conditions as compared to sham control; encapsulated hMSCs attenuated increases in cartilage thickness as compared to all other MMT conditions. (c) Cartilage surface roughness was significantly increased in all MMT conditions as compared to sham control; saline augmented cartilage surface roughness as compared to all other MMT conditions; encapsulated hMSCs attenuated increases in cartilage surface roughness as compared to all other MMT conditions. (d-h) Representative differential surfaces illustrating surface roughness of the medial $\frac{1}{3}$ of the articular cartilage of the medial tibial condyle. Differential maps were generated by subtracting individual 3D polynomial surfaces from the corresponding cartilage surface renderings. In these images, red indicates points that are more proximal and blue points that are further distal. (e-h) Qualitative analysis of the cartilage surfaces demonstrated increased surface roughness in all MMT conditions relative to the sham control in (d). (h) The representative surface for encap hMSCs also displayed decreased surface roughness when compared to all other MMT conditions (e-g). Data presented as mean \pm SD. $n = 7$ /group for MMT/empty caps; $n = 8$ /group for all other conditions. ^a $p < 0.05$; ^b $p \leq 0.01$; ^c $p \leq 0.001$; ^d $p \leq 0.0001$.

yielding a significant reduction in the expression of fibrotic and hypertrophic markers (Maumus *et al.*, 2013). The data from the present study showed that independently of direct engraftment, hMSCs could exert a chondroprotective therapeutic effect in early OA, reinforcing the significance of the MSC paracrine signaling properties in OA treatment. One limitation of the study was the lack of secretome analysis on the hMSCs following injection; the successful recovery of cells following intra-articular delivery is technically challenging but would provide substantial information if a reliable approach would be used. This limitation motivates further study into the identification of factors being released by hMSCs when stimulated by the osteoarthritic environment. hMSC paracrine signaling properties

show great therapeutic potential in protecting the joint cartilaginous surfaces in early OA but the secondary effects of these hMSC communication mechanisms must also be considered in assessing overall therapeutic efficacy.

OA-associated pathologies are not limited to phenotypic changes in the articular cartilage but can also affect the surrounding tissue, through the formation of osteophytes, synovial hyperplasia and subchondral bone sclerosis (Loeser *et al.*, 2012). Osteophytes are clinically defined as bony outgrowths – containing a fibrocartilaginous cap that forms on the margins of weight-bearing joints – and are a staple of OA development (van der Kraan and van der Berg, 2007). EPIC- μ CT quantitative analysis showed an increase in mineralized osteophyte volume for

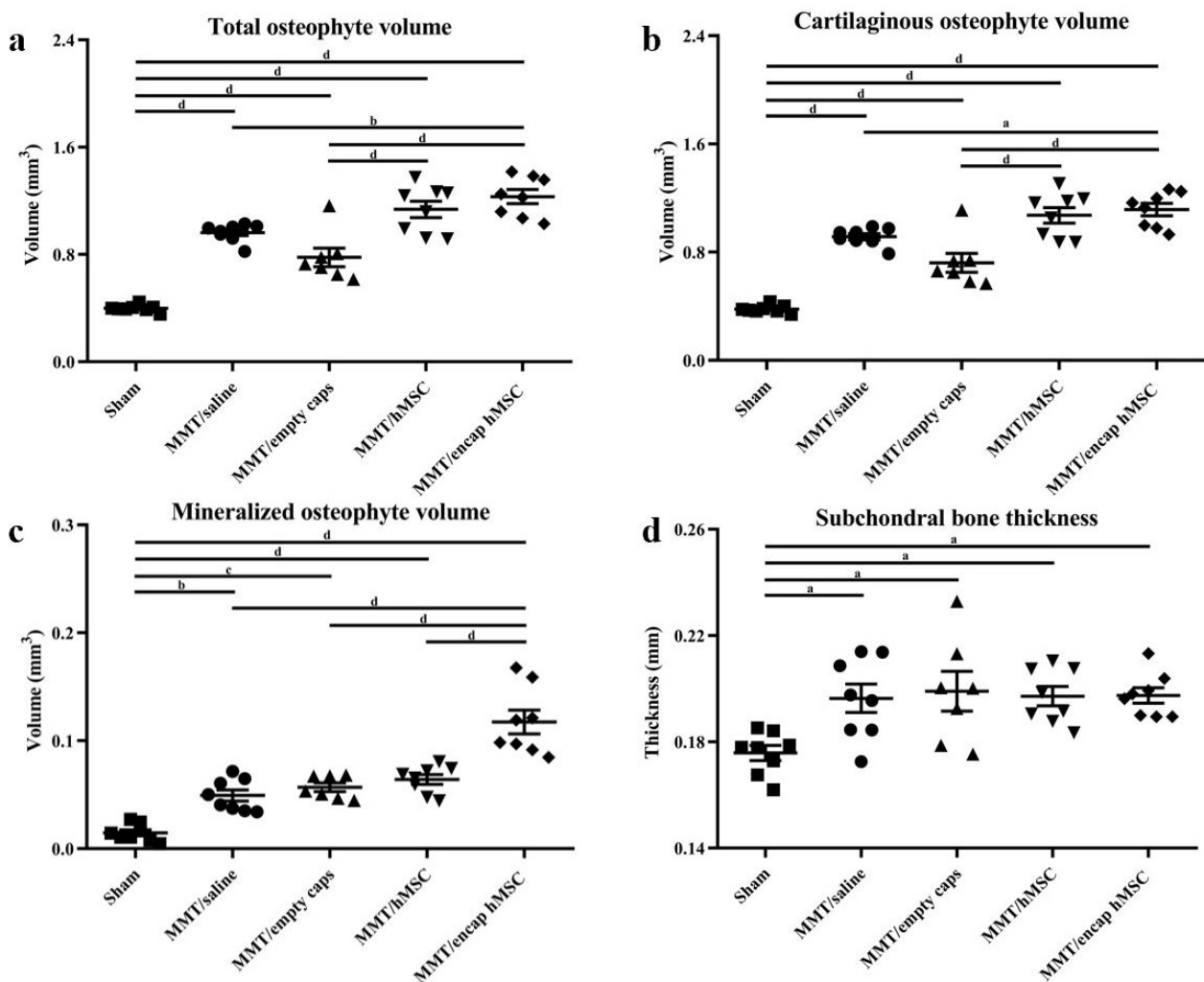


Fig. 7. EPIC- μ CT quantification of osteophyte formation and subchondral bone morphology of medial side of MMT joints treated with encapsulated hMSCs. (a) Total osteophyte volume was significantly increased in all MMT conditions as compared to sham control; encapsulated hMSCs augmented osteophyte volumes as compared to saline and empty capsule conditions. (b) Cartilaginous osteophyte volumes yielded the same respective differences among groups as the total osteophyte volume parameter. (c) Mineralized osteophyte volume was significantly increased in all MMT conditions as compared to sham control; encapsulated hMSCs augmented mineralized osteophyte volumes as compared to all other MMT conditions. (d) Subchondral bone thickness was significantly increased in all MMT conditions as compared to sham control. Data presented as mean \pm SD. $n = 7$ /group MMT/empty caps; $n = 8$ /group for all other conditions. ^a $p < 0.05$; ^b $p \leq 0.01$; ^c $p \leq 0.001$; ^d $p \leq 0.0001$.

the encapsulated hMSC group in comparison to all control groups. Additionally, cartilaginous osteophyte volumes were larger for encapsulated hMSCs in comparison to all groups, except the hMSC group. The effects that MSCs can have on osteophyte formation remains largely unknown. Osteophytes in general are understudied and their role and function remain poorly understood in OA. While the formation of osteophytes is hypothesized to be a compensatory mechanism in early OA, late stage osteophytes may be associated with further stages of disease progression and symptoms (Muraki *et al.*, 2011; Serban *et al.*, 2016; van der Berg, 1999). Even though studies as to the mechanical role of osteophytes in the knee are lacking, the function of osteophytes in the vertebral bodies of the human spines is reported (Al-Rawahi *et al.*, 2011). Vertebral body osteophytes increase motion segment resistance to both bending and compression forces, suggesting that osteophytes' formation reverses the mechanical stimuli that cause them to form, in a possible compensatory and protective role (Al-Rawahi *et al.*, 2011). Clinically, in late stage knee OA, osteophyte formation strongly correlates with pain level and patient quality of life (Muraki *et al.*, 2011; Serban *et al.*, 2016; van der Berg, 1999); however, cartilage damage (and not osteophytes) is the strongest predictor of pain in these same late stage OA patients (Serban *et al.*, 2016). Studies isolating the associated pain levels of these late stage pathologies, independent of one another, are limited (Serban *et al.*, 2016). In addition to these studies, Kirkley *et al.* (2008) demonstrate that arthroscopic removal of osteophytes brings no additional clinical benefits. The clinical implications of osteophytes are not well characterized in early OA, as osteophyte formation usually presents (or is at least identified and reported) in the latter stages of the disease, when these structures are augmented and more radiographically identifiable. While the present study did not analyze late stage OA, the results warrant further study.

Even though many questions remain as to the mechanism of osteophyte formation, MSCs are implicated as a major player in their development (van der Kraan and van der Berg, 2007). Osteophytes develop from the marginal tissue periosteum surrounding subchondral cortical bone, where endogenous MSCs are stimulated to proliferate by various mechanical and biochemical cues (van der Kraan and van der Berg, 2007). Then, cells within the developing osteophyte undergo chondrogenesis and differentiate into mature hypertrophic chondrocytes (van der Kraan and van der Berg, 2007). Following the development of this cartilaginous tissue, vascular invasion occurs and chondrocytes are replaced by osteoblasts to form bone and marrow cavities (van der Kraan and van der Berg, 2007). This developmental process is similar to the endochondral ossification in bone growth plates, however, the exact mechanism has yet to be elucidated. Fully developed osteophytes integrate with the subchondral bone and

retain an outer covering of cartilage, expanding the original cartilage surface of the joint (van der Kraan and van der Berg, 2007). The implication of MSCs as a major player in osteophyte development speaks to the potential role hMSC paracrine factors may have in augmenting osteophyte formation. Numerous paracrine factors that are implicated in osteophyte development are identified in the hMSC secretome, including fibroblast growth factor (FGF)-9, TGF- β , bone morphogenic protein (BMP)-2 and insulin-like growth factor (IGF)-1 (Davidson *et al.*, 2007; Okazaki *et al.*, 1999; van der Kraan and van der Berg, 2007; Zhou *et al.*, 2016). While many questions remain about the role of osteophytes, the results of the present study should warrant consideration and further investigation when using hMSCs in patients.

Quantitative EPIC- μ CT analysis of subchondral bone thickness showed an increase in subchondral bone thickness for all MMT conditions in comparison to the sham control. This increase in thickness was evidence of increased sclerosis (abnormal hardening), which is a hallmark of OA development (Radin *et al.*, 1972). However, no differences were detected between any of the MMT conditions, indicating a lack of enhancement or of a protective effect of subchondral bone sclerosis by encapsulated hMSCs. These results contrast previous studies reporting a protective effect of MSCs on subchondral bone in the form of decreased mineralization and subsequent reduction in sclerosis (thickening) (Kim *et al.*, 2014; Murphy *et al.*, 2003). Changes in the synovium were not assessed in the current study since significant differences in the synovium, between sham and MMT animals, do not present in this model until later time points (Kloefkorn *et al.*, 2017). Collectively, the results of the study showed that hMSC paracrine communication yielded a chondroprotective role on articular cartilage in early OA but also augmented osteophyte formations.

The hMSC group, in comparison to the encapsulated hMSC group, did not yield the same early chondroprotective effect and did not yield significantly larger mineralized osteophyte volumes than the other study groups, as measured by EPIC- μ CT analysis. The results of the luciferase-tracking study suggested that the increased hMSC bioluminescence played a minor role in the therapeutic efficacy of hMSCs, as encapsulation did not enhance bioluminescent activity as markedly as was initially hypothesized. It is possible that encapsulation may also affect the paracrine signaling properties of hMSCs and further contribute to the results yielded in the EPIC- μ CT analyses. However, a limitation of the study was the inability to delineate between the effects of hMSC bioluminescence (viability, retention, proliferation and metabolic state) and the paracrine signaling properties of these cells, as these could not be specifically isolated and studied independently of one another. A further limitation was the inability to successfully recover encapsulated hMSCs from the knee joint. For both the encapsulated and

non-encapsulated groups, the same batch of cells were used for intra-articular injections, with both containing the same initial secretome factors. *In vitro*, encapsulation affects the MSC secretome, with certain factors being differently affected in comparison to MSC monolayer cultures (Landázuri *et al.*, 2016; Stucky *et al.*, 2015). Encapsulation upregulates prostaglandin E₂ (PGE₂), which reduces the levels of the pro-inflammatory cytokine TNF α , implicated in the breakdown of cartilage in OA (Kunisch *et al.*, 2016; Stucky *et al.*, 2015). However, the study by Stucky *et al.* (2015) is unable to delineate between the individual effects of the alginate and the 3D culture environment within the micro-capsule and the role each of these had in the study results. Furthermore, encapsulation of hMSCs upregulates numerous factors, including bFGF, phosphatidylinositol-glycan biosynthesis class F protein (PIGF) and vascular endothelial growth factor (VEGF), and downregulates the hepatocyte growth factor (HGF), among others, in comparison to non-encapsulated cells (Landázuri *et al.*, 2012). This potential for alterations in paracrine secretory activity might also account for the differences noted in the present study. Additionally, while the intercellular signaling properties of extracellular vesicles are an important mediator in the therapeutic efficacy of MSCs in OA, these structures are unable to readily diffuse through the capsules employed in the present study (Cosenza *et al.*, 2017). The two main types of extracellular vesicles, exosomes and microvesicles, which maintain sizes of 50-150 nm and 50-500 nm, respectively, exceed the 40 nm pore size of the capsules previously established (molecular diameter IgG ~ 40 nm) (Landázuri *et al.*, 2012; van Niel *et al.*, 2018). The potential effects encapsulation has on enhanced bioluminescent activity and varied paracrine secretory activity are important observations. This motivates further study of the effects encapsulation has on the secretory profiles of hMSCs and hMSCs paracrine communication and of hMSCs and encapsulation therapeutic efficacy.

With the substantial and increasing burden of OA and limited treatment options outside of temporary symptomatic relief, there is a critical need for the development of disease-modifying therapeutics. MSCs show great promise but questions remain as it relates to their mechanism of action. The present study showed that hMSCs could exert a chondroprotective therapeutic effect through paracrine signaling, independent of direct engraftment, as encapsulated hMSCs yielded an early protective role on articular cartilage in OA. Furthermore, the study showed the effects hMSCs, through their paracrine signaling properties, could have on osteophyte formation, as encapsulated hMSCs increased osteophyte volumes. These augmented tissue volumes are especially relevant in clinical applications as many clinical trials are currently ongoing but the effects of osteophyte development have not been investigated so far. Further study of the efficacy of these encapsulated

hMSCs on OA progression after the disease has developed will have clinical relevance, as OA is not diagnosed clinically until patients present with augmented OA phenotypes in later stage OA.

Conclusions

Encapsulation of bone marrow hMSCs with sodium alginate allowed for the assessment of the paracrine signaling properties of these cells, by preventing their direct engraftment into the native tissue. The paracrine mechanisms of these hMSCs showed a chondroprotective role for articular cartilage in early stage post-traumatic OA, attenuating increases in articular cartilage swelling and surface roughness. However, in addition to these early protective effects, cartilaginous and mineralized osteophyte volumes were enhanced. This early cartilage protective effect was consistent with previous reports of MSC therapeutics for OA, suggesting that direct engraftment of MSCs might not be necessary for the therapeutic benefit of an MSC injection for OA. However, the effects MSCs could have on augmenting osteophyte formations was a new observation and warrants consideration and further investigation as MSC therapies are currently being used clinically. Overall, the study demonstrated that the paracrine signaling properties of hMSCs, alone, could exert a chondroprotective therapeutic effect in early stage OA.

Acknowledgements

This work was supported in part by VA (SPiRE) Grant I21RX002372-01A1 from the United States (U.S.) Department of Veterans Affairs Rehabilitation Research and Development Service. The research was also supported in part by the DOD PRMRP Grant PR171379 and PHS Grant UL1TR000454 from the Clinical and Translational Science Award Program, National Institutes of Health, National Center for Advancing Translational Sciences. The authors would like to thank Mila Friedman for the histological analyses and Colleen Oliver for her support in the animal study.

Disclaimer

The contents do not represent the views of the U.S. Department of Veterans Affairs or the United States Government.

References

Allen AB, Gazit Z, Su S, Stevens HY, Guldborg RE (2014) *In vivo* bioluminescent tracking of

mesenchymal stem cells within large hydrogel constructs. *Tissue Eng Part C Methods* **20**: 806-816.

Al-Rawahi M, Luo J, Pollintine P, Dolan P, Adams MA (2011) Mechanical function of vertebral body osteophytes, as revealed by experiments on cadaveric spines. *Spine* **36**: 770-777.

Bendele AM (2001) Animal models of osteoarthritis. *J Musculoskelet Neuronal Interact* **1**: 363-376.

Bertrand J, Cromme C, Umlauf D, Frank S, Pap T (2010) Molecular mechanisms of cartilage remodeling in osteoarthritis. *Int J Biochem Cell Biol* **42**: 1594-1601.

Campeau E, Ruhl VE, Rodier F, Smith CL, Rahmberg BL, Fuss JO, Campisi J, Yaswen P, Cooper PK, Kaufman PD (2009) A versatile viral system for expression and depletion of proteins in mammalian cells. *PLoS One* **4**: e6529.

Choi H, Lee RH, Bazhanov N, Oh JY, Prockop DJ (2011) Anti-inflammatory protein TSG-6 secreted by activated MSCs attenuates zymosan-induced mouse peritonitis by decreasing TLR2/NF- κ B signaling in resident macrophages. *Blood* **118**: 330-338.

Cisternas MG, Murphy L, Sacks JJ, Solomon DH, Pasta DJ, Helmick CG (2016) Alternative methods for defining osteoarthritis and the impact on estimating prevalence in a US population-based survey. *Arthritis Care Res* **68**: 574-80.

Cosenza S, Ruiz M, Toupet K, Jorgensen C, Noël D (2017) Mesenchymal stem cells derived exosomes and microparticles protect cartilage and bone from degradation in osteoarthritis. *Sci Rep* **7**: 16214. DOI: 10.1038/s41598-017-15376-8.

Davidson ENB, Vitters EL, van Beuningen HM, van de Loo FAJ, van den Berg WB, van der Kraan PM (2007) Resemblance of osteophytes in experimental osteoarthritis to transforming growth factor β -induced osteophytes: limited role of bone morphogenetic protein in early osteoarthritic osteophyte formation. *Arthritis Rheum* **56**: 4065-4073.

Diekman BO, Wu C-L, Louer CR, Furman BD, Huebner JL, Kraus VB, Olson SA, Guilak F (2013) Intra-articular delivery of purified mesenchymal stem cells from C57BL/6 or MRL/MpJ superhealer mice prevents posttraumatic arthritis. *Cell Transplant* **22**: 1395-1408.

Farrell E, Fahy N, Ryan AE, Flatharta CO, O'Flynn L, Ritter T, Murphy JM (2016) VIL-10-overexpressing human MSCs modulate naïve and activated T lymphocytes following induction of collagenase-induced osteoarthritis. *Stem Cell Res Ther* **7**: 74. DOI: 10.1186/s13287-016-0331-2.

Galleu A, Riffo-Vasquez Y, Trento C, Lomas C, Dolcetti L, Cheung TS, Von Bonin M, Barbieri L, Halai K, Ward S, Weng L, Chakraverty R, Lombardi G, Watt F, Orchard K, Marks D, Apperley J, Bornhauser M, Walczak H, Bennett C, Dazzi F (2017) Apoptosis in mesenchymal stromal cells induces *in vivo* recipient-mediated immunomodulation. *Sci Transl Med* **9**: 1-11.

Grigolo B, Lisignoli G, Desando G, Cavallo C, Marconi E, Tschon M, Giavaresi G, Fini M, Giardino R, Facchini A (2009) Osteoarthritis treated with mesenchymal stem cells on hyaluronan-based

scaffold in rabbit. *Tissue Eng Part C Methods* **15**: 647-658.

Hatsushika D, Muneta T, Horie M, Koga H, Tsuji K, Sekiya I (2013) Intraarticular injection of synovial stem cells promotes meniscal regeneration in a rabbit massive meniscal defect model. *J Orthop Res* **31**: 1354-1359.

Horie M, Choi H, Lee RH, Reger RL, Ylostalo J, Muneta T, Sekiya I, Prockop DJ (2012) Intra-articular injection of human mesenchymal stem cells (MSCs) promote rat meniscal regeneration by being activated to express Indian hedgehog that enhances expression of type II collagen. *Osteoarthr Cartil* **20**: 1197-1207.

Janusz MJ, Bendele AM, Brown KK, Taiwo YO, Hsieh L, Heitmeyer SA (2002) Induction of osteoarthritis in the rat by surgical tear of the meniscus: inhibition of joint damage by a matrix metalloproteinase inhibitor. *Osteoarthr Cartil* **10**: 785-791.

Kim JE, Lee SM, Kim SH, Tatman P, Gee AO, Kim D-H, Lee KE, Jung Y, Kim SJ (2014) Effect of self-assembled peptide-mesenchymal stem cell complex on the progression of osteoarthritis in a rat model. *Int J Nanomedicine* **9** **Suppl 1**: 141-157.

Kintscher U, Wakino S, Bruemmer D, Goetze S, Graf K, Hsueh WA, Law RE (2002) TGF-beta(1) induces peroxisome proliferator-activated receptor gamma1 and gamma2 expression in human THP-1 monocytes. *Biochem Biophys Res Commun* **297**: 794-799.

Kirkley A, Birmingham TB, Litchfield RB, Giffin JR, Willits KR, Wong CJ, Feagan BG, Donner A, Griffin SH, D'Ascanio LM, Pope JE, Fowler PJ (2008) A randomized trial of arthroscopic surgery for osteoarthritis of the knee. *N Engl J Med* **359**: 1097-1107.

Kloefkorn HE, Allen KD (2017) Quantitative histological grading methods to assess subchondral bone and synovium changes subsequent to medial meniscus transection in the rat. *Connect Tissue Res* **58**: 373-385.

Kunisch E, Kinne RW, Alsalameh RJ, Alsalameh S (2016) Pro-inflammatory IL-1beta and/or TNF-alpha up-regulate matrix metalloproteases-1 and -3 mRNA in chondrocyte subpopulations potentially pathogenic in osteoarthritis: *in situ* hybridization studies on a single cell level. *Int J Rheum Dis* **19**: 557-566.

Kunzmann S, Wright JR, Steinhilber W, Kramer BW, Blaser K, Speer CP, Schmidt-Weber C (2006) TGF-beta1 in SP-A preparations influence immune suppressive properties of SP-A on human CD4+ T lymphocytes. *Am J Physiol Lung Cell Mol Physiol* **291**: L747-756.

Landázuri N, Levit RD, Joseph G, Ortega-Legaspi JM, Flores CA, Weiss D, Sambanis A, Weber CJ, Safley SA, Taylor WR (2012) Alginate microencapsulation of human mesenchymal stem cells as a strategy to enhance paracrine-mediated vascular recovery after hindlimb ischaemia. *J Tissue Eng Regen Med* **10**: 222-232.

- Leijs M, Villafuertes E, Haeck J, Koevoet W, Fernandez-Gutierrez B, Hoogduijn M, Verhaar J, Bernsen M, van Buul G, van Osch G (2017) Encapsulation of allogeneic mesenchymal stem cells in alginate extends local presence and therapeutic function. *Eur Cell Mater* **33**: 43-58.
- Levit RD, Landázuri N, Phelps EA, Brown ME, Garcia AJ, Davis ME, Joseph G, Long R, Safley SA, Suever JD, Lyle AN, Weber CJ, Taylor WR (2013) Cellular encapsulation enhances cardiac repair. *J Am Heart Assoc* **2**: e000367. DOI: 10.1161/JAHA.113.000367.
- Lin CS, Lin G, Lue TF (2012) Allogeneic and xenogeneic transplantation of adipose-derived stem cells in immunocompetent recipients without immunosuppressants. *Stem Cells Dev* **21**: 2770-2778.
- Liu X, Duan B, Cheng Z, Jia X, Mao L, Fu H, Che Y, Ou L, Liu L, Kong D (2011) SDF-1/CXCR4 axis modulates bone marrow mesenchymal stem cell apoptosis, migration and cytokine secretion. *Protein Cell* **2**: 845-854.
- Loeser RF, Goldring SR, Scanzello CR, Goldring MB (2012) Osteoarthritis: a disease of the joint as an organ. *Arthritis Rheum* **64**: 1697-1707.
- Mamidi MK, Das AK, Zakaria Z, Bhonde R (2016) Mesenchymal stromal cells for cartilage repair in osteoarthritis. *Osteoarthr Cartil* **24**: 1307-1316.
- Martel-Pelletier J (2004) Pathophysiology of osteoarthritis. *Osteoarthr Cartil* **12 Suppl A**: S31-3.
- Maumus M, Manferdini C, Toupet K, Peyrafitte J-A, Ferreira R, Facchini A, Gabusi E, Bourin P, Jorgensen C, Lisignoli G, Noël D (2013) Adipose mesenchymal stem cells protect chondrocytes from degeneration associated with osteoarthritis. *Stem Cell Res* **11**: 834-844.
- Messier SP, Loeser RF, Miller GD, Morgan TM, Rejeski WJ, Sevick MA, Ettinger WH, Pahor M, Williamson JD (2004) Exercise and dietary weight loss in overweight and obese older adults with knee osteoarthritis: the arthritis, diet, and activity promotion trial. *Arthritis Rheum* **50**: 1501-1510.
- Muraki S, Oka H, Akune T, En-Yo Y, Yoshida M, Suzuki T, Yoshida H, Ishibashi H, Tokimura F, Yamamoto S, Nakamura K, Kawaguchi H, Yoshimura N (2011) Independent association of joint space narrowing and osteophyte formation at the knee with health-related quality of life in Japan: a cross-sectional study. *Arthritis Rheum* **63**: 3859-3864.
- Murphy JM, Fink DJ, Hunziker EB, Barry FP (2003) Stem cell therapy in a caprine model of osteoarthritis. *Arthritis Rheum* **48**: 3464-3474.
- Namba A, Aida Y, Suzuki N, Watanabe Y, Kawato T, Motohashi M, Maeno M, Matsumura H, Matsumoto M (2007) Effects of IL-6 and soluble IL-6 receptor on the expression of cartilage matrix proteins in human chondrocytes. *Connect Tissue Res* **48**: 263-270.
- Niemeyer P, Vohrer J, Schmal H, Kasten P, Fellenberg J, Suedkamp NP, Mehlhorn AT (2008) Survival of human mesenchymal stromal cells from bone marrow and adipose tissue after xenogenic transplantation in immunocompetent mice. *Cytotherapy* **10**: 784-795.
- Okazaki K, Jingushi S, Ikenoue T, Urabe K, Sakai H, Ohtsuru A, Akino K, Yamashita S, Nomura S, Iwamoto Y (1999) Expression of insulin-like growth factor I messenger ribonucleic acid in developing osteophytes in murine experimental osteoarthritis and in rats inoculated with growth hormone-secreting tumor. *Endocrinology* **140**: 4821-4830.
- Orive G, Hernández RM, Gascón AR, Calafiore R, Chang TMS, Vos P De, Hortelano G, Hunkeler D, Lacík I, Shapiro AMJ, Pedraz JL (2003) Cell encapsulation: promise and progress. *Nat Med* **9**: 104-107.
- Palmer AW, Guldberg RE, Levenston ME (2006) Analysis of cartilage matrix fixed charge density and three-dimensional morphology *via* contrast-enhanced microcomputed tomography. *Proc Natl Acad Sci* **103**: 19255-19260.
- Pers Y-M, Ruiz M, Noël D, Jorgensen C (2015) Mesenchymal stem cells for the management of inflammation in osteoarthritis: state of the art and perspectives. *Osteoarthr Cartil* **23**: 2027-2035.
- Pigott JH, Ishihara A, Wellman ML, Russell DS, Bertone AL (2013) Investigation of the immune response to autologous, allogeneic, and xenogeneic mesenchymal stem cells after intra-articular injection in horses. *Vet Immunol Immunopathol* **156**: 99-106.
- Radin EL, Paul IL, Rose RM (1972) Role of mechanical factors in pathogenesis of primary osteoarthritis. *Lancet* **299**: 519-522.
- Reece DS, Thote T, Lin ASP, Willett NJ Guldberg RE (2017) Contrast enhanced μ CT imaging of early articular changes in a pre-clinical model of osteoarthritis. *Osteoarthr Cartil* **26**: 118-127.
- Sato M, Uchida K, Nakajima H, Miyazaki T, Guerrero A, Watanabe S, Roberts S, Baba H (2012) Direct transplantation of mesenchymal stem cells into the knee joints of hartley strain guinea pigs with spontaneous osteoarthritis. *Arthritis Res Ther* **14**: R31. DOI: 10.1186/ar3735.
- Saulnier N, Viguier E, Perrier-Groult E, Chenu C, Pillet E, Roger T, Maddens S, Boulocher C (2015) Intra-articular administration of xenogeneic neonatal mesenchymal stromal cells early after meniscal injury down-regulates metalloproteinase gene expression in synovium and prevents cartilage degradation in a rabbit model of osteoarthritis. *Osteoarthr Cartil* **23**: 122-133.
- Schmitz N, Laverty S, Kraus VB, Aigner T (2010) Basic methods in histopathology of joint tissues. *Osteoarthr Cartil* **18**: S113-S116.
- Serban O, Porojan M, Deac M, Cozma F, Solomon C, Lenghel M, Micu M, Fodor D (2016) Pain in bilateral knee osteoarthritis - correlations between clinical examination, radiological, and ultrasonographical findings. *Med Ultrason* **18**: 318-325.
- Shin EY, Wang L, Zemskova M, Deppen J, Xu K, Strobel F, Garcia AJ, Tirouvanziam R, Levit RD (2018)

Adenosine production by biomaterial supported mesenchymal stromal cells reduces the innate inflammatory response in myocardial ischemia/reperfusion injury. *J Am Heart Assoc* 7: e006949. DOI: 10.1161/JAHA.117.006949.

Stucky EC, Schloss RS, Yarmush ML, Shreiber DI (2015) Alginate micro-encapsulation of mesenchymal stromal cells enhances modulation of the neuro-inflammatory response. *Cytotherapy* 17: 1353-1364.

ter Huurne M, Schelbergen R, Blattes R, Blom A, de Munter W, Grevers LC, Jeanson J, Noël D, Casteilla L, Jorgensen C, van den Berg W, van Lent PLEM (2012) Antiinflammatory and chondroprotective effects of intraarticular injection of adipose-derived stem cells in experimental osteoarthritis. *Arthritis Rheum* 64: 3604-3613.

Thote T, Lin ASP, Raji Y, Moran S, Stevens HY, Hart M, Kamath R V, Guldborg RE, Willett NJ, Coulter WH, Woodruff GW (2013) Localized 3D analysis of cartilage composition and morphology in small animal models of joint degeneration. *Osteoarthr Cartil* 21: 1132-1141.

Toghraie F, Razmkhah M, Gholipour MA, Faghih Z, Chenari N, Torabi Nezhad S, Nazhvani Dehghani S, Ghaderi A (2012) Scaffold-free adipose-derived stem cells (ASCs) improve experimentally induced osteoarthritis in rabbits. *Arch Iran Med* 15: 495-499.

Van Buul GM, Siebelt M, Leijts MJC, Bos PK, Waarsing JH, Kops N, Weinans H, Verhaar J, Bernsen M, Van Osch GJVM (2014) Mesenchymal stem cells reduce pain but not degenerative changes in a monoiodoacetate rat model of osteoarthritis. *J Orthop Res* 32: 1167-1174.

van der Berg WB (1999) Osteophyte formation in osteoarthritis. *Osteoarthr Cartil* 7: 333.

van der Kraan PM, van den Berg WB (2007) Osteophytes: relevance and biology. *Osteoarthr Cartil* 15: 237-244.

van Niel G, D'Angelo G, Raposo G (2018) Shedding light on the cell biology of extracellular vesicles. *Nat Rev Mol Cell Biol* 19: 213-228.

Vos T, Global Burden of Disease Study 2010 Collaborators (2012) Years lived with disability (YLDs) for 1160 sequelae of 289 diseases and injuries 1990-2010: a systematic analysis for the global burden of disease study 2010. *Lancet* 380: 2163-2196.

Willett NJ, Thote T, Hart M, Moran S, Guldborg RE, Kamath R V, Woodruff GW (2016) Quantitative pre-clinical screening of therapeutics for joint diseases using contrast enhanced micro-computed tomography. *Osteoarthr Cartil* 24: 1604-1612.

Willett NJ, Thote T, Lin AS, Moran S, Raji Y, Sridaran S, Stevens HY, Guldborg RE (2014) Intra-articular injection of micronized dehydrated human amnion/chorion membrane attenuates osteoarthritis development. *Arthritis Res Ther* 16: R47. DOI: 10.1186/ar4476.

Xie L, Lin ASP, Guldborg RE, Levenston ME (2010) Nondestructive assessment of sGAG content and distribution in normal and degraded rat articular

cartilage *via* EPIC-microCT. *Osteoarthritis Cartilage* 18: 65-72.

Yu SP, Hunter DJ (2016) Intra-articular therapies for osteoarthritis. *Expert Opin Pharmacother* 17: 2057-2071.

Zhou S, Wang Z, Tang J, Li W, Huang J, Xu W, Luo F, Xu M, Wang J, Wen X, Chen L, Chen H, Su N, Shen Y, Du X, Xie Y, Chen L (2016) Exogenous fibroblast growth factor 9 attenuates cartilage degradation and aggravates osteophyte formation in post-traumatic osteoarthritis. *Osteoarthritis Cartilage* 24: 2181-2192.

Web Reference

1. <https://clinicaltrials.gov/ct2/home> [11-10-2017].

Discussion with Reviewers

Gerben van Buul: What is the effect of alginate on inflammation?

Authors: The immunogenicity of alginate capsules is influenced by alginate composition, method of synthesis and, in some cases, animal species. UP-LVG, bound to barium and lacking an outer polycationic membrane, as was the case in the present study, has better biocompatibility *in vivo* (Figliuzzi *et al.*, 2006; Safley *et al.*, 2008, additional references). Furthermore, microcapsules are more biocompatible in rodents, when compared to other species (Vaithilingam *et al.*, 2011, additional reference). It is also important to note that the empty capsule group was used as a control for any potential effects of the alginate capsules.

Mary Murphy: The increases in osteophyte formation observed are somewhat troubling; do the authors have any opinion on whether this would be the same outcome obtained when using syngeneic or even allogeneic MSCs? Additionally, is EPIC- μ CT previously shown to be associated with increased sensitivity for detection of osteophytes?

Authors: Increases in osteophyte volumes with encapsulated hMSC treatment also came as a surprise as no previous study reports this finding. However, MSCs can secrete numerous growth factors associated with endochondral ossification (Li *et al.*, 2016, additional reference). No other sourced encapsulated MSCs (allogeneic or syngeneic) were used in the MMT model and due to the scarcity of previous literature reporting these findings it is not possible to speculate on how alternatively sourced MSCs may impact these findings. It will be critically important for future studies to investigate this exact question. Additionally, EPIC- μ CT demonstrates increased sensitivity in analyzing osteophyte parameters, relative to the gold standard in the musculoskeletal field, histopathology (Willett *et al.*, 2016).

Additional References

Figliuzzi M, Plati T, Cornolti R, Adobati F, Fagiani A, Rossi L, Remuzzi G, Remuzzi A (2006) Biocompatibility and function of microencapsulated pancreatic islets. *Acta Biomater* **2**: 221-227.

Li C, Li G, Liu M, Zhou T, Zhou H (2016) Paracrine effect of inflammatory cytokine-activated bone marrow mesenchymal stem cells and its role in osteoblast function. *J Biosci Bioeng* **121**: 213-219.

Safley SA, Cui H, Cauffiel S, Tucker-Burden C, Weber CJ (2008) Biocompatibility and immune acceptance of adult porcine islets transplanted

intraperitoneally in diabetic NOD mice in calcium alginate poly-L-lysine microcapsules *versus* barium alginate microcapsules without poly-L-lysine. *J Diabetes Sci Technol* **2**: 760-767.

Vaithilingam V, Kollarikova G, Qi M, Lacik I, Oberholzer J, Guillemin GJ, Tuch BE (2011) Effect of prolonged gelling time on the intrinsic properties of barium alginate microcapsules and its biocompatibility. *J Microencapsul* **28**: 499-507.

Editor's note: The Scientific Editor responsible for this paper was Mauro Alini.